THE UNIVERSITY OF CHICAGO

THE DISTRIBUTION OF HEAT-PRODUCING RADIOACTIVE ELEMENTS IN THE DEEP EARTH

A DISSERTATION SUBMITTED TO
THE FACULTY OF THE DIVISION OF THE PHYSICAL SCIENCES
IN CANDIDACY FOR THE DEGREE OF
DOCTOR OF PHILOSOPHY

DEPARTMENT OF THE GEOPHYSICAL SCIENCES

BY
BETHANY A. CHIDESTER

CHICAGO, ILLINOIS
AUGUST 2017

For Peyton and Mae and all the young people who come after. May you never doubt that you can do hard things.

TABLE OF CONTENTS

LIST OF FIGURES

LIST OF TABLES

ACKNOWLEDGMENTS

None of the work described here could have been accomplished without the patient guidance and support of my advisor, Dr. Andy Campbell. Andy's open door and willingness to talk through problems with his students was invaluable to me, particularly since my background is very different than my PhD project. My sincerest thanks to Andy, for everything. I would also like to thank my committee members, Dr. Dion Heinz, Dr. Nicolas Dauphas, Dr. Andy Davis, and Dr. Frank Richter, for always asking hard questions and making me think about the bigger picture. To the rest of the Laboratory for Mineral Physics, including Dr. Rebecca Fischer, Lily Thompson, Nigel Brauser, Claire Zirkowski, and Anne Davis: thank you for the friendship, the support, the laughs, and the subtle competition which kept me going through the last 5 years. To all of the undergraduates I have worked with over the years, thank you for letting me be your teacher for a short while. Finally, thank you to Wade, who never doubted me and was always there to provide dinner when I had to work late.

ABSTRACT

The Earth is a heat engine, where large differences in temperature between the interior and the surface drive large-scale movement that manifests as plate tectonics and the geomagnetic field that protects us from the Sun's harmful charged particles. Decay of the long-lived radioactive elements U, Th, and K is expected to contribute as much as 45% of the current heat production in the Earth, and that heat production was five times higher early in Earth's history. It is unclear how this heat source affects the thermal and dynamic evolution of the Earth's core and mantle and how that contribution has changed over geologic time. This dissertation addresses this problem in several different ways.

This work represents the first high-pressure, high-temperature metal–silicate partitioning experiments for U, Th, and K in the laser-heated diamond anvil cell at conditions relevant to core formation. A chemical model is developed using parameterization of these partitioning data to constrain the concentrations of each of these elements in the core. Using a numerical calculation, it is then determined how that radioactive heat would contribute to the core's energy and entropy budget through time. One finds that, despite its strong lithophile nature at the surface, U partitions significantly into the metallic phase at increasing temperatures. This may be due to a decrease in U valence from 4+ to 2+ in high-pressure silicate melts, which our data supports. However, K and Th do not exhibit a similar change in behavior at these conditions, and this may drive fractionation between U and Th in the deep mantle. At the most extreme conditions of core formation, enough U could exist in the core to produce up to 4.4 TW of heat 4.5 billion years ago. Potassium could produce much less heat than U early on (< 1 TW), and due to its short half-life, would have decayed away much faster. While this energy source is significantly greater than was previously thought to be possible, it is likely not enough to explain the presence of the geomagnetic field early in Earth's history.

I have also completed a synchrotron-based study to determine the phase behavior and equations of state of UO_2 and ThO_2. ThO_2 undergoes a phase transition from the fluorite-type structure (thorianite) that is stable at ambient conditions to the previously identified

cotunnite-type structure around 19 GPa and 1500 K. It remains in the cotunnite-type phase up to 60 GPa and 2500 K. UO_2 undergoes several solid phase transitions at high pressure. The fluorite-type (uraninite) to cotunnite-type transition occurs around 20 GPa above 1100 K. At around 35 GPa, a new phase emerges; this phase has been indexed to a tetragonal crystal structure. Finally, at 80 GPa and above, UO_2 undergoes another phase transition or dissociates into two separate oxides. This understanding of the phase behavior of the simplest actinide-bearing minerals provides insight into the mineralogical hosts for these radioactive elements, as well as other large cations, in the Earth's deep mantle.

CHAPTER 1

INTRODUCTION AND BACKGROUND

The composition of the Earth is one of the most enigmatic problems in planetary science. We certainly have a good starting point – most of the Solar System material ended up in the Sun. Ergo, the average Solar System material has the same composition as the sun. However, the solar system bodies, from terrestrial planets to gas and ice giants to asteroids and comets, have unique compositions and properties, so there was some chemical heterogeneity involved in the planetary formation process. From seismic and magnetic observations, we know that Earth has a metallic core overlain by a rocky mantle, all topped by a very thin layer of crust. From meteorites, we know the core is mainly composed of iron, while the mantle plus crust is described as "pyrolitic". This means that the relative mantle abundances of the most refractory (i.e. least volatile) lithophile (rock-loving, or unlikely to partition into the metallic core) elements, such as aluminum, calcium, and uranium, match the compositions of those in bulk carbonaceous chondrite meteorites, the most primitive solar system material. The abundances of the less refractory elements in the mantle are estimated using petrological observations relative to these refractory elements in primitive near-surface rock samples (e.g. Ringwood (1966); McDonough and Sun (1995)).

However, we know that there are inaccessible regions of our planet that cannot be described by meteorites or near-surface samples due to the complex chemistry that occurs at the extreme pressure and temperature conditions of the deep Earth. These regions hold the key to big picture questions, such as: what is the trace- and volatile-element composition of the Earth; when did the planet separate into a core, mantle and crust; and how did this differentiation occur such that life can be supported on the surface? The answers to these questions can be addressed in part using mineral physics, the study of materials at high pressures and temperatures, so that their physical and chemical properties can be compared with our seismological and geochemical observations of the Earth. In effect, mineral physics is an experimental and theoretical means by which we connect the world that we cannot see

to the world that we can.

The Earth is a heat engine, driven by secular cooling, radioactive decay, and the segregation and solidification of materials into distinct layers (Verhoogen, 1980). Under the chondritic Earth assumption, the decay of the long-lived radioactive isotopes ^{235,238}U, ^{232}Th, and ^{40}K account for up to half of the total heat flux measured at the surface of the planet (McDonough and Sun, 1995; Lay et al., 2008; Arevalo et al., 2009). However, the distribution of these elements in the deepest part of the Earth and the role they have played in core and mantle dynamics through geologic time is uncertain. Furthermore, these elements, as well as many other large cation lithophile elements, are trace elements, which means they are expected to passively take part in chemical and physical processes within the mantle. They are also nominally incompatible in mantle minerals; i.e. they tend to partition out of mantle rocks during partial melting. These properties make them excellent tracers of mantle heterogeneities and planetary differentiation processes. Finally, the actinide elements, including U and Th, are important sources of energy for our growing population. Understanding their behavior and accommodation within silicate materials under extreme conditions will naturally lead to improved solid-state containment mechanisms for nuclear waste. The purpose of this work was two-fold. First, I sought to experimentally determine how these radioactive elements behave during planetary differentiation to constrain the radiogenic element budget in Earth's core. These experiments were then used to inform one-dimensional energy and entropy budget models of the core through geologic time. Second, I performed the first reported simultaneous high-pressure, high-temperature *in situ* measurements of the phase behaviors and equations of state of the actinide oxides, UO_2 and ThO_2, to determine their stability as hosts of these elements in the deep mantle.

1.1 The core's energy and entropy budget

To understand the importance of the distribution of radiogenic elements within the deepest part of the planet, and particularly within the core, one must first understand the energy

budget of the core and how it fits into the global energy balance. Earth's core consists of an iron-nickel alloy, with some amount of lighter element (e.g. S, Si, C, O, H), as evidenced by its seismically measured density. For a discussion on the current understanding of the core's composition, see McDonough (2013) or Hirose et al. (2013). Presently, the core can be divided into a liquid outer core and a solid inner core, which is slowly growing and freezing from the liquid as the planet cools through time. This crystalization is demonstrated in Fig. 1.1. We make the assumption that the outer core is well-stirred, because: 1) the viscosity of molten iron at those temperatures is very low, and 2) the observed geomagnetic field can only exist if a conducting fluid is in relative motion. Thus, we treat the outer core as energetically adiabatic except in very thin strips at the inner-core and core-mantle boundaries. Taking the adiabatic and melting temperature profiles of core material as given by Nimmo (2015), we see that the radius of the inner core through time is defined by the crossover point of these two curves. The inner-core boundary (ICB) is where the actual temperature of the material on the adiabat meets the melting temperature of the material at that pressure, as in Fig. 1.1. Here, as in Nimmo (2015), the adiabatic temperature of core material is anchored to the melting temperature of Fe at the ICB (330 GPa). Using the *ab initio* calculations of Alfe et al. (2002); Alfè et al. (2002); Alfe et al. (2003), this value is 6350 ± 300 K, which was reduced to 6200 K after accounting for errors in the DFT calculations (Alfe et al., 2002). An 11% decrease is then applied to this temperature to account for the melting temperature depression due to alloying light elements, resulting in a T_{ICB} of 5508 K. Extrapolating this

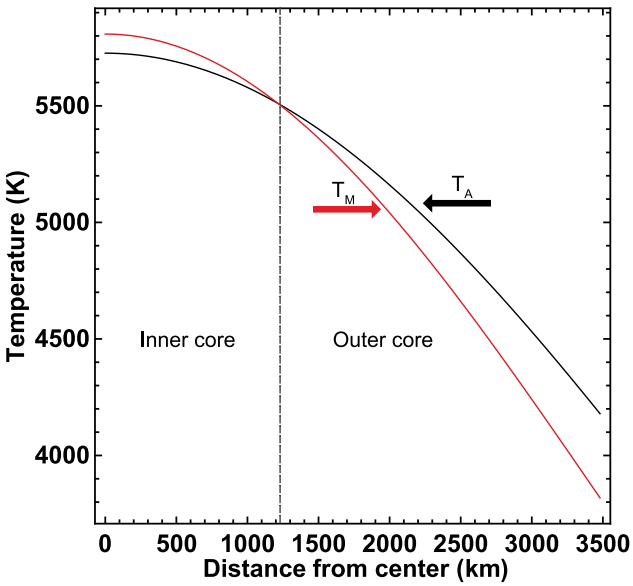

Figure 1.1: The melting temperature (T_M) and adiabatic temperature (T_A) as a function of depth within the core. The dashed line indicates the inner core-outer core boundary (ICB).

temperature along the adiabat, one finds T_{CMB} to be 4180 ± 400 K. Melting experiments on Ni to outer core conditions suggest that the presence of 5-10% Ni in the core will not significantly affect the melting temperature of core material at the ICB, so no adjustments to temperature were used to account for the presence of Ni (Lord et al., 2014).

Growth of the inner core assists in convection in the liquid outer core through several mechanisms, including latent heat release as the liquid–solid phase transition occurs and release of gravitational potential energy as light elements that are preferentially excluded from the solid inner core buoyantly rise. This convection largely drives the geodynamo and the geomagnetic field, which protects the Earth and its atmosphere from charged particles from the Sun. Understanding the intricacies of the forces driving the geodynamo, and particularly how they have changed through geologic time is important for several reasons. First, the geodynamo has been active for at least the last 3.45 billion years, and likely much longer (Biggin et al., 2011; Tarduno et al., 2010, 2015). This places strong constraints on the thermal evolution of the core through geologic time, and especially prior to the initiation of the inner core, which is estimated to be only ∼1 billion years old (Labrosse et al., 2001). Second, since the presence of the geodynamo intrinsically depends on the heat extracted from the core into the mantle, it is essential to understanding the thermal evolution of the mantle. Finally, by understanding the forces that are currently driving our magnetic field, we can better predict and model dynamo formation in other planets.

Recent calculations (de Koker et al., 2012; Pozzo et al., 2012, 2014) and experiments (Gomi et al., 2013; Gomi and Hirose, 2015; Gomi et al., 2016; Ohta et al., 2016; Seagle et al., 2013) have suggested that the thermal conductivity of core materials is much higher than previously thought. This means that prior to inner core solidification much of the energy is conducted out of the core along the adiabat so that the thermally driven geodynamo would not function unless temperatures were unreasonably high. However, energy budget calculations for the core have shown that by including a significant radiogenic heat source in the core, the calculated age of the inner core would be slightly older, but more importantly,

the inferred initial temperature of the core would be much lower (e.g. Nimmo (2015)). Thus, radioactive decay could explain the presence of the magnetic field early in Earth's history without unrealistically high CMB temperatures. A more detailed description of the core's energy budget and the effect of radioactive elements is provided in Chapter 4.

1.2 Metal–silicate partitioning of lithophile elements

The long-lived radioactive decay of the most abundant isotopes of U, Th, and K is likely an important source of energy driving the dynamics of the planet through geologic time. Assuming the Earth is pyrolitic, the decay of these elements account for 45% of the total heat flux measured at Earth's surface, and their heat production was 5 times higher when the planet formed (McDonough and Sun, 1995; Arevalo et al., 2009). Much of this heat production currently occurs in the crust (6-8 TW) and in the lower mantle (10-12 TW), with very little radioactive content in the depleted upper mantle ($\sim$2 TW) (Lay et al., 2008). The distribution of these elements in the deep Earth may have profound implications for the heat budget of the core, including the age of the inner core and the source of the geodynamo that has driven the Earth's magnetic field through geologic time, as well as the thermal evolution of the mantle (Labrosse et al., 2001). Whether these radioactive elements are an important heat source within the core itself has been uncertain. Based on the strongly lithophilic nature of these elements at ambient conditions, it has been considered unlikely that they would partition into the metallic phase as the core segregated (e.g. McDonough (2013)). However, it is difficult to reconcile the presence of a geomagnetic field prior to the initiation of the inner core without this heat source, because the temperatures required for a purely thermally driven dynamo early in Earth's history are unreasonably high such that there would be widespread lower mantle melting through much of Earth's history (Nimmo, 2015; Fiquet et al., 2010).

It has been suggested that the extremely high temperature conditions of core formation could cause even highly lithophile elements such as Mg to partition into the metallic core

(Badro et al., 2016; O'Rourke and Stevenson, 2016; O'Rourke et al., 2017). This leads one to reconsider whether other lithophile elements such as U, Th, K, and rare-earth elements (REE) might also partition into the core in significant amounts, and thus, explain isotopic deviations of REE in surface rocks with respect to the chondritic building blocks of the planet (Boyet and Carlson, 2005). The possibility of Mg in the core presents an additional energy source to consider. It has been suggested that if Mg were to significantly partition into the core and the solubility of Mg in liquid iron is strongly dependent upon temperature, then Mg-bearing silicates and oxides would precipitate out of the liquid metal as the core cools (O'Rourke and Stevenson, 2016; O'Rourke et al., 2017; Badro et al., 2016). This Mg-rich precipitate would be much more buoyant than the remaining liquid metal, which will sink through the core and drive convection. While this energy source was not taken into account in the energy budget calculations above, recent studies suggest this power source could be as much as an order of magnitude more efficient at driving the geomagnetic field than the growth of the inner core because the density difference between core material and magnesian minerals (a factor of $\sim$2) is much much greater than the density difference across the ICB ($\sim$ 3%) (O'Rourke and Stevenson, 2016). This behavior has also been suggested for Si-bearing oxides as well (Hirose et al., 2017), which could also be a major contributor to the core's energy budget if it participates in precipitation out of the metal phase as the planet cools. Chapter 3 below describes experiments undertaken to better understand the metal–silicate partitioning behavior of these lithophile elements (U, Th, K, and Mg) and to quantify their concentrations in the early core, while Chapter 4 includes these heat sources in a 1-dimensional core energy and entropy model to quantify their contribution to the geodynamo and the inferred initial temperature of the core.

1.3 Actinide mineralogy at extreme conditions

In addition to possibly being an important heat source in Earth's core, the long-lived radioactive elements may also be important in terms of the dynamics of the mantle, as well as

tracers for mantle geochemistry. The long-term goal is to have a planetary-scale knowledge of petrology and geochemsitry of these elements within the deep Earth to better understand the geochemical signals observed on the surface. However, petrology experiments at very extreme P-T conditions, such as the metal–silicate partitioning experiments described in Chapters 2 and 3 here, are challenging and it will take some time before we have a full picture of the petrology of the lowermost mantle. A good starting point for this goal is to experimentally determine the phase behavior and stability of mineral assemblages at pressures above 30 GPa and at geothermal temperatures.

Mineral–mineral and mineral–melt partitioning experiments in the large volume press show that up to ∼25 GPa, large, nominally incompatible elements, including the actinides (U and Th) and REEs, can be accommodated within the Ca site of Ca-Si-perovskite ($CaSiO_3$) (Corgne, 2002; Corgne et al., 2003, 2005; Greaux et al., 2009). This phase is expected to be the third most abundant phase in the lower mantle, after ferropericlase ((Mg,Fe)O) and bridgmanite ($(Mg,Fe)(Si,Al)O_3$). However, at the surface, these elements are more often found in accessory minerals such as zircon ($ZrSiO_4$) or oxides (uraninite, $(U,Th)O_2$) than major phases, so it follows that they could also be hosted to a great extent in high-pressure polymorphs of these accessory phases. Measurements of the high P-T phase behavior of zircon shows that this material decomposes into a high-pressure polymorph of ZrO_2 in the cotunnite-type structure and SiO_2-stishovite near 20 GPa at mantle temperatures (Tange and Takahashi, 2004). This suggests that below the transition zone the major host of actinide elements could also be oxides. For this reason, we investigated the phase behavior and stability of the actinide oxides, UO_2 and ThO_2, to ≥60 GPa and at high temperatures to better constrain the likely hosts of these elements in the lower mantle.

CHAPTER 2

EXPERIMENTAL METHODS

This chapter is based on methods reported in: Chidester, B.A., Rahman, Z., Righter, K., and Campbell, A.J. (2017) Metal–silicate partitioning of U: Implications for the heat budget of the core and evidence for reduced U in the mantle. *Geochimica et Cosmochimica Acta*, Chidester, B.A., Rahman, Z., Righter, K., and Campbell, A.J. (in prep) Metal–silicate partitioning behavior of lithophile elements at high pressures and temperatures, and Chidester, B.A., Pardo, O.S., Fischer, R.A., Thompson, E.C., Heinz, D.L., Prescher, C., Prakapenka, V.B., and Campbell, A.J. (in review) High-pressure phase behavior and equations of state of ThO_2 polymorphs. *American Mineralogist*

2.1 Metal–silicate partitioning experiments

2.1.1 Sample preparation and laser heating

Metal–silicate partitioning experiments were conducted at high pressures and high temperatures in the laser-heated diamond anvil cell (LH-DAC) in the Laboratory for Mineral Physics at the University of Chicago. The silicate used in most experiments was a mixed oxide powder having a major element composition of pyrolite (with or without Ca) (McDonough and Sun, 1995), but typically without any FeO to keep conditions as reducing as possible. When trace elements (i.e. U, Th, or K) were the focus of the study, they were introduced into the silicate material at elevated levels to facilitate analysis of the experimental run products. In two cases (B22 and B23) the silicate was composed of a mixture of UO_2, ThO_2 and SiO_2. MgO (99%), Al_2O_3 (99.99%), SiO_2 (99.9%), $CaSiO_3$ (meta, reagent grade), SiO_2:K_2O (2.5:1 by weight, 48 mesh), Fe (99.9+%, <10 μm), FeSi (99.9%) and FeS (99.9%) were all purchased from Alfa Aesar. To remove any contaminating OH from the oxide and silicate powders, they were fired in a furnace at 1000 °C for 12-20 hours prior to use. ThO_2 (99.99%) was purchased from Strem Chemical. Depleted UO_2 powder was purchased from SPI Chemical.

Table 2.1: Starting compositions for all metal–silicate partitioning experiments (weight %).

Sample	**Metal**	**Silicate**						
		MgO	Al_2O_3	CaO	SiO_2	UO_2	ThO_2	K_2O
B42	FeSi	36.56	8.40	0	43.44	11.60	0	0
B49	Fe–12S–22Si	35.35	8.13	3.31	42.00	11.22	0	0
B50	FeSi	35.35	8.13	3.31	42.00	11.22	0	0
B56	FeSi	35.35	8.13	3.31	42.00	11.22	0	0
B59	Fe–9Si	35.35	8.13	3.31	42.00	11.22	0	0
B66	Fe–4S–15Si	35.35	8.13	3.31	42.00	11.22	0	0
B72	Fe–4S–15Si	34.70	7.98	3.25	41.23	0	9.0	4.59
B77	Fe–4S–15Si	34.70	7.98	3.25	41.23	0	9.0	4.59
B83	Fe–4S–15Si	34.70	7.98	3.25	41.23	0	9.0	4.59
B85	Fe–9Si	34.70	7.98	3.25	41.23	0	9.0	4.59
B91	Fe–9Si	34.70	7.98	3.25	41.23	0	9.0	4.59
PC0.1	FeSi	39.77	9.14	3.72	47.26	0.1	0	0
PC0.4	FeSi	39.65	9.12	3.71	47.12	0.4	0	0
PC2	FeSi	39.02	8.97	3.65	46.36	2	0	0
PC12	FeSi	35.04	8.05	3.28	41.63	12	0	0

This material contained a small amount of polymer binder, so it was washed in ethanol and baked at 100 °C, though no higher to prevent oxidation of U, prior to sample preparation. The silicate and oxide materials were mixed together and ball-milled in a tungsten carbide (WC) capsule at 20 Hz for 1.5 hours to make a homogenous silicate material. The metal used in these experiments was either stoichiometric FeSi or a mixture of FeSi, FeS and Fe, to produce Fe alloys of targeted compositions during the experiment. The metals were also blended in a WC capsule using a ball mill at 20 Hz for 1.5 hours. Tungsten was not detected in any of the samples; however, it is possible that trace W was introduced during the ball milling processes and that it was not observed as a result of a strong peak overlap between W and Si using energy dispersive analytical techniques. The starting materials for each experiment are listed in Table 2.1

Oxygen fugacity is not controlled externally in LH-DAC experiments; this is precluded by the nature of the experiments ($\sim$10 μm x 30 μm diameter laser heated spot, confined between diamond anvils). Similarly, due to the very small scale of the samples, one cannot precisely control a priori the exact proportions of metal and silicate in each sample. Here, as

in previous metal–silicate partitioning experiments at very high P-T conditions, the oxygen fugacity of the system is self-buffered by exchange of Fe and Si between metal and silicate melts. We influenced this self-buffering toward reducing conditions by using starting materials with high Si contents in the metal, but as recognized previously (Siebert et al., 2012; Fischer et al., 2015), the Fe-Si exchange reaction at high P-T conditions drives the oxygen fugacity of the experimental products toward a relatively narrow range of ΔIW conditions. Importantly, we measure the composition of coexisting metal and silicate products to establish the fO_2 that was achieved in the experiments and find that the samples are consistent with core formation models (i.e. ΔIW=-3.3 to -1.5) (Rubie et al., 2015; Fischer et al., 2015).

Diamond anvil cell samples were loaded into stainless steel gaskets pre-indented to 18-23 GPa or rhenium gaskets pre-indented to 25-28 GPa. A hole, which serves as the sample chamber, was drilled in the center of this indentation by either milling with an electrical discharge machine (EDM) or laser ablation system. The diamond culets measured 300, 250, or 150 μm in diameter. The metallic sample material was pressed into a thin foil of 2-5 μm thick, and encapsulated within the sample chamber by flakes of silicate powder. Samples B22 and B23 were prepared as extreme end-members using a mixture of UO_2, ThO_2 and FeSi as the pressed flake and SiO_2 was used as the surrounding silicate. A small amount of Al_2O_3 was introduced in these two samples by processing in a corundum mortar and pestle. The samples were dried at 90 °C for 30-60 minutes after loading but prior to closing the cell, to remove any moisture from the sample. The pressure at the location to be heated was determined using the Raman shift of diamond (calibrated to ruby under quasi-hydrostatic conditions after Akahama and Kawamura (2007)) prior to heating. Several pressure measurements were made across each sample chamber, and they were found to be within 1-2 GPa on average, indicating reasonably constant stress state across the small sample chamber. Any non-hydrostatic strain is expected to be eliminated at the high temperatures of melting. Thermal pressure was estimated from two additional samples of the same geometry under the same pressure range that were laser heated with the benefit of *in situ* synchrotron X-ray

diffraction. The additional pressure due to heating above the sample liquidus was found to be ∼20% of the room temperature pressure (Fischer et al., 2015). The pressures reported here include the 20% thermal pressure for all samples in this study. The error on pressure was determined based on uncertainties in the thermal pressure and in the diamond Raman measurement.

The laser heating system used for these experiments is a double-sided version of that described by Campbell (2008). Samples were compressed to the target pressure, then laser-heated on both sides using a 1064 nm Yb-doped fiber laser. Temperature was gradually increased to above the sample liquidus over a period of 5 minutes. Samples were held at the maximum temperature for 15-30 seconds, then quenched to room temperature to conserve the high-temperature chemical distribution by turning off the laser. Average temperature in these experiments was measured spectro-radiometrically with 5-10 msec spectral exposures, while temperature gradients were simultaneously assessed using a four-color spectral imaging system with a 200-500 msec exposure time (Campbell, 2008). Temperatures were measured from both sides and the laser power was adjusted upstream and downstream to minimize temperature differences. For ease of programming, surface temperatures were initially calculated using Wien's approximation. It has been shown that this method underestimates temperature above 4000 K. Since many of the samples prepared here are at or above this temperature, a correction was made by fitting the misfit to the temperature vs. the known temperature and determining the temperature-dependent misfit, as shown in the following equation.

$$T_{real} = T_{meas} + (1.182(\frac{T_{meas}}{1000}) - 1.813)^{\frac{7}{2}} \tag{2.1}$$

The axial temperature gradient across the metal foil was also accounted for by corrected T_{real} by -3%, as demonstrated by Campbell et al. (2007).

2.1.2 Sample Recovery

The samples were decompressed over ∼30 minutes and then secured within the gasket to a 0.5" aluminum SEM pin stub. They were then coated with a thin (10 nm) layer of carbon to provide a conductive surface for imaging with an electron beam. The samples were sectioned along the axis of compression through the center of the laser-heated spot using a dual beam focused ion beam (FIB) at either Johnson Space Center (FEI Quanta 3D FEG) or the University of Chicago (Tescan Lyra3). The FIB sections of each sample were attached to a copper TEM grid with a platinum strip and thinned to $\leq$1 μm.

2.1.3 Chemical Analysis

Chemical analysis of the samples was done at the University of Chicago using energy dispersive X-ray spectroscopy (EDX) on either a JEOL 5800LV or Tescan Lyra3 scanning electron microscope (SEM) at 15 keV and ∼2 nA. Using the JEOL instrument, several profiles were taken across each sample with measurements every 0.25 μm and 2 minutes/step. Using the Tescan instrument, profiles were taken in 20 nm steps with a 10 ms dwell time per pixel and a total of 350 passes over the profile. Compositions were determined by averaging all of the point measurements from each respective phase. The measurements reported in this study are very precise due to a large number of measurements made in each phase. Based on measurements of analytical standards, the sample measurements are expected to be accurate to within 5% (relative). This calibration inaccuracy is expected to be similar for both the metal and the silicate melt because the measurements are made under identical conditions, so will cancel out in the partition coefficient calculations (see Eq. 3.2). Detection limits for Al, Ca, Mg, K, Th, and U in the metallic phase were determined as 3 times the standard error of the background in the metallic phase of sample B59, which contained all of these elements in concentrations too low to be detected by EDX. Similarly, the measurement of background for K and Th were made in sample B85. Detection limits are dependent on the number of measurements made in each phase because of counting statistics. For the metals

in the samples reported here (13-291 measurements) the range of detection limits is: 0.04-0.18 atom% Al, 0.01-0.15 atom% Ca, 0.06-0.28 atom% Mg, 0.02-0.09 atom% U, 0.013-0.021 atom% K, and 0.009-0.015 atom% Th. Detection limits were not an issue for any element in the silicate melt. X-ray maps of select elements were obtained for sample B42 using the JEOL 2500SE field emission scanning transmission electron microscope (STEM) at Johnson Space Center (Fig. 3.2).

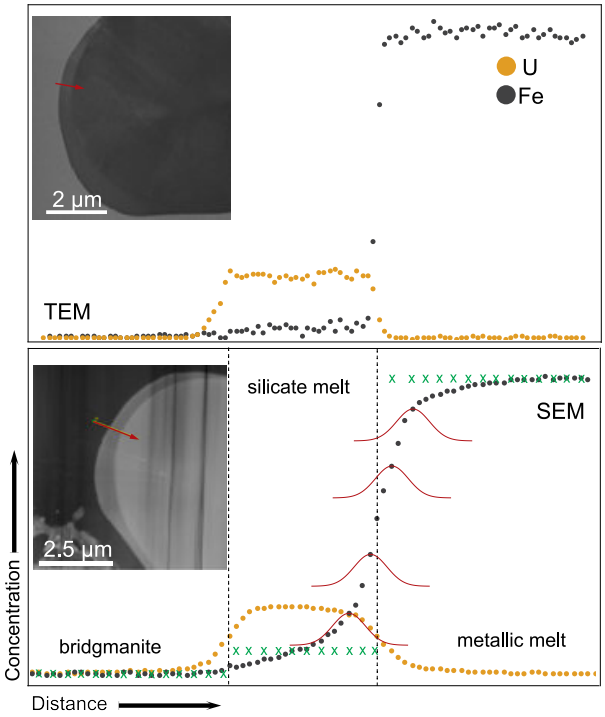

Figure 2.1: Illustration of signal deconvolution of the Fe signal in each phase using point-spread analysis. For comparison of spatial resolution, top panel was measured on the TEM at Johnson Space Center; bottom panel are measurements from the Tescan SEM at the University of Chicago. Filled circles are the measurements, green x's are the fitted compositions of Fe in each phase, dashed lines are the fitted boundaries between phases.

In several cases, the silicate melt region was small compared to the activation volume of the EDX measurements. In these cases, we were able to deconvolute the signals from each phase using a point-spread function. Each point measurement was treated as an integration over an area having a Gaussian-weighted signal, and the composition of the silicate melt was fitted to a line profile across each phase as shown in Figure 2.1. Other fitted parameters in this analysis included the location of the boundary between the silicate and metallic melt phases, the width of the Gaussian (σ), and if necessary, the composition of the silicate mineral in the outer region of the laser heated spot. For those samples whose compositions were fit in this way, the uncertainties provided are the standard errors to the fit.

Because the samples were thinner than the activation volume of the EDX measurement, the analyses were normalized to 100%. A previous metal–silicate study on tungsten has

shown that although samples of this type are thinner than the typical activation volume for EDX, there is little difference in the measured composition between using a the phi-rho-Z thin-film correction or the standard ZAF correction to the data (Shofner, 2011), so we chose to use the ZAF correction only. Oxide mole fractions in the silicate melt were calculated stoichiometrically using the following oxidation states: 6+ for S; 4+ for Si and Th; 3+ for Al; and 2+ for Fe, Mg, Ca, U (for a description, see Chapter 3), and 1+ for K. Oxygen measurements in Fe-rich alloys are often challenging using EDX because of a slight overlap in excitation energy between the O Kα line (0.525 keV) and the Fe Lα line (0.705 keV), but it is known that a significant amount of O will partition into Fe metals at high P-T conditions (Frost et al., 2010; Fischer et al., 2015), so it is necessary to obtain accurate O contents in the metals in these experiments. The Tescan system at the University of Chicago is equipped with a silicon-drift detector (Oxford Instruments X-MaxN) that has sufficient energy resolution to fully deconvolute these Fe and O peaks. Measurements on several Fe-bearing silicate and oxide standards on this instrument showed the O measurements to be accurate to within 5% (relative). Furthermore, there was no significant difference in the silicate melt compositions of our samples when they were calculated as stoichiometric oxides or when measuring O as a separate element. Finally, the oxygen content in the metal phase of each sample was compared to the expected O content from the published P-T dependence of O partitioning between peridotite and metal (Fischer et al., 2015), and most were found to be within 15% of those predicted values. Samples B42, B50 and B56 were not measured using the silicon-drift detector, so the reported metal compositions for these samples were obtained by measuring all elements except O in the EDX, and renormalizing with the O content predicted by the O partitioning parameters at the relevant P-T conditions (Fischer et al., 2015).

2.1.4 Piston-cylinder experiments and analysis

Four metal–silicate partitioning experiments with varying UO_2 contents were completed in the piston-cylinder (PC) apparatus to determine whether our higher *P-T* experiments can be considered within the Henry's Law regime of UO_2 concentrations. That is, we measured the partitioning as a function of UO_2 contents to determine whether the partitioning is directly dependent upon UO_2 concentrations or not. The large size of PC samples allows for very low concentration measurements to be made using laser ablation-inductively coupled plasma-mass spectrometry (LA-ICP-MS). Starting compositions are listed in Table 2.1, where metal and silicate phases were initially combined 50/50 by weight and homogenized in a WC capsule in the ball mill. Samples, contained in graphite capsules, were compressed to 1 GPa and heated at 2173 K in a non-end-loaded PC apparatus at NASA-Johnson Space Center. The runs were brought to temperature over 55 minutes, then allowed to equilibrate for 10 minutes. Temperatures were measured with a W5Re/W25Re thermocouple. Samples were quenched by cutting the power to the furnace. The rest of the experimental details have been documented by Righter et al. (2006) and Filiberto et al. (2008).

PC samples were chemically analyzed using EDX at the University of Chicago (described in Section 2.1.3) and with LA-ICP-MS under the supervision of Dr. Minako Righter at the University of Houston. LA-ICP-MS measurements were made using a Photon Machines Inc. Analyte.193 ArF laser ablation system coupled to a Varian 810-MS ICP-MS. The laser operated with a repetition rate of 4-10 Hz at 3 J/cm^2 and a helium flow rate of 0.5 L/minute. The spot sizes were 50 to 100 μm. Background measurements were made over 20 seconds, then ablation proceeded for 30 seconds, and the final washout occurred over 20 seconds, for a total of 70 seconds per measurement. The isotopes measured in both the silicate and metal melts in each sample were: ^{29}Si, ^{43}Ca, ^{49}Ti, ^{56}Fe, ^{61}Ni, ^{60}Ni, ^{232}Th, and ^{238}U. Three separate measurements were made in each phase and averaged to produce the final concentration. The measurements were calibrated using NIST 610 and NIST 612 glass standards (Pearce et al., 1997) and the data were reduced using the Glitter software (van

Achterbergh et al., 1999).

2.2 *In situ* X-ray diffraction

Four synchrotron powder X-ray diffraction (XRD) experiments on ThO_2 and 8 on UO_2 were conducted in the laser-heated diamond anvil cell (LH-DAC), with diamond culets of 300, 250, or 150 μm in diameter. The ThO_2 starting material was characterized by an ambient condition XRD measurement at the University of Chicago using incident radiation of λ=1.5418 Å(Cu K-α) and Si powder (NBS 640a) as an X-ray standard. Similarly, the UO_2 starting material was characterized a 1 bar, but no standard material was used. Amorphous Pt metal (Alfa Aesar, 0.2-1.6 μm, 99.9%) was mixed with the ThO_2 as an absorber for the laser heating experiments. The UO_2 or ThO_2/Pt mixture was loaded as a powder between flakes of KCl (reagent grade, Alfa Aesar) or KBr (spectroscopy grade, Alfa Aesar), which acted as the pressure medium, thermal insulator and pressure standard in the high-temperature experiments (Dewaele et al., 2012). Samples B11 and B12 were measured at room temperature using Ar as the pressure medium and pressure standard (Ross et al., 1986). A 3% uncertainty was assigned to the accuracy of the Ar pressure standard. The Ar was loaded cryogenically in the Laboratory for Mineral Physics at the University of Chicago.

Following safety regulations for radiogenic samples at the Department of Energy facilities where these measurements were made, the samples had "double containment" to prevent accidental environmental contamination or dispersal. The gasket and diamonds of the diamond anvil cell provided the first layer of containment. For the second layer of containment, the DACs were securely wrapped in Kapton® tape. In the laser-heating path, thin (0.5 mm) sapphire windows (6.35 mm diameter, Edmund Optics #45-467) were adhered to the outside of the diamond seat by epoxy. The sapphire windows typically resulted in several large and distinctive X-ray diffraction spots on the detector, which were masked out during data analysis.

Room temperature angle-dispersive powder XRD experiments were conducted at sector

12.2.2 at the Advanced Light Source (ALS), Lawrence Berkeley National Laboratory. These measurements were made on increasing pressure with a monochromatic incident X-ray beam ($\lambda = 0.4959$ Å) of ~10 μm in diameter. High-temperature XRD experiments were conducted at sector 13-ID-D (GSE-CARS) of the Advanced Photon Source (APS), Argonne National Laboratory. These XRD measurements were made using a monochromatic incident X-ray ($\lambda = 0.3344$ Å) typically measuring ~3 x 4 μm. At both facilities, sample to detector distance and tilt were calibrated using LaB_6. High-temperature samples were compressed to a target pressure, then laser heated while XRD measurements were simultaneously collected. The heating laser was co-aligned with the X-ray beam using the X-ray induced fluorescence of the KCl or KBr insulator. Laser-heating was done from both sides of the sample, adjusting upstream and downstream laser power to balance the temperature. Surface temperatures were measured spectro-radiometrically using the Plank radiation function (Prakapenka et al., 2008), and corrected by -3% to account for the axial temperature gradient across the sample (Campbell et al., 2007). The temperature of the alkali halide thermal insulator was estimated as the midpoint between the surface of the sample and the surface of the diamond anvil as described by Campbell et al. (2009).

Powder XRD patterns were collected on a CCD image plate and azimuthally integrated to 2θ (degrees) vs. intensity plots using DIOPTAS (Prescher and Prakapenka, 2015). To determine lattice parameters as a function of pressure and temperature, reflection positions were fit using PeakFit (Systat Software). At least one XRD pattern per heating cycle was fully indexed to confirm the space group and lattice parameters at each pressure step using GSAS-II (Toby and Von Dreele, 2013) or DICVOL04 (Boultif and Louër, 2004), which is part of the FULLProf Suite (Rodriguez-Carvajal, 1993).

2.3 Raman spectroscopy

In addition to XRD measurements, the room-temperature phase behavior of ThO_2 was investigated using Raman spectroscopy in the Laboratory for Mineral Physics at the University

of Chicago. Samples were prepared either as ThO_2 powder pressed between two MgO flakes, which acted as a Raman-inactive pressure-transmitting medium, or with no pressure medium. All samples were prepared in a steel gasket with an 80 μm sample chamber and 300 μm culet DAC. Measurements were taken using a 0.75-meter Acton SpectraPro monochromator with a 473 nm 150 mW blue laser for excitation. Pressure was determined using the Raman shift of the diamond, which was calibrated to ruby under quasi-hydrostatic conditions after (Akahama and Kawamura, 2007). Raman acquisitions of the sample were centered at 712 cm^{-1} in order to minimize nearby diamond Raman interference and were the average of 600 one-second exposures at full laser power. Compression measurements began at 3-5 GPa and samples were incrementally brought to $\sim$60 GPa before beginning decompression to ambient pressure. Raman mode frequencies were determined by peak fitting using PeakFit (Systat Software). To account for errors in background subtraction, etc., the reported frequencies are an average of three individual fitting routines and the error is its corresponding standard deviation.

CHAPTER 3

METAL–SILICATE PARTITIONING OF LITHOPHILE ELEMENTS

This chapter is based on Chidester, B.A., Rahman, Z., Righter, K., and Campbell, A.J. (2017) Metal–silicate partitioning of U: Implications for the heat budget of the core and evidence for reduced U in the mantle. *Geochimica et Cosmochimica Acta* and Chidester, B.A., Rahman, Z., Righter, K., and Campbell, A.J. (in prep) Metal–silicate partitioning behavior of lithophile elements at high pressures and temperatures.

3.1 Introduction

Previous high-pressure, high-temperature metal–silicate partitioning experiments have shown that U will partition into the metallic phase at very low oxygen fugacity (fO_2) and high S content, but that under the P-T-fO_2 conditions of Earth's upper mantle, the partitioning is too low for U to be an important heat source in the core (Malavergne et al., 2007; Bouhifd et al., 2013). While no studies of this type have been reported for Th, metal–silicate partitioning experiments of K show similar results to U, although there is much less consensus amongst these studies (Bouhifd et al., 2007; Corgne et al., 2007; Gessmann and Wood, 2002; Hirao et al., 2006; Murthy et al., 2003; Watanabe et al., 2014). However, most of these experiments were done at relatively low pressures and temperatures (i.e. $P \leq 20$ GPa and $T \leq 2700$ K), or suffered from various experimental biases (i.e. experiments were not above silicate liquidus, they used sulfides rather than metals, silicates were not of representative mafic compositions, etc). To match the mantle abundances of the siderophile elements such as Ni and Co, equilibration of the metal in a magma ocean would have had to take place at much deeper conditions on average (i.e. P between 30 and 60 GPa, with T up to 4200 K) (Li and Agee, 2001; Bouhifd and Jephcoat, 2011; Siebert et al., 2012; Fischer et al., 2015; Righter et al., 2016). Experiments at these more extreme conditions have shown that some

highly lithophile elements, such as Mg, could become significantly more siderophile, to the point where they could contribute to the light element budget of the core early in Earth's history (Badro et al., 2016). Additionally, it has been shown that the *s*-valence electron of K undergoes a transition to a *d*-orbital at high pressures, such that K mimics a transition metal (Bukowinski, 1976; Lee and Jeanloz, 2003; Lee et al., 2004). So, the metal–silicate partitioning behavior of the other lithophile elements, including U, Th, and K, could also be enhanced at extreme conditions.

Wohlers and Wood (2015) recently suggested that a significant amount of U (and other nominally lithophile elements) could have partitioned into sulfides at very reducing conditions in the solar nebula, and that by incorporating those sulfides into the growing core early in planetary accretion, those elements would have been trapped in the core even as the whole planet was continuously becoming more oxidized and S-depleted. That model relies on a very specific scenario for planetary growth, and it is necessary to consider more broadly the conditions under which heat-producing elements could have entered the core as the planet was growing. Thus, it is important to investigate the partitioning of U, Th, K, and other nominally lithophile elements at higher pressures and temperatures such that their partitioning behavior can be investigated within the P-T space of a deep magma ocean. Here, we demonstrate that under magma ocean conditions, U, K, and Mg become less lithophile, while Th remains strongly lithophile at all conditions. Depending on the parameters within a growing planet, U could have entered the core to significantly alter the energy budget of the core.

3.2 Results

3.2.1 Sample texture and equilibration

Six metal–silicate partitioning experiments were successfully completed for U and an additional four were conducted to explore the behavior of K and Th. Each of these experi-

ments were set up and conducted in the manner described in Section 2.1. Recovered samples were sectioned to ∼1 μm thick for observation in the SEM. Figures 3.1, 3.2, and 3.3 show representative samples after sectioning. The samples always consisted of a quenched rounded metal melt ball surrounded by a quenched silicate melt. There was a region of silicate material, often of bridgmanite composition, outside the silicate melt that texturally appeared to have been recrystallized during heating. Experiments containing Th and K often had a Th-rich mineral assemblage outside of the melt region as well (Fig. 3.1). The laser-heated spots were on the order of 20 μm in diameter. There was no evidence of immiscible metallic phases, in contrast to the miscibility gaps observed in the Fe-S-Si system below 15 GPa, Fe-FeO system above 16 GPa, and the Fe-O-S system around 3 GPa (Sanloup and Fei, 2004; Ringwood and Hibberson, 1990; Tsuno et al., 2007). The metal phase often exhibited a uniform quench texture, where Si and O that were soluble in the metal at high temperature exsolved upon rapid cooling. Due to the rapid quench rates in the diamond anvil cell, no strong crystalline quench texture was observed in the silicate melt, although occasionally metal blobs would exsolve out of the silicate melt upon quench (Fig. 3.1). That the boundaries between each phase (metallic melt, silicate melt and silicate mineral) were always smooth and continuous is evidence that the system within the laser-heated spot had a minimal free energy, i.e. was locally equilibrated under the high P-T experimental conditions.

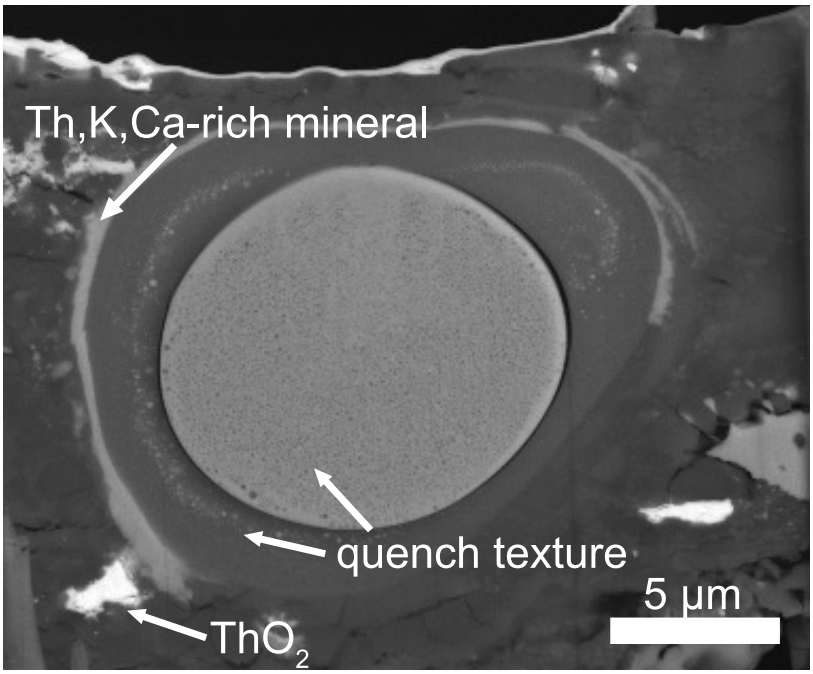

Figure 3.1: An example of several different quench textures in sample B85, recovered from 38 GPa and 3400 K.

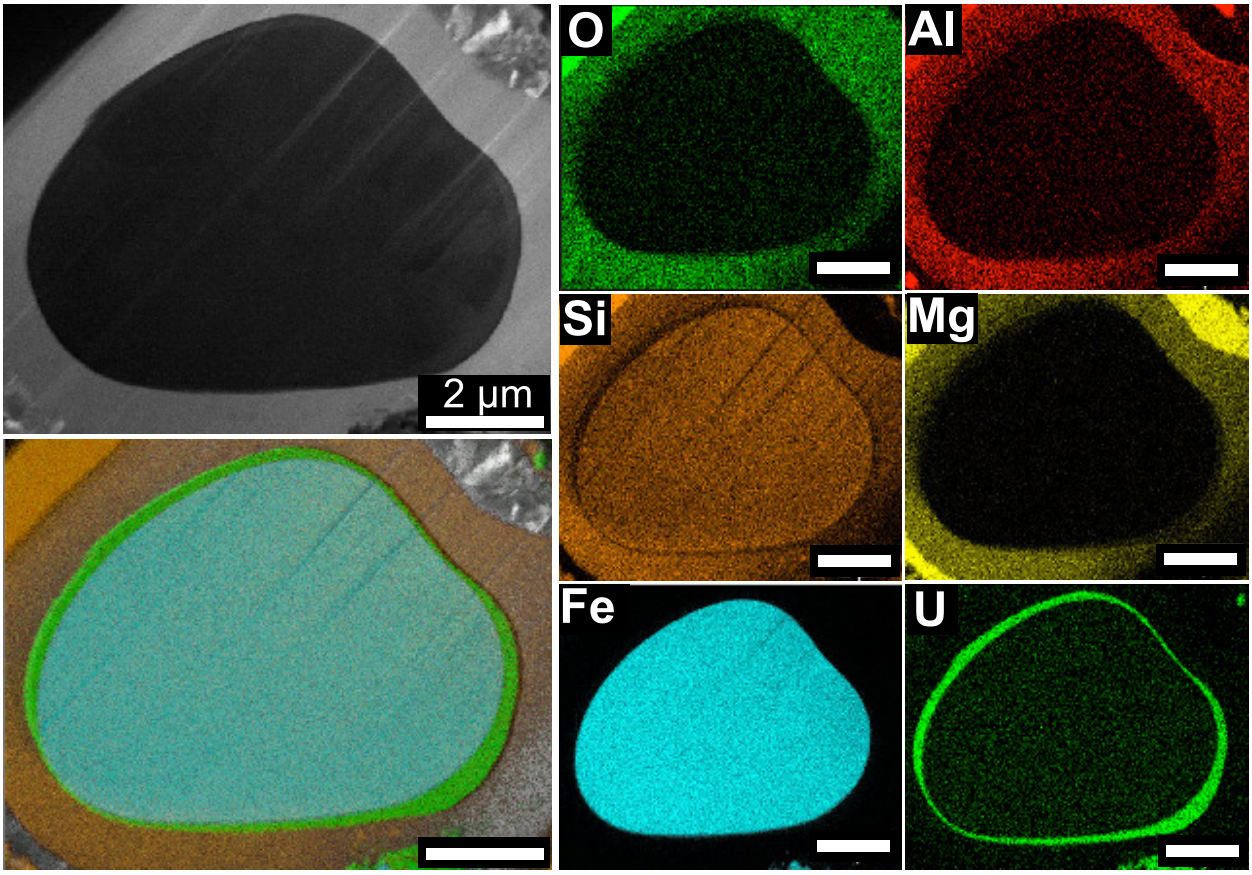

Figure 3.2: **(Top left)** Transmission electron image of sample B42, recovered from 57 GPa and 3800 K. The dark region contains metallic and silicate melts; the bright region is amorphous $MgSiO_3$ that was bridgmanite under high P conditions. **(Bottom left)** Composite X-ray map of Fe, U and Si. **(Right)** X-ray maps for individual elements.

Further demonstration of local equilibrium was that the composition of the silicate was uniform over sample regions of different scales, indicating that kinetic processes like thermal diffusion were not in evidence.

3.2.2 Chemical composition and oxygen fugacity

The pressure, temperature, and relative fO_2 conditions of each sample from this study are listed in Table 3.1. The compositions of each phase of each sample in this study and their errors are reported in Tables 3.2 (metal phase) and 3.3 (silicate phase). Here, fO_2 was calculated in reference to the iron-wüstite buffer assuming ideality (i.e. that the activities of Fe in the metal and FeO in the silicate were equal to their mole fractions in their respective

phases), such as:

$$\Delta IW = 2Log_{10}(\frac{X_{FeO,Silicate}}{X_{Fe,metal}}) \tag{3.1}$$

To evaluate the effect of the high concentrations of Si, O, and occasionally S in the metal phases of our samples, we also calculated this parameter using the activity of Fe (a_{Fe}) from the online metal activity calculator (`http://www.earth.ox.ac.uk/~expet/metalact/`; based on Wade and Wood (2005)) in place of $X_{\mathrm{Fe,metal}}$. This calculator failed to compute a result for several of our samples at very high temperatures. However, thermodynamic results using the model activities that were possible to compute were virtually unchanged using this model, except that the residuals to the fit appeared to trend slightly with temperature. We conclude that this type of model is not yet calibrated to sufficiently high temperatures for this study, and for now unnecessary given other uncertainties in our experiments. For consistency, the literature values for fO_2, as well as partition and exchange coefficients, were recalculated using mole fractions of elements and oxides converted from the weight percents reported.

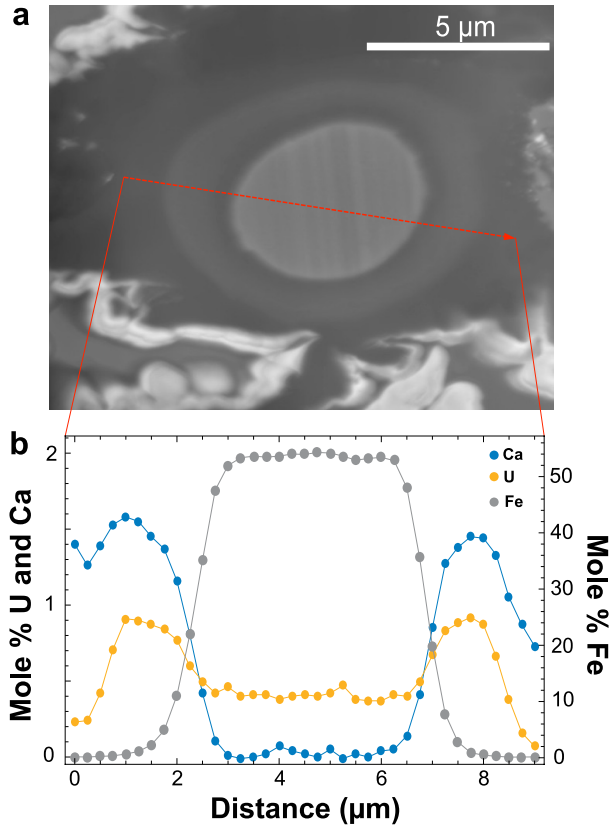

Figure 3.3: **a)** Back-scattered electron image of sample B50, recovered from 56 GPa and 4700 K. Red arrow indicates location of EDX profile. **b)** EDX profiles of U, Ca and Fe across sample B50. Measurements were made in 0.25 μm steps.

As mentioned previously, compositions of each phase were obtained from point measurements in profile across the laser-heated spot. An example of this type of measurement is given in Figure 3.3. In all relevant cases, U was measurable in the silicate melt and often within the metallic region, but was usually not measurable in the crystalline bridgmanite

Table 3.1: Experimental conditions for the DAC samples.

Sample	***P* (GPa)**	**+/-**	***T* (K)**	**+/-**	**fO_2 (ΔIW)**	**+/-**
B22	67	6	4700	400	-2.10	0.1/-0.1
B23	61	6	5000	300	-2.62	0.03/-0.04
B42	57	6	3800	200	-2.15	0.05/-0.05
B49	55	5	5400	300	-1.53	0.03/-0.03
B50	57	6	4800	300	-3.3	0.2/-0.2
B56	41	5	4000	200	-3.19	0.02/-0.02
B59	18	3	3200	200	-1.65	0.05/-0.05
B66	54	5	4400	300	-2.12	0.06/-0.07
B72	47	4	4200	200	-2.5	0.09/-0.1
B77	54	5	4800	200	-2.3	0.1/-0.2
B83	88	7	4500	500	-1.6	0.09/-0.1
B85	38	3	3400	300	-2.01	0.05/-0.05
B91	62	5	4700	200	-1.48	0.02/-0.02

Oxygen fugacity (fO_2) was calculated using the mole fractions of Fe and FeO and assuming ideality.

outside of the melt region. This demonstrates very low compatibility of U in crystalline bridgmanite (Corgne et al., 2005), as well as the significant partitioning of U into Fe metal at these high pressures and temperatures. In contrast, metal–silicate partitioning of Th and K was typically quite low. In fact, as mentioned above, the mineral–melt partitioning of these elements was surprisingly high, where they both concentrated in a Ca- and Th-rich mineral outside of the melt region. This indicates a dichotomy between the chemical behaviors of U with Th and K, which are quite similar at near-surface conditions.

It can be seen in Fig. 3.3 that in sample B50, recovered from 56 GPa and 4700 K, both U and Ca concentrate in the silicate melt, and that U partitions into the metal but Ca does not. A concern raised for measurement of metal–silicate partitioning samples from the laser-heated diamond anvil cell is that the spatial scale is too small, and the measurement is contaminated with fluorescence from a higher abundance region (Wade and Wood, 2012). In this regard, comparison of U chemical profiles with those of Ca is particularly important. Ca and U have similar absorption energies in EDX (3.164 and 3.690 kV for the U Mα line and the Ca Kα line, respectively); thus, if the measurements in the metal were artificially high due to fluorescence from the silicate, we would expect to see it with both elements, but this is not observed. Indeed, the apparent abundance of U in the silicate mineral directly

Table 3.2

Sample	Fe	Si	O	S	Al	Mg	U	Th	K	Ca	n
B22 mol%	57.27(5)	33.04(4)	8.34(5)	0	0	0	1.36(1)	≤0.034	0	0	261
wt%	69.78(6)	20.25(2)	2.91(3)	0	0	0	7.06(5)	nd	0	0	
B23 mol%	47.16(5)	42.51(4)	8.65(5)	0	0.1(1)	0	1.54(1)	≤0.026	0	0	91
wt%	60.75(6)	27.54(3)	3.19(3)	0	0.06(6)	0	8.45(5)	nd	0	0	
B42 mol%	48.7(1)	44.6(1)	5.26∗	0	0.23(2)	0.76(7)	0.45(1)	0	0	0	13
wt%	64.9(1)	29.91(7)	2.01∗	0	0.15(1)	0.44(4)	2.56(6)	0	0	0	
B49 mol%	33.40(4)	18.31(2)	21.28(6)	19.84(3)	0.950(8)	2.92(1)	3.299(8)	0	0	nd	126
wt%	44.01(5)	12.14(1)	8.03(4)	15.01(2)	0.605(5)	1.67(1)	18.53(4)	0	0	nd	
B50 mol%	57.7(1)	37.29(8)	2.54∗	0	0.75(2)	1.24(8)	0.439(5)	0	0	nd	29
wt%	72.2(1)	23.46(5)	0.91∗	0	0.45(1)	0.68(4)	2.34(3)	0	0	nd	
B56 mol%	50.40(6)	47.22(6)	1.93∗	0	0.2(1)	0.1(1)	0.122(5)	0	0	nd	151
wt%	66.88(8)	31.51(4)	0.73∗	0	0.13(6)	0.6(6)	0.69(3)	0	0	nd	
B59 mol%	63.6(1)	27.92(5)	8.3(1)	0	nd	0.19(3)	nd	0	0	nd	149
wt%	79.4(2)	17.53(3)	2.96(9)	0	nd	0.10(2)	nd	0	0	nd	
B66 mol%	66.36(8)	8.30(2)	19.51(7)	3.89(2)	0.30(1)	1.06(3)	0.580(8)	0	0	nd	40
wt%	81.5(1)	5.13(1)	6.86(4)	2.74(1)	0.178(6)	0.57(2)	3.04(4)	0	0	nd	
B72 mol%	55.55(6)	15.05(1)	18.17(5)	9.70(1)	0.433(4)	0.953(6)	0	0.036(2)	0.075(3)	0.032(3)	291
wt%	74.32(7)	10.13(1)	6.96(3)	7.448(8)	0.280(3)	0.555(4)	0	0.20(1)	0.70(3)	0.031(3)	
B77 mol%	73.2(4)	6.3(1)	11.5(2)	6.67(3)	0.42(1)	1.80(6)	0	0.049(4)	0.148(7)	0.064(6)	156
wt%	86.3(5)	3.71(7)	2.9(1)	4.52(2)	0.241(8)	0.92(3)	0	0.24(2)	0.122(6)	0.054(5)	
B83 mol%	52.0(2)	14.18(9)	22.1(2)	8.17(4)	0.64(1)	2.59(5)	0	0.125(4)	0.205(6)	nd	103
wt%	71.9(3)	9.88(7)	8.8(1)	6.50(3)	0.426(7)	1.56(3)	0	0.72(2)	0.199(6)	nd	
B85 mol%	78.6(1)	12.84(3)	8.22(7)	0	0.17(1)	0.18(2)	0	≤0.014	≤0.019	nd	127
wt%	89.7(1)	7.38(2)	2.69(4)	0	0.095(6)	0.09(1)	0	nd	nd	nd	
B91 mol%	59.27(8)	19.41(2)	19.41(6)	0	0.73(1)	1.01(3)	0	0.048(4)	0.063(6)	0.053(6)	233
wt%	78.3(1)	12.90(1)	7.35(4)	0	0.466(8)	0.58(2)	0	0.26(2)	0.058(5)	0.050(5)	

Metal phase compositions in both mole percent and weight percent for the samples in this study. Standard errors are given on the least significant digit. "n" is the number of measurements. Asterisks indicate oxygen contents that were calculated rather than measured - see text. If an element was below the detection limit, it is denoted as "nd". Elements with 0 percent were not present in the sample material.

Table 3.3

Sample	MgO	Al_2O_3	SO_3	SiO_2	CaO	FeO	ThO_2	UO	K_2O	Fit (Y/N)[†]
B22 mol%	0	8.89(6)	0	39.46(9)	0	5.13(8)	5.16(3)	41.37(7)	0	N, 251
wt%	0	5.84(4)	0	0	15.28(3)	0	2.38(4)	8.78(5)	67.7(1)	0
B23 mol%	0	7.63(8)	0	45.8(1)	0	2.31(9)	9.44(5)	34.82(9)	0	N, 57
wt%	0	5.17(5)	0	18.30(4)	0	1.10(4)	16.58(9)	58.8(2)	0	
B42 mol%	28.4(2)	13.7(1)	0	42.0(2)	0	4.1(2)	0	11.7(1)	0	Y
wt%	13.7(1)	16.7(1)	0	30.3(1)	0	3.5(2)	0	35.7(3)	0	
B49 mol%	40.5(1)	10.5(1)	4.9(1)	31.6(1)	1.85(2)	5.8(2)	0	4.98(3)	0	Y
wt%	24.08(6)	15.8(2)	5.8(1)	28.00(9)	1.53(2)	6.2(2)	0	18.7(1)	0	
B50 mol%	48.72(9)	17.9(4)	0	27(2)	3.15(5)	1.2(3)	0	1.94(9)	0	Y
wt%	31.84(6)	29.6(7)	0	26(2)	2.86(5)	1.4(4)	0	7.9(4)	0	
B56 mol%	33.59(3)	9.03(3)	0	49.47(4)	3.73(2)	1.28(3)	0	2.9(1)	0	N, 79
wt%	21.54	14.65(5)	0	47.29(4)	3.33(2)	1.46(3)	0	11.71(4)	0	
B59 mol%	20.7(1)	1.51(5)	0	62.5(2)	3.85(5)	9.5(5)	0	2.04(3)	0	Y
wt%	13.53(8)	2.49(9)	0	61.0(2)	3.51(4)	11.1(6)	0	8.4(1)	0	
B66 mol%	43.6(2)	8.98(7)	2.13(3)	35.7(1)	1.32(2)	5.8(4)	0	2.52(2)	0	Y
wt%	28.7(1)	15.0(1)	2.79(4)	35.1(1)	1.21(2)	6.8(5)	0	10.46(8)	0	
B72 mol%	37.2(2)	8.71(4)	nd	41.4(2)	1.55(1)	3.3(4)	1.51(1)	0	6.37(2)	Y
wt%	24.2(2)	14.33(6)	nd	40.2(2)	1.40(1)	3.8(4)	6.42(6)	0	9.69(3)	
B77 mol%	41.6(1)	9.86(8)	0.7(1)	34.0(2)	1.68(1)	5.5(9)	1.10(2)	0	5.6(1)	Y
wt%	27.54(9)	16.5(1)	1.0(1)	33.6(2)	1.55(1)	6(1)	4.79(9)	0	8.6(2)	
B83 mol%	45.8(3)	8.34(6)	0.8(1)	28.5(4)	1.32(2)	9(1)	1.355(2)	0	5.10(3)	Y
wt%	30.7(2)	14.1(1)	1.1(2)	28.5(4)	1.23(2)	10(1)	5.95(1)	0	7.99(5)	
B85 mol%	36.0(2)	7.33(4)	0	40.49(7)	3.16(3)	7.8(4)	0.931(9)	0	4.28(7)	Y
wt%	24.1(2)	12.43(7)	0	40.42(7)	2.95(2)	9.3(5)	4.09(4)	0	6.7(1)	
B91 mol%	37.6(1)	13.00(3)	0	29.33(9)	3.03(5)	10.8(2)	1.86(4)	0	4.33(3)	N, 151
wt%	23.51(7)	20.55(5)	0	27.32(9)	2.63(4)	12.0(3)	7.6(2)	0	6.32(4)	

Silicate melt compositions in both mole percent and weight percent assuming U is in the 2+ oxidation state (see text). Errors are either the standard errors of the average or the error from the point spread analysis. Elements with 0 percent were not present in the sample material; nd means the oxide was not detectable. [†]Fit with point spread function (Yes/No). If no, number of measurements are included.

outside the silicate melt is lower than that measured in the metal. We therefore conclude that secondary fluorescence has not compromised our measurements of lithophile elements in the metal phase in these experiments.

3.3 Discussion

3.3.1 Thermodynamic modeling and the oxidation state of U

Partition coefficients for any trace element (M) between liquid metal and silicate melt phases are defined as

$$D_M = \frac{X_{M,metal}}{X_{MO_{n/2},silicate}} \tag{3.2}$$

where X_i are the mole fractions of those species in their respective phases and n is the oxidation state of the metal cation in the silicate melt. The partition coefficient is not only dependent on thermodynamic variables such as temperature and pressure, but also on composition and the fO_2 of the system. Because of this, a multivariate approach is necessary to address all of the variables simultaneously. The dependence on redox condition is best described by considering the exchange reaction

$$MO_{n/2} + \frac{n}{2}Fe \rightarrow \frac{n}{2}FeO + M \tag{3.3}$$

in which the cation of interest (having valence n) is reduced to a metal by exchanging oxygen with iron, the most abundant multivalent element in Earth's interior. The exchange coefficient (K_D) for this reaction,

$$K_D^M = \frac{\frac{X_M}{X_{MO_{n/2}}}}{(\frac{X_{Fe}}{X_{FeO}})^{n/2}} = \frac{D_M}{(D_{Fe})^{n/2}} \tag{3.4}$$

is thus a useful means of describing the dependence of partitioning on P, T, and composition of the various phases independent of the redox state. However, use of the exchange coefficient

requires that the oxidation state of the cation be assumed or inferred from the fit to the data. Previous studies (Malavergne et al., 2007; Bouhifd et al., 2013) have inferred an oxidation state for U of 4+, which is reasonable given that the most reduced form of natural U at surface conditions is 4+. However, this assumption did not work well for fitting the combined high-pressure and low-pressure data for U here.

When fitting the dependence of partition coefficient (D_U) on fO_2 explicitly, as in Eq. 3.5,

$$Log_{10}D_U = a + \frac{b}{T} + c\frac{(1-X_S)^2}{T} + d\frac{(1-X_{SiO_2})^2}{T} + e\Delta IW, \tag{3.5}$$

we find that the U oxidation state within the silicate liquid at these conditions is best described as 2+, instead of the 4+ valence that has previously been inferred. Here, X_i is the mole fraction of species i, and a and b are representative of the entropy and enthalpy of the reaction in Eq. 3.3, respectively. The compositional terms are expressed as the excess Gibbs free energy of mixing in a Guggenheim-type binary mixing model (e.g. Ganguly (2009)), where the log of the activity coefficient (γ_i) equals a constant times (1-X_i)^2/T. Equations 3.5 and 3.6 neglect terms that were found to be statistically insignificant to the partitioning of U, including pressure and other compositional effects, discussed later. In this notation, the coefficient e is equal to negative one quarter of the U oxidation state in the silicate liquid. The parameters for this fit are listed in Table 3.5, where e = -n/4 = -0.49. Thus, the inferred oxidation state, n, for U in the silicate melt is indeed 2+. To show this result more explicitly, we corrected all of the data using the fitted parameters in Eq. 3.5 to single temperature (3000 K), S content in the metal

Table 3.4: Metal–silicate partitioning and exchange coefficients for U.

Sample	D_U	K_D^U
B22	0.0328(3)	0.00294(5)
B23	0.0441(3)	0.00216(9)
B42	0.039(1)	0.0032(2)
B49	0.662(4)	0.114(4)
B50	0.23(1)	0.005(1)
B56	0.042(2)	0.00107(5)
B66	0.230(4)	0.020(2)

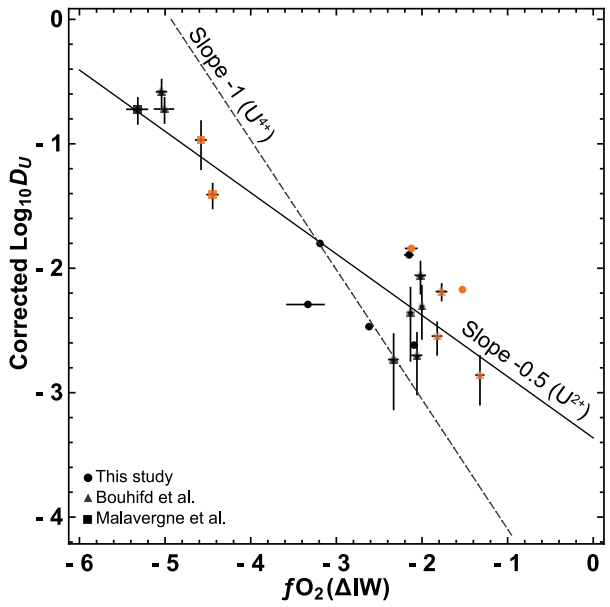

Figure 3.4: Plot of partition coefficients as a function of fO_2(ΔIW). Orange symbols are sulfur-containing samples. All of the data have been corrected to a single P-T-X condition. Lines of slope -1 (indicating U^{4+}) and -0.5 (indicating U^{2+}) are included for reference.

(2 wt%, mole fraction = 0.033) and SiO_2 content in the silicate (45 wt%, mole fraction = 0.382). These data were then plotted in Fig. 3.4 as corrected $Log_{10}D_U$ versus the measured ΔIW values. The slope of this line is indeed -0.49, consistent with U^{2+}. A line with slope of -1 (indicating a 4+ oxidation state for U) is also shown for reference. The data from this study used in this regression are listed in Table 3.4.

Divalent uranium has only been previously observed using relatively exotic organometallic synthesis methods (MacDonald et al., 2013). Our result is consistent with recent experiments that have reported a reduction in oxidation state of two other high-field strength elements, Nb and Ta, in silicate melts at 5 GPa under reducing conditions (Cartier et al., 2014, 2015). These results indicate that metal–silicate partitioning of these elements is less dependent on fO_2 at high P-T conditions. This change in U valence could result in a difference in metal–silicate partitioning behavior between U and the other radioactive elements (described below). This is also likely important for mineral–melt partitioning of these elements at depth within the Earth, as cations with lower field strength are more

Table 3.5: Metal–silicate partitioning parameters fit to Eqs. 3.5 and 3.6 for U. The root-mean-square (RMS) misfit to the data is 0.31 log units in both cases.

	Equation 5		**Equation 6**	
Parameter	**Value**	**Error (±)**	**Value**	**Error (±)**
a	0.1	0.3	0.1	0.3
b	-11,000	1000	-11,000	1000
c	-4700	900	-4700	800
d	13,000	3000	13,000	3000
e	-0.49	0.07	–	–

likely to be compatible in mantle minerals (Blundy and Wood, 2003a).

A comparison of our high-pressure exchange coefficients to earlier work (Malavergne et al., 2007; Bouhifd et al., 2013) in Fig. 3.5 shows a strong dependence of K_D^U on temperature. This dependence was not discernible in earlier studies, likely because of the relatively small pressure and temperature ranges previously investigated. Much of the apparent scatter in Fig. 3.5 relates to other factors, besides temperature, that affect the metal–silicate partitioning of U. To parse the dependence of partitioning on pressure, temperature and chemical composition of the metal and the silicate, the K_D^U data were fit to an equation of the form

$$log_{10}K_D^U = a + \frac{b}{T} + c\frac{(1-X_S)^2}{T} + d\frac{(1-X_{SiO_2})^2}{T} \tag{3.6}$$

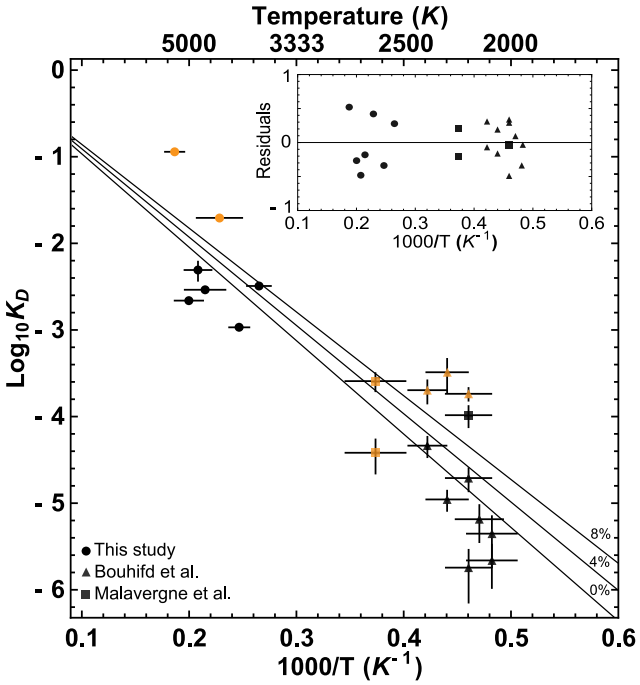

Figure 3.5: Temperature dependence of metal–silicate partitioning of U. Orange symbols are sulfur-containing samples. Solid lines represent the expected exchange coefficients at constant sulfur content in the metal in weight percent. Inset: Residuals to the fit.

where the coefficients are thermodynamically equivalent to those in Eq. 3.5, except that the fO_2 term is accounted for in K_D^U. These coefficients are listed in Table 3.5, and are found to be identical to those in Eq. 3.5.

Our results show that, within the range of conditions appropriate to core formation in Earth, temperature is the factor that most strongly influences metal–silicate partitioning of uranium. Sulfur in the core appears to be favorable for U partitioning into the metal, while SiO_2 in the silicate has a strong negative effect. In this context, SiO_2 content of the silicate melt is a proxy for how polymerized the melt is, which is often a

consideration in partitioning studies at lower pressures and temperatures as "non-bridging oxygens per silicate tetrahedron (nbo/t)" (Mysen, 1991; O'Neill and Eggins, 2002; Righter, 2003). The effect of pressure was found to be insignificant, and is not included in the reported parameterization.

The concentrations of UO_2 in the silicate melts of these samples are far greater than the very low (ppb to ppm) levels that occur in natural silicates. This was necessary, as the available techniques for measuring composition at such high spatial resolution do not have the capability of detecting elements at such low concentrations. Consequently, it is important to consider that these samples may not fall within the Henry's Law range of chemical activity; i.e. the activity of U, and therefore its partitioning behavior, is different (either higher or lower) than it would be in nature. This would be accounted for in the thermodynamic model in the same way that we have accounted for S and SiO_2, with a coefficient on the composition term to describe the non-ideality of the solution. Despite the range of UO_2 (or U) concentrations in the silicate (or metal), it was found that such a term was not statistically significant. In addition, we tested the Henry's Law assumption by completing four otherwise identical metal–silicate partitioning experiments in a large-volume press with a range of UO_2 contents in the silicate melt. Fig. 3.6 shows the results from these experiments. We see no trend of D_U as a function of U concentration in the silicate, thus we concluded that there is not a strong dependence of U partitioning of U content of the silicate. Likewise, it was found that additional terms in equations 3.5 and 3.6 to account for the Si content for the metal were also not significant.

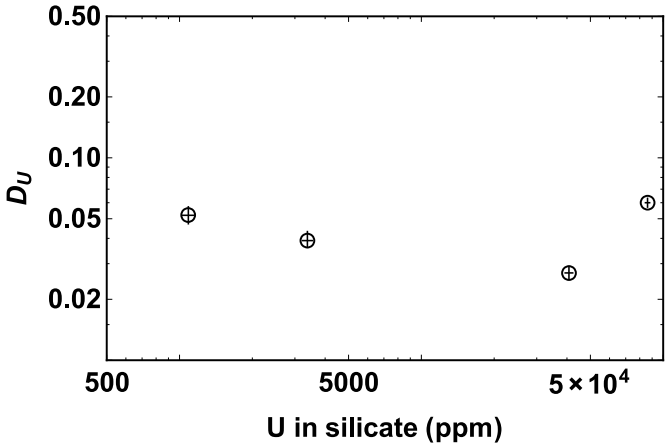

Figure 3.6: Evaluation of Henry's Law for U partitioning. There is no trend in D_U as a function of U content of the silicate melt, thus Henry's Law holds.

Thus, the activity coefficients of UO_2 and Si appear not to vary strongly over the range of compositions explored in this study, and we tentatively conclude that Henry's Law violations do not impact our results.

In all the experiments described here, as well as many of those reported in the literature, the metallic phase has the opportunity to be completely saturated in carbon due to reaction with the sample containment (either graphite capsules in multi-anvil or piston cylinder press, or diamonds in the diamond anvil cells). Unfortunately, in addition to being a ubiquitous environmental contaminant, C is difficult to measure using the spectroscopic techniques described here. However, there is very little evidence that C is actually an important factor for metal–silicate partitioning of U. The interaction parameter between C and U in a C-saturated iron alloy is listed in the Steelmaking Data Sourcebook as 0 at temperatures around 1600-1700 K (Japan Society for the Advancement of Science and the 19th Committee on Steelmaking, 1988). Furthermore, Bouhifd et al. (2013) completed metal–silicate partitioning experiments of U at moderate pressures in both MgO and graphite capsules and found C to have a negligible effect. They, along with others (Miettinen, 1998; Kawanishi et al., 2009; Li et al., 2015), show that the C and Si contents of the metallic phase are inversely correlated. Thus, given the high Si contents of the metals in our study, and the negligible interaction between U and C, we expect our parameterization to be accurate without including a parameter for the effect of C content.

3.3.2 Thermodynamic modeling of the metal–silicate partitioning of other lithophile elements (K, Th, and Mg)

In addition to U, K and Th are also important radioactive heat-producing elements in the deep Earth. Experiments of the type described above were undertaken to determine the metal–silicate partitioning behavior of these elements. Partition and exchange coefficients were calculated for both K and Th using equations 3.2 and 3.4, assuming oxidation states of +1 (K) and +4 (Th). Those results are listed in Tables 3.6 and 3.7.

Several studies have investigated the metal–silicate partitioning of K in the past (e.g. Bouhifd et al. (2007); Corgne et al. (2007); Gessmann and Wood (2002); Hirao et al. (2006); Murthy et al. (2003); Watanabe et al. (2014)). When determining which of these studies to compare with our data, particular care had to be taken. To begin, Murthy et al. (2003) noted that much of the inconsistency amongst previous studies could be attributed to leaching of K from the metallic phases during polishing under oil when preparing samples for chemical analysis. Because we could not constrain the amount of leaching in every experiment, we chose not to include any data reported prior to 2003. Additionally, many of the studies used silicates with very high K content, sometimes even up to stoichiometric K-feldspar compositions (e.g. $KAlSi_3O_8$) (Bouhifd et al., 2007; Hirao et al., 2006; Watanabe et al., 2014). This material is more representative of continental crust than bulk silicate Earth, and likely falls outside the Henry's Law regime. We confirmed this by thermodynamically parameterizing the combined K data as a function of X_{K_2O}. When experiments with very K-rich silicates were included in the parameterization, we found a strong dependence of partitioning on K content, which suggests that the activity of K in those experiments was not representative of K in a deep mantle silicate melt. Unfortunately, these high-K experiments included the only studies that reached P-T conditions relevant to a magma ocean. However, when we closely examined images of the samples reported in these studies, we determined that they did not exhibit the texture expected of a sample taken to temperatures above the silicate liquidus. Thus, these experiments were not representative of a truly magma ocean scenario anyway. For these reasons, these samples were also excluded from

Table 3.6: Metal–silicate partitioning and exchange coefficients for K.

Sample	D_K	K_D^K
B72	0.0117(4)	0.0029(3)
B77	0.026(1)	0.007(1)
B83	0.040(1)	0.016(2)
B91	0.015(1)	0.0062(3)

Table 3.7: Metal–silicate partitioning and exchange coefficients for Th.

Sample	D_{Th}	K_D^{Th}
B72	0.024(1)	0.00008(2)
B77	0.044(4)	0.00025(9)
B83	0.092(3)	0.0026(6)
B91	0.026(2)	0.00086(8)

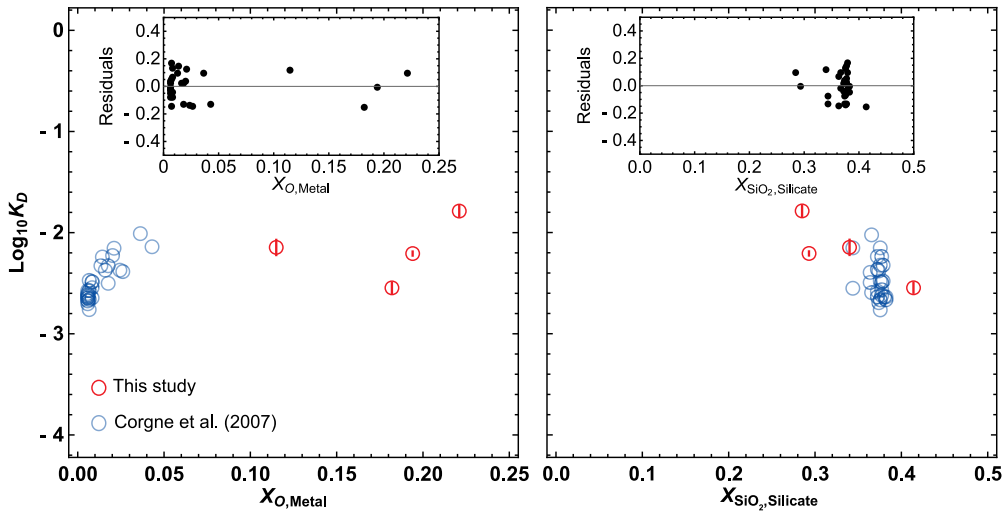

Figure 3.7: Exchange coefficients for K as a function of **Left** O content in the metal, and **Right** SiO_2 contents of the silicate melt

our analysis.

The one study that met all of our criteria was from Corgne et al. (2007), which reached 7.7 GPa. By combining our high P-T data with their lower pressure data, we were able to thermodynamically parameterize the metal–silicate partitioning of K as in Eq. 3.7. The coefficients $(a - e)$ are listed in Table 3.8.

$$log_{10} K_D^K = a + b\frac{(1 - X_S)^2}{T} + c\frac{(1 - X_{Si})^2}{T} + d\frac{(1 - X_O)^2}{T} + e\frac{(1 - X_{SiO_2})^2}{T} \tag{3.7}$$

We find the strongest dependence of K partitioning is on the chemical composition of the metal phase (Eq. 3.7). Partitioning is positively dependent on O and S content of the metal and negatively dependent on Si content of the metal and SiO_2 content of the silicate melt. As is the case with U partitioning, the SiO_2 content is likely a proxy for how polymerized the silicate melt is. The only discernible dependence on temperature is within the non-ideal mixing terms and there was no dependence on pressure. There is, however, a hidden dependence of partitioning on pressure and temperature here, as the metal–silicate partitioning (and therefore the resulting concentration) of O, Si, and S have all been shown to be dependent on these variables (Frost et al., 2010; Boujibar et al., 2014; Fischer et al., 2015).

This is further complicated because, as was briefly mentioned in Section 3.3.1, the partitioning of these light elements has been shown to be dependent upon the concentrations of one another (Boujibar et al., 2014; Fischer et al., 2015).

To date, no metal–silicate partitioning experiments have been reported for Th. Of the seven experiments we conducted that contained Th, only four had measurable Th in the metal phase (maximum concentrations for the other three are listed in Table 3.2). When parameterizing our data, we were unable to extract a dependence of partitioning of Th on any thermodynamic or compositional variables (e.g. see Fig. 3.8). This is likely due to the relatively narrow range of conditions under which the experiments were performed. Therefore, we chose to treat the partitioning behavior of Th as an average of the four experiments, as in Eq. 3.8.

Table 3.8:
Metal–silicate partitioning parameters fit to Eq. 3.7 for K. The root-mean-square (RMS) misfit to the data is 0.095 log units.

Parameter	Value	Error (±)
a	-2.6	0.2
b	-500	200
c	8000	3500
d	-11000	3000
e	9000	3000

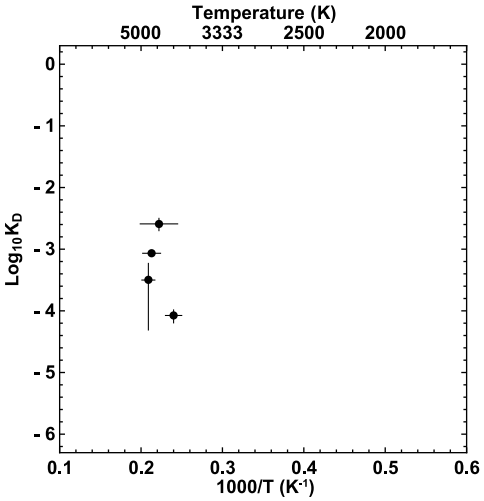

Figure 3.8: Exchange coefficients for Th as a function of temperature.

$$log_{10}K_D^{Th} = -3.3(3) \tag{3.8}$$

This is reasonable because the conditions at which those experiments were conducted are similar to the average conditions in a magma ocean, so very little extrapolation is necessary when modeling core formation.

One more lithophile element that is predicted to be important for energy production in the core is Mg (O'Rourke and Stevenson, 2016; O'Rourke et al., 2017; Badro et al., 2016). This element has recently been recognized as a possible contribution to the light element budget of the core, at least early in Earth's history, as metal–silicate partitioning experiments

are being completed at higher P-T conditions with the advent of focused-ion-beam nanofabrication techniques allowing for the recovery of small diamond anvil cell samples. It was shown by Badro et al. (2016) that the partitioning behavior of Mg is strongly dependent upon temperature. We confirm this finding, although when our data are compared directly with the previous study, we observe a systematic offset of their exchange coefficients as a function of temperature (Fig. 3.9). It is unclear what is causing this offset, as the P-T conditions of the two studies are quite similar. There is, however, a noticeable difference in silicate melt composition between the two studies. Many of the samples in the previous study contain more FeO and less MgO in the silicate, although the O and Fe contents of the metal are not drastically different as would be expected if the high FeO is due to the exchange reaction in Eq. 3.3. Unfortunately, this compositional difference was unable to account for the observed offset in the data and we chose to thermodynamically parameterize our data alone. We find that indeed, the strongest dependence of metal–silicate partitioning of Mg is temperature, with a slight dependence on pressure and a negative dependence on Mg content in the silicate melt (Eq. 3.9). The data used in this regression can be found in Table 3.9.

Table 3.9:
Metal–silicate partitioning and exchange coefficients for Mg.

Sample	D_{Mg}	K_D^{Mg}
B42	0.027(2)	0.0023(2)
B49	0.0722(4)	0.0124(4)
B59	0.009(1)	0.0013(2)
B66	0.0243(8)	0.0021(2)
B72	0.0256(2)	0.0015(2)
B77	0.043(1)	0.0032(6)
B83	0.057(1)	0.009(1)
B85	0.0051(6)	0.00051(7)
B91	0.0269(7)	0.0049(2)

$$log_{10}K_D^{Mg} = a + \frac{b}{T} + c\frac{P}{T} + d\frac{(1 - X_{MgO})^2}{T} \tag{3.9}$$

In this case, it is reasonable to have a dependence of partitioning upon the MgO content of the silicate melt. MgO makes up a significant portion of the silicate melt which would have an effect on the silicate melt characteristics, unlike the trace elements described above.

3.3.3 Core formation at a single effective pressure and temperature

Table 3.10:

Metal–silicate partitioning parameters fit to Eq. 3.9 for Mg. The root-mean-square (RMS) misfit to the data is 0.13 log units.

Parameter	Value	Error (±)
a	0.03	0.6
b	-18,000	3500
c	54	20
d	10,000	4000

We use the parameterization of metal–silicate partitioning of lithophile elements described above with a core/mantle differentiation model to place bounds on their content of the Earth's core. Our model uses average P-T conditions of core-mantle equilibration (Siebert et al., 2012; Fischer et al., 2015), that is P = 45-58 GPa and T = 3900-4200 K (the liquidus of peridotite from Fiquet et al. (2010)), with the core and mantle composition from McDonough (2013) and Arevalo et al. (2009) (i.e. a conservative 2 wt% S in the core and a current 20 ± 8 ppb U, 80 ± 25 ppb Th, and 280 ± 120 ppm K in the bulk silicate Earth (BSE)), and an fO_2 of IW-2. It is important to note that these calculations were done for the age 4.5 Ga, meaning the concentrations of each radioactive isotope are greater in our calculations than the current values. For example, starting with a current 20.3 ppb U in the BSE and integrating back through time, the U content in the initial BSE equaled 53.7 ppb. The O and Si content in the core are calculated using the parameterization in Fischer et al. (2015), which results in a lower bound of 1.1 wt.% O and 14 wt.% Si and an upper bound of 1.2 wt.% O and 22 wt.% Si at these P-T conditions. The SiO_2 content of the mantle ranges between 35-42 wt.% de-

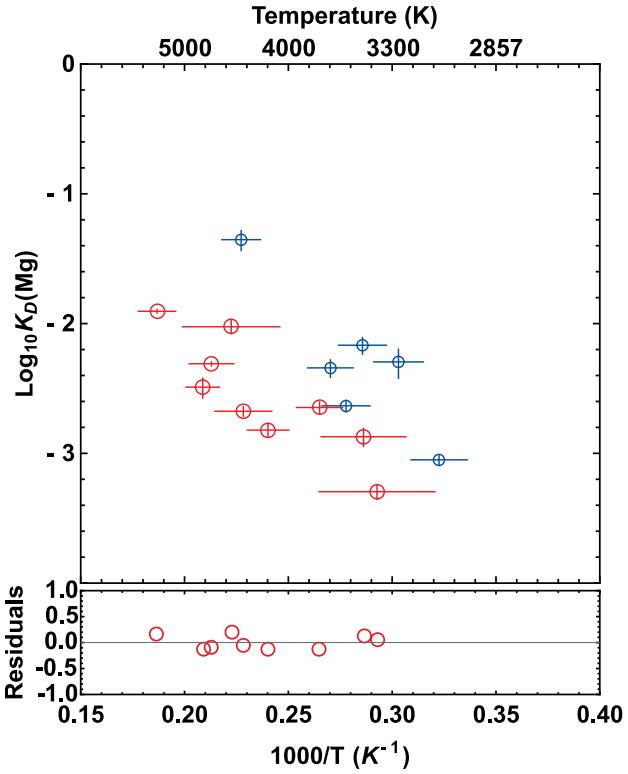

Figure 3.9: Exchange coefficients for Mg as a function of temperature. Red symbols are from this study, blue symbols are from Badro et al. (2016). Bottom panel contains residuals to the fit of the data from this study to Equation 3.9.

pending upon the conditions under which Si is partitioned into the core. Under these conditions, we calculate partitioning of U in the differentiating planet to be $D_U = 0.035$ (+0.04/-0.02) to 0.099 (+0.1/-0.05), resulting in a concentration of 3-9.7 ppb U in the core. Thus, the heat production from U at 4.5 Ga is predicted to be 1.2 (+1/-0.6) to 4.4 (+4/-2) TW (Turcotte and Schubert, 2002) depending upon the temperature of equilibration at the base of a magma ocean.

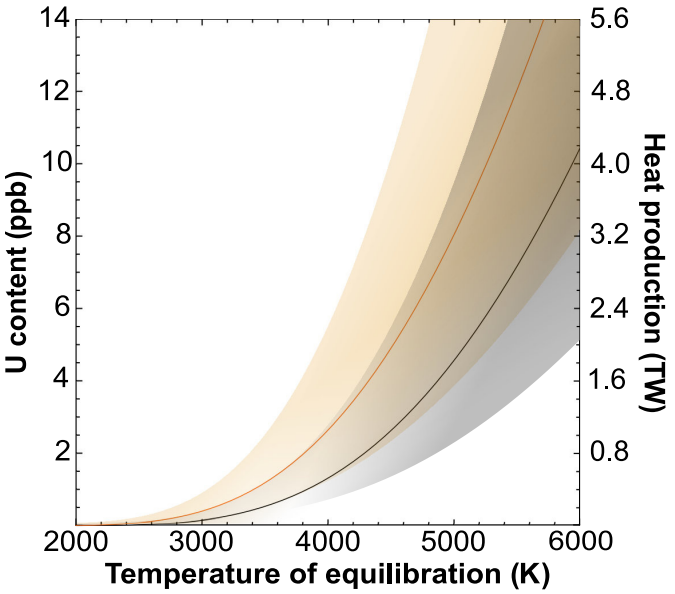

Figure 3.10: U content and the resulting heat production at the onset of core formation as a function of metal–silicate equilibration temperature assuming an SiO_2 content of 45 wt% in the silicate melt. Black line: 0 wt% S in the metal; orange line: 8 wt% S. Error envelopes are derived from the root-mean-squared error on the fit.

We confirm the strong dependence of U partitioning on S content of the core discussed by previous studies (Malavergne et al., 2007; Bouhifd et al., 2013; Wohlers and Wood, 2015). Raising the sulfur content of the metal to an extreme upper bound of 8 wt% elevates the amount of U initially partitioned into the core at an average temperature of 4200 K to 14.5 (+13/-7) ppb, corresponding to 6.6 TW of heat. We emphasize, however, that based on our results high sulfur contents alone cannot produce a significant radiogenic heat source by partitioning U into the core. Figure 3.10 shows the amount of U partitioned into the metal as a function of temperature of metal–silicate equilibration with 0 and 8 wt% S at a fixed SiO_2 content of 45 wt% in the mantle. The amount of U in the core increases dramatically above 4000 K, temperatures that would be expected subsequent to a large impact (Canup et al., 2015) or in a basal magma ocean (Fiquet et al., 2010). While our experiments did not investigate the sulfide–silicate partitioning behavior of U and they may not be directly comparable to

the Wohlers and Wood (2015) study, they do suggest that putting significant amounts of U into the core by including a large fraction of sulfide material early on is unlikely, because the temperatures early on were significantly lower than at later stages of core formation.

For K, the calculated partition coefficients are relatively constant at 45-58 GPa (3900-4200 K), D_K = 0.0017 (+0.0004/-0.0003) to 0.0015 (+0.0004/-0.0003), which results in approximately 0.8 ppm K in the core. This is several orders of magnitude lower than the 300 ppm K used in previous core energy budget models (e.g. Nimmo (2015)). The radioactive isotope of potassium, ^{40}K, is 0.012% of the total K currently and was 0.15% at 4.5 Ga. So, only about 0.0012 ppm of the K in the core translates to heat production, resulting in ∼0.07 TW. As discussed above, although K partitioning does not depend upon pressure or temperature directly, the K content in the core decreased for the higher P-T condition because of its strong negative dependence on Si content in the metal, which increased significantly at the higher P-T condition. K partitioning is also dependent upon S content, but to a much lesser degree than U. At 45 GPa and 3900 K, raising the S content of the metal to 8 wt%, D_K = 0.0018, which is a negligible change in terms of heat production. Furthermore, K is a volatile element, so its abundance within the BSE is estimated based on measurements of the K/U ratio in various crust and mantle reservoirs. Since the error on U in the BSE is ∼40%, so is the error on K contents. However, it is clear that even a doubling of K within the BSE would result in << 1 TW of heat within the core. The partitioning of Th is being treated as a constant, so its partition coefficient at all P-T conditions is D_{Th} = 0.05 (+0.1/-0.04), which puts ∼8 (+18/-6) ppb Th into the core, resulting in 0.4 (+0.9/-0.3) TW of heat. As discussed above, the partitioning of Mg is strongly dependent on the temperature of metal–silicate equilibration. The partition coefficients for Mg are D_{Mg} = 0.0057 (+0.002/-0.001) to 0.010 (+0.004/-0.003), putting 0.14-0.31 wt% Mg into the core. Since Mg is not a radioactive heat source, the Mg contents does not translate directly into heat. The effect this light element has on the energy budget of the core will be addressed in the following chapter.

The expected amounts of these elements in the core are different if the calculations are done using the liquidus of Andrault et al. (2011), because their temperature profile was measured on a different composition (chondritic) and is lower than that of Fiquet et al. (2010), which was measured on peridotite. For example, using 3400 K, the liquidus temperature at 58 GPa from Andrault et al. (2011), and 2 wt% S (45 wt% SiO_2), the core's contents of U and Mg decrease to 0.7 ppb and 0.09 wt.%, respectively. Th is about 50% that using the higher liquidus profile. In contrast, the K content increases slightly at these conditions to 1.53 ppm. The total radiogenic heat production in the core under these lower temperature metal–silicate equilibration conditions is about 0.6 TW. Importantly, changing the average temperature of core formation by 500 K, which is well within the uncertainty of the conditions of this process, decreases the radiogenic heat production by an order of magnitude.

3.3.4 Core formation under a range of pressures and temperatures

Modeling core formation at a single representative pressure and temperature, as above, is useful for comparison between partitioning studies, as well as for direct observation of the effects of the various fitting parameters. However, the compositions of the core and mantle were set under a range of equilibrium conditions, so it is more rigorous to model core formation as a series of equilibration steps of evolving conditions. We performed a "growing-Earth" model as described in Fischer et al. (2015), but used the liquidus profile of Fiquet et al. (2010) and added S to the core, for consistency with the single P-T model above. In this model, metal and silicate liquids fully equilibrate at 50% the CMB pressure at each step, reaching a maximum pressure of 70.5 GPa. Two starting compositions were used: a "reduced Earth" and an "oxidized Earth". For the reduced Earth, the initial fO_2 was set at IW-3.5 which evolved to IW-1.96 because of the high P-T reactions that drive redox exchange between Fe and Si, changing the internally buffered oxygen fugacity as the planet grows. The oxidized Earth started at IW-1.5 and evolved to IW-1.36. The U, Th, K, and

Mg parameterizations were added to this model, along with the parameterizations found in Table 2 of Fischer et al., 2015. The greatest discrepancy between this model and the single P-T model described above is that a much lower Si content in the core results from the growing Earth model (i.e. 3-8 wt. % as opposed to 14-22 wt% above), which greatly affects the partitioning of U and K. Additionally, the oxygen content in the core resulting from the oxidized model is about twice as high as both the single P-T and reduced growing Earth model at all conditions. Even so, the results of both the reduced and oxidized models are similar to our single P-T case. A reduced Earth with 2-8 wt% S in the core would result in 1.5-2.4 ppb U, ∼14.9 ppb Th, 1.2-1.3 ppm K, and 0.13 wt% Mg, which amounts to 1.3-1.6 TW of radiogenic heat in the core. Naturally, the oxidized case results in slightly different lithophile contents. With the same S content, we would expect 1.0-1.6 ppb U, ∼1.47 ppb Th, 3.93-4.15 ppm K, and 0.15 wt.% Mg in the core, resulting in 0.44-0.56 TW of heat production.

3.4 Implications

Based on these results, U, along with contributions from K and Th, could exist to a much greater extent within Earth's core than previously believed. Given the large uncertainties in core energy and entropy models (Nimmo, 2015), it is difficult to say precisely how important this radiogenic heat source would be. The models agree that radiogenic heat contributes to the energy budget, but that it is an inefficient source of entropy available to drive the magnetic field. The high core mantle boundary (CMB) heat flow required for a thermally driven dynamo results in a very young inner core, likely less than 1 Gyr. Integrating back through time, the high heat flow would derive from very high CMB temperatures, and therefore result in extensive to complete mantle melting, through much of Earth's history. A radioactive heat source would allow the core to cool more slowly and inner core to be somewhat older. Most importantly, this heat source would make the early CMB temperature lower, which would curb mantle melting. A discussion of how this radiogenic heat source

contributes to the energy budget of the core through geologic time can be found in the following chapter.

A different but important implication of this work is the effect metal–silicate partitioning of lithophile elements may have for geochemical observations at the surface. First, the relative abundances of the refractory lithophile elements (including U and Th) to one another in the BSE are generally assumed to be chondritic, although there is some discussion as to whether this is actually the case (e.g. Boyet and Carlson (2005, 2006, 2007); Javoy et al. (2010); Jackson and Jellinek (2013)). The Th/U ratio in the BSE as estimated from measurements of various geochemical reservoirs is approximately consistent with this chondritic Earth assumption at 3.8-4.2 (Palme and O'Neill (2013) and references therein). The value used in our model, based on the measurements of McDonough and Sun (1995), is 4 ± 2. In keeping with the chondritic Earth assumption, the metal–silicate partitioning of U and Th must be similar enough that the resulting Th/U ratio in the mantle is not greatly disturbed. Using our growing Earth models, the resulting Th/U values are a little on the high end at 4.1-4.2, but are still well within the error. The single stage core formation model at 58 GPa, 4200 K, and with 8 wt% S in the core can be ruled out based on its resulting Th/U of 4.45, still within uncertainty of the observed value. However, the more conservative models suggest that core formation should not leave an imprint on the mantle in terms of Th/U ratio.

Furthermore, the major isotopes of U (235,238) and Th (232) all undergo radioactive decay to isotopes of Pb (207, 206, and 208, respectively), and the difference in chemistry between these elements has important chronological consequencyes. Additionally, the average Pb isotope composition of surface samples falls to the radiogenic end of the meteorite isochron (see Connelly and Bizzarro (2016) or Allègre (1968) for example). Since much of the solar system material is believed to have formed at the same time, it follows that there must be a hidden reservoir within the Earth that is depleted in radiogenic lead. This is known as the "First Lead Paradox" (Allègre, 1968). One hypothesis is that, since Pb is

more chalcophile than U at ambient conditions and the core likely contains some S, then the core could be the hidden reservoir. This hypothesis also provides a mechanism by which to date the formation of the core, since that should provide the correction between the surface rocks and the meteorite isochron. It is difficult for us to say how our results will impact the current understanding of U-Th-Pb systematics because we do not provide constraints on the Pb content of the core. However, we can show that the assumption that the core contains absolutely zero radioactive elements is too simplistic.

3.5 Conclusions

We have completed metal–silicate partitioning experiments on U, Th, K, and Mg at pressures between 38 and 88 GPa and up to 5400 K, higher P-T conditions than have previously been reported, and exceeding the mean conditions at which Earth's core formed. The experiments were performed at a range of fO_2 states, from IW-3.3 to IW-1.5. We found that U becomes significantly more siderophilic at high temperatures and S contents, such that it could have been an important heat source in the energy and entropy budget of the early core. Differentiation at mean conditions of 58 GPa, 4200 K and 8 wt% S in the metal (an extreme end-member composition) would result in a maximum of 6.6 TW of heat. The metal–silicate partitioning behavior of K is much less dependent upon pressure and temperature, but responds to compositional constraints, which are dependent upon P-T conditions of core–mantle equilibration. From our parameterization, we would expect K to contribute <0.1 TW of heat early in geologic time. Due to the narrow range of experimental conditions here, partitioning of Th was treated as a constant. We find that up to 14 ppb Th could exist in the core, but it releases relatively little heat per mass, so its heat production in the core is limited to a maximum 0.7 TW. The metal–silicate partitioning of Mg is strongly dependent upon temperature, and a maximum 0.3 wt% of this element could have partitioned. Increasing the temperature of differentiation to 6000 K, such as after a large impact, would increase the U and Mg content in the core substantially.

Additionally, we infer a reduction in the oxidation state of U to 2+ in high-pressure silicate melts, which has not been observed previously in natural samples. A lower valence could enhance the partitioning of U into the core at these extreme conditions. It would also likely affect mineral–melt partitioning of U and may result in a fractionation between U and Th at lower mantle conditions, although it must be relatively minor to stay within the range of chondritic Th/U ratios. These results lead the way for other studies of this type on lithophilic elements including REEs, which would have important implications for the geochemistry of the planet if found to be present at significant levels in the core.

CHAPTER 4

ENERGY AND ENTROPY BUDGET FOR EARTH'S CORE WITH A RADIOACTIVE HEAT SOURCE

4.1 Background

When modeling the core's 1-dimensional energy and entropy budget through geologic time, the inferred initial temperature at the core-mantle boundary is too high to be compatible with subsolidus mantle convection (Jaupart et al., 2007) or petrological observations of Archean komatiites (Grove and Parman, 2004) on the surface. Thus, a radioactive heat source in the core may be required to explain the presence of the geomagnetic field through Earth's history while avoiding this thermal catastrophe.

The generation of the geodynamo is contained within the energy balance of the core as described in Equation 4.1, using the formalism of Nimmo (2015).

$$Q_{CMB} = Q_S + Q_L + Q_G + Q_R \tag{4.1}$$

Here, Q_{CMB} is the heat flux across the core-mantle boundary (CMB). This heat flux acts as a sink of energy from the core and a source of energy to the mantle. The corresponding sources of energy in the core include: secular cooling (Q_S), latent heat release as the inner core solidifies (Q_L), release of gravitational energy as light material rises and denser material sinks through the liquid outer core (Q_G), and heat production as radioactive elements decay (Q_R). This equation ignores negligible terms, including heat of solution (Q_H) and pressure heating (Q_P). The energy driving the magnetic field, known as ohmic dissipation (Φ), occurs entirely within the core, so it does not appear in the energy balance above. However, it is a non-reversible process, so it must be taken into account in the core's global entropy budget

(E), shown in Equation 4.2.

$$E_S + E_L + E_G + E_R = E_\kappa + E_\Phi \tag{4.2}$$

The subscripts in the above equation are equivalent to those in Eq. 4.1, except κ, which is thermal conduction of heat across the CMB, and Φ, which is ohmic dissipation. Generally, the entropy production rate is equal to the corresponding energy flux divided by a characteristic temperature for the process (e.g. $E_L = Q_L \frac{(T_i - T_c)}{T_c T_i}$, where the subscripts i and c represent the inner core boundary (ICB) and the core-mantle boundary (CMB)). For convenience, it is useful to separate out the terms in Eqs. 4.1 and 4.2 that depend on the core cooling rate ($\frac{dT}{dt}$), as in the following equations.

$$Q_{CMB} = Q_R + \tilde{Q}_T \frac{dT_{CMB}}{dt} \tag{4.3}$$

$$E_\Phi = E_R + \tilde{E}_T \frac{dT_{CMB}}{dt} - E_\kappa \tag{4.4}$$

Here, $\tilde{Q}_T$ is equal to the $(Q_S + Q_L + Q_G)/(dT/dt)$, and similarly with $\tilde{E}_T$. As can be seen above, keeping all energy sources constant through time, the entropy available to the geodynamo is whatever is leftover after conduction of heat to the lower mantle (E_κ) . Combining Eqs. 4.3 and 4.4, we find an expression that relates the core heat flow to the entropy available to drive the dynamo:

$$Q_{CMB} = Q_R(1 - \frac{\tilde{Q}_T}{\tilde{E}_T}\frac{1}{T_R}) + \frac{\tilde{Q}_T}{\tilde{E}_T}(E_\Phi + E_\kappa) \tag{4.5}$$

Where T_R is the scaled temperature of radiogenic heat production, $\frac{Q_R}{E_R}$. The magnitude of ohmic dissipation (E_Φ) required to drive the geodynamo at its current strength is largely unknown, with estimates ranging from 20-3000 MW/K (Roberts et al., 2003; Buffett, 2002; Buffett and Christensen, 2007; Kuang and Bloxham, 1997; Labrosse, 2003; Gubbins et al.,

2003; Christensen and Tilgner, 2004; Christensen, 2010; Stelzer and Jackson, 2013). The uncertainty here is due to the very short length scale of ohmic dissipation, which has proven difficult to simulate. This number is often reported as a corresponding energy term, Q_Φ, which again can be estimated by multiplying the entropy production by a characteristic temperature. For the core, this temperature is often taken to be 5000 K; thus, the estimated energy required to drive the geodynamo at its current strength is 0.1-15 TW. It is possible that at least a marginal dynamo could exist as long as E_Φ is near zero or not largely negative, but typically this value is set at a minimum value of 100-200 MW/K or 0.5-1 TW.

Equation 4.5 presents another large uncertainty in the dynamics of the core as the thermal conductivity of iron at outer core conditions is uncertain to within a factor of 2-3. Early estimates of this value were in the range of 35-50 W/mK (Buffett et al., 1996; Roberts et al., 2003; Labrosse, 2003). However, more recent calculations and experiments have suggested a significantly higher value for thermal conductivity, >100 W/mK at CMB conditions (de Koker et al., 2012; Pozzo et al., 2012, 2014; Gomi et al., 2013; Gomi and Hirose, 2015; Gomi et al., 2016; Seagle et al., 2013; Ohta et al., 2016), although this is still an active area of research (Konôpková et al., 2016). Raising the thermal conductivity, and thus the adiabatic heat flow, of iron at these conditions means the entropy available to drive the magnetic field is significantly lower. Mantle dynamics calculations suggest that the maximum allowable heat flux out of the core currently is ∼18 TW (Lay et al., 2008). With this value, and assuming the thermal conductivity, $\kappa = 130$ W/mK, the energy budget can be reasonably balanced by sources deriving from inner core growth, Q_L and Q_g, along with secular cooling, Q_S, to provide an E_Φ of 1095 MW/K. Importantly, this very high heat flux imposes a very high rate of cooling ($\frac{dT}{dt}$) for the core, meaning that the inner core must be very young.

Prior to inner core solidification, the only source of energy and entropy for the geodynamo in the core was secular cooling and possibly radiogenic heat production. Removing inner

core heat sources turns Eq. 4.5 into:

$$Q_{CMB} = \frac{Q_R}{1 + \frac{5}{2}(\frac{L^2}{r_c^2})} + Q_\kappa(1 + \frac{E_\Phi}{E_\kappa}) \tag{4.6}$$

where L is a characteristic length scale ($L = \sqrt{\frac{3K_0(ln\frac{\rho_{cen}}{\rho_0}+1)}{1+2\pi G\rho_0\rho_{cen}}}$), ρ is the density either at the center of the Earth (cen) or at ambient conditions (0), K_0 is the bulk modulus of iron at ambient conditions, G is the gravitational constant, and r_c is the radius of the core at the CMB (Nimmo, 2015). Here we see that if radiogenic heat is negligible, the CMB heat flux prior to the inner core must be superadiabatic to have even a marginal dynamo ($E_\Phi \geq 0$). By integrating Eqs. 4.5 and 4.6 through geologic time, assuming radiogenic heating is negligible, κ is 130 W/mK, Q_{CMB} is currently 18 TW, and fixing E_Φ to 100 MW/K (i.e. the geodynamo existed at present-day strength as suggested by Biggin et al. (2011); Tarduno et al. (2010, 2015)) prior to inner core initiation, we get a picture that looks like Figure 4.1. This model shows that under these conditions, the inner core is as young as 0.5 Gyr and the inferred initial temperature of the core is ∼5700 K. This temperature is high enough that the whole lowermost mantle would have been above the liquidus of mantle material (Fiquet et al., 2010; Andrault et al., 2011) for most of Earth's history, which is not supported by either mantle dynamics simulations or petrological observations of surface rocks.

Furthermore, examination of Eq. 4.6 shows that a radiogenic heat source actually acts to decrease the available entropy within the core, although it is a very inefficient term overall. However, radiogenic heat most strongly affects the core cooling rate, as in the following equation.

$$\frac{dT_{CMB}}{dt} = \frac{Q_{CMB} - Q_R}{\tilde{Q}_T} \tag{4.7}$$

Depending upon the model constraints of the entropy available to drive the magnetic field (E_Φ), thermal conductivity of core material at CMB pressures and temperatures (κ), and current day CMB heat flux (Q_{CMB}), a radiogenic element content upwards of 300 ppm

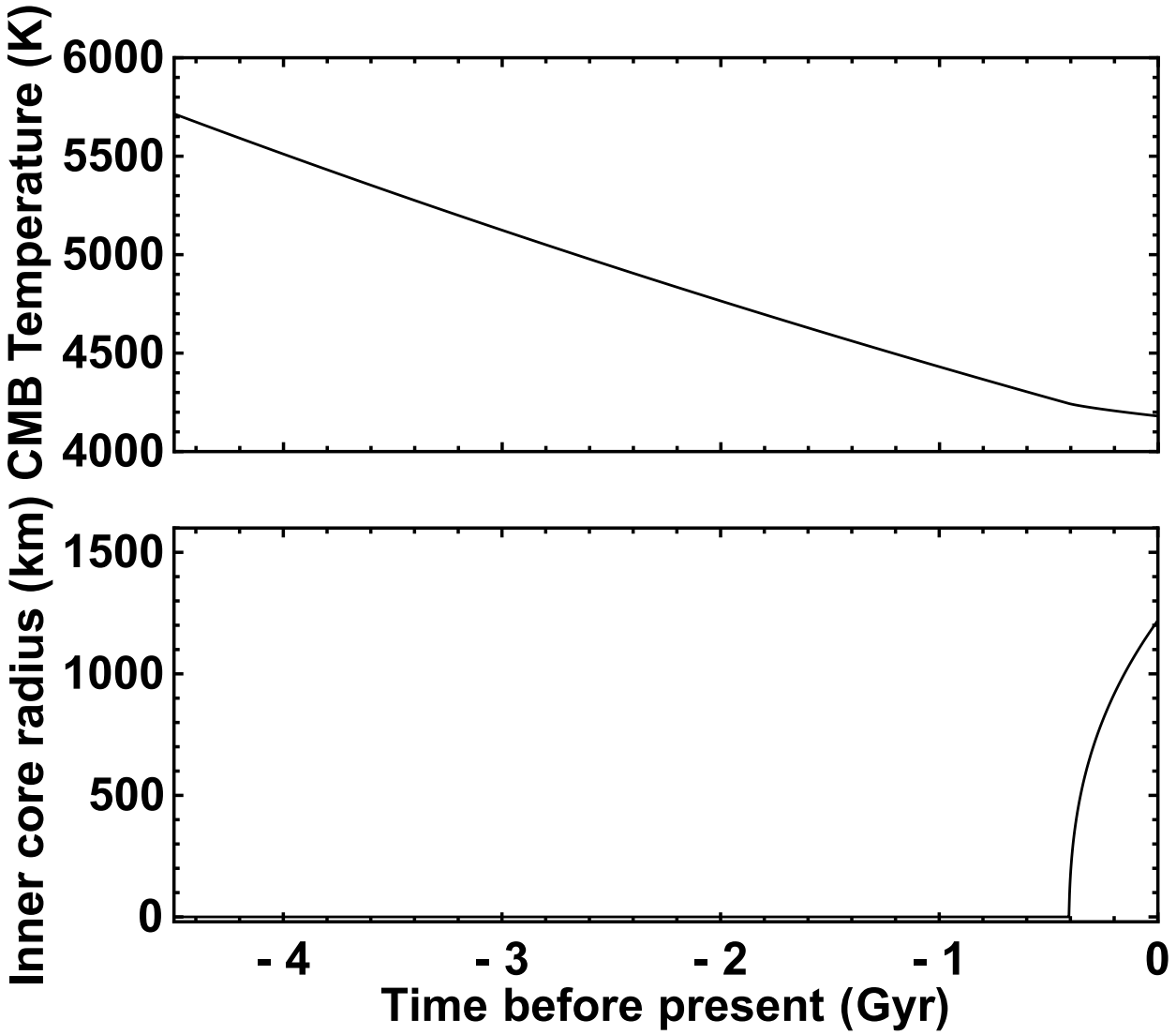

Figure 4.1: Results of a 1-dimensional energy and entropy budget for Earth's core, assuming the ohmic dissipation, or magnetic field strength, is 100 MW/K prior to inner core generation and the thermal conductivity at the core-mantle boundary is 130 W/mK.

K is required to reduce the inferred early Earth CMB temperature to reasonable values (Nimmo, 2015). Whether this is possible based on the chemical behavior of K under core formation conditions was not well constrained previously, and the possibility that other radioactive elements, such as U or Th, may play an important role in this process has not been widely considered. In Chapter 3, I have described metal–silicate partitioning experiments to constrain the chemical behavior of these elements under core-formation conditions to shed some light on their role within the energy balance of Earth's core.

Radioactive element content affects the core's energy and entropy budget by modifying the radiogenic heat source term, Q_R, and its corresponding entropy, E_R. Expanding Q_R assuming radiogenic heat sources are homogeneously distributed, we get Eq. 4.8.

$$Q_R = \int \rho h dV \tag{4.8}$$

Here, ρ is the density of the core and h is the heat production per unit mass in the core. Completing the integration over the volume of the core, we find a simple expression:

$$Q_R = M_c h, \tag{4.9}$$

where M_c is the mass of the core. The corresponding entropy term is slightly more complicated.

$$E_R = \int \rho h (\frac{1}{T_c} - \frac{1}{T}) dV \tag{4.10}$$

Here, T_c is the temperature at the CMB. For simplicity, we choose to define a term I_T as

$$I_T = \int \frac{\rho}{T} dV = \frac{4\pi \rho_{cen}}{3T_{cen}} r_c^3 (1 - \frac{3}{5}\frac{r_c^2}{B^2} + ...), \tag{4.11}$$

where

$$B^2 = (\frac{1}{L^2} - \frac{1}{D^2})^{-1}, \tag{4.12}$$

r_c is the radius of the core, and ρ_{cen} and T_{cen} are the density and temperature at the center of the core, respectively. This integration can be done analytically, but it is sufficient to carry out a series expansion as shown in Eq. 4.11. L and D are characteristic length scales within the core that depend upon the equation of state of core material and describe density variations and adiabatic temperature variations, respectively (see Nimmo (2015) for a precise definition). In this model these parameters are held constant at $L = 7272$ km and $D = 6203$ km. The final entropy expression for radioactive decay is as follows

$$E_R = (\frac{M_c}{T_c} - I_T)h. \tag{4.13}$$

4.2 Results

To investigate the effect radioactive decay has on these energy and entropy terms through geologic time, we used the parameterizations described in Chapter 3 to place bounds on the heat production per unit mass of the core, h. To start, we will look at the most extreme case. In Chapter 3.3.3, we see that core formation at a single pressure of 58 GPa and 4200 K with an extreme 8 wt% S in the metal at a constant IW-2 put 14.5 ppb U, 9.25 ppb Th, and 0.89 ppm K, which amounts to 7.2 TW of heat at 4.5 Ga. Since we only have constraints on the state of the core currently, we choose to run the energy budget model backward in time. So, our starting concentrations for each isotope are a result of the radioactive decay of the above concentrations: 5.47 ppb ^{238}U, 0.042 ppb ^{235}U, 7.40 ppb ^{232}Th, and 0.1098 ppb ^{40}K. With these abundances, the current per mass heat production (h) is $7.4 * 10^{-25}$ TW/kg, amounting to a Q_R of 1.42 TW, and the equivalent values at 4.5 Ga are $3.3 * 10^{-24}$ TW/kg and 6.4 TW, respectively. The rest of the energy sources and sinks in the model are as described by Nimmo (2015) for a constant E_Φ of 100 MW/K prior to inner core formation and a current heat flux across the core mantle boundary (Q_{CMB}) of 18.2 TW. For reference, the Mathematica code for this model is available in Appendix C.

Figure 4.2 shows the results of our core energy budget model with and without radioac-

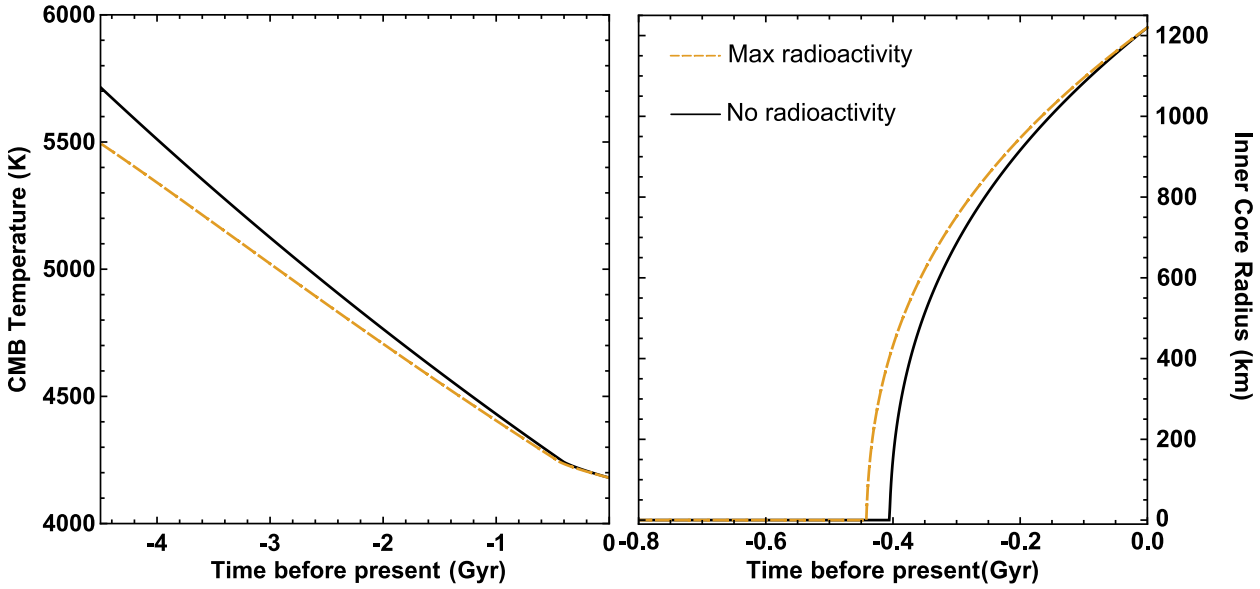

Figure 4.2: **Left** The CMB temperature over the last 4.5 Gyr with and without a radioactive heat source in the core. **Right** As left for inner core radius.

tivity. With no radioactive heat production, the inferred initial temperature at the CMB is 5714 K and the age of the inner core is 0.4 Gyr. Including a maximum radiogenic heat production, as described above, lowers the inferred initial temperature to 5494 K and the inner core age extends to 0.443 Gyr. This change in temperature is within the uncertainty of the current day CMB temperature (±500 K) and is likely not sufficient to curb lower mantle melting through geologic time. One thing to note is that both the planetary growth models described here (i.e. core–mantle differentiation at a single P-T point vs. a range of P-T conditions as the planet grows) are meant to represent average conditions under the stochastic process of planetary accretion. They do not allow for a single large-scale event, such as the moon-forming impact, which would have likely raised the temperature of this process by several thousand degrees (Canup et al., 2015) and may have changed metal–silicate interactions entirely, as has recently been suggested by Lock and Stewart (2017). The aftermath of these extreme events may result in even more U entering the core, which would have a more significant effect on the inferred initial CMB temperature from our model.

Additionally, experiments at extreme temperature conditions have suggested that much more abundant lithophile elements, such as Mg, could enter the Earth's core and provide

a significant amount of buoyant energy release when it subsequently precipitates out of the liquid metal as the core cools (Badro et al., 2016; O'Rourke and Stevenson, 2016; O'Rourke et al., 2017). This may also be true for Si, which may become oversaturated within the core as it cools (Hirose et al., 2017). Since this possibility has only recently become apparent, early models did not include this heat source. The energy production term associated with precipitation, Q_P, is very similar to Q_G, which describes the gravitational potential energy associated with the exclusion of light elements from the inner core as it grows. The major difference between these two terms is that Q_P is active at the CMB and is dependent on the rate of precipitation, which is determined by the pressure and temperature dependence of Mg solubility, whereas Q_G is dependent upon the rate of inner core growth. As such, Q_P would be active much earlier in Earth's history, and depending upon the rate of precipitation, may have been more efficient than inner core growth because the density contrast between metal and oxides/silicates is much greater than the density contrast between solid and liquid metal at the inner core boundary. Furthermore, examination of the P-T dependence of metal–silicate partitioning of both Mg (Eq. 3.9) and Si (Fischer et al., 2015) shows that both elements are more likely to exist in the metal at higher temperatures (with a slight positive dependence on pressure for Mg). Thus, precipitation of these elements as oxides or silicates will occur at the lowest possible P-T condition, which is at the CMB.

Badro et al. (2016) demonstrate that Mg could have reached concentrations above the saturation limit (a current 1.1 wt% in their model) if the last 1-20% of core formation occurred at very high temperatures, such as after the moon-forming impact. Our results of metal–silicate partitioning for Mg show a slightly different picture. First, our data exhibit systematically lower K_D^{Mg} values than those from Badro et al. (2016) (Fig. 3.9). Second, when parameterizing the metal–silicate partitioning behavior of our data alone, in addition to the temperature dependence we were able to extract a dependence of partitioning on pressure and MgO content of the silicate melt, which the previous study did not capture. Using our parameterization, we find that a maximum of 0.31 wt% Mg would have partitioned

into the core at mid-mantle conditions, which is not enough Mg to saturate the metal at CMB conditions according to the model of Badro et al. (2016). Furthermore, using our parameterization (assuming the exchange of Mg with Fe between liquid metal and liquid silicate is representative of the CMB region), the current saturation limit of Mg at the CMB (137 GPa, 4200 K) is 3.2 wt%, several times that of Badro et al. (2016), and would have been higher earlier in Earth's history when the temperature in that region was higher. However, we recognize that we have not employed core-formation models with very high temperature steps, and that our metal–silicate parameterization may indeed reproduce the results of the previous study under very extreme conditions of core formation. The precipitation of Si-bearing materials was also not taken into account in either this work or that of Badro et al. (2016), but that may play an even more significant role. In the future, more work on understanding not only the metal–silicate partitioning, but also the solubility of lithophile elements in metallic liquids and their precipitation rates will need to be constrained for this term to be properly included in energy budget models for Earth's core.

An interesting result of this core energy budget model is that without a strong radiogenic heat source in the core, early widespread lower mantle melting, along with the strong incompatibility of radioactive elements in mantle minerals, would likely concentrate large amounts of radioactive elements at the CMB. A concentrated heat source in this region would significantly affect the heat budget of the core and mantle by lowering the heat flux out of the core, but would probably not directly assist in driving the magnetic field (Nimmo, 2015). Additionally, metal and silicate equilibration at these very high temperatures in the lowermost mantle would further promote addition of U to the core; the implication of not having a radiogenic heat source in the core is that the resultant high temperatures would cause a greater amount of radiogenic heat producing elements to enter the core. Further, this model doesn't allow for lateral variations in heat flow (i.e. it's spherically symmetric). However, tomographic observations of thermochemical piles at the CMB (Garnero et al., 2007) demonstrate distinct lateral heterogeneities at the CMB. It has been suggested that

these regions are warmer than the surrounding mantle (implying increased concentrations of radioactive elements) (Burke and Torsvik, 2004; Torsvik et al., 2010), which would laterally disrupt heat flow out of the core (Amit and Olson, 2015). In the future, this model will need to be coupled to the mantle and possible lateral variations in heat flow accounted for. Finally, a consequence of assuming the core is fully adiabatic is that it precludes the existence of stably stratified layers within the core. Stable stratification could be inferred in the core if, for example, light elements buoyantly accumulate at the CMB. Several authors have argued for such a layer on the basis of seismology (e.g. Helffrich and Kaneshima (2010)), so this too should be included as a possibility in future energy budget models as well.

4.3 Conclusions

We use our metal–silicate partitioning parameterization for the long-lived radioactive elements U, Th, and K to constrain the radiogenic terms of the energy and entropy budget of Earth's core. We find that even if the core is formed under high P-T conditions on average with an extreme upper bound of S content, the resulting radiogenic heat lowers the inferred initial CMB temperature by about 200 K, and extends the inner core age by $\sim$45 million years. While this is a significant difference, it is smaller than the uncertainties on the current CMB temperature and likely not enough to curb widespread melting in the lowermost mantle throughout much of Earth's history. However, melting in the lowermost mantle, known as a basal magma ocean, would likely promote additional partitioning of radiogenic elements into the core. Lateral heterogeneities of radiogenic heat distribution in thermochemical piles on the CMB may also play a role in the core's energy budget, but more work needs to be accomplished before this is well understood. Finally, we investigate the likelihood that Mg-bearing mineral precipitation is an important heat source for the core. Assuming our metal–silicate parameterization is representative of the exchange of Mg from the liquid metal to either solid or liquid silicate at the CMB, we find the equilibrium saturation concentration of Mg at current CMB conditions to be 3.2 wt% and this value would have been higher

in the past when the temperatures of that region were higher. In contrast, we find that a maximum of 0.3 wt% Mg will partition into the metal at nominal core-forming conditions of metal–silicate equilibrium. Thus, it is unlikely that Mg precipitation occurs to a great degree. Models that include a period of very high temperature partitioning, such as after a large impact, may produce slightly different results, and more work on this topic needs to be done to fully understand the core's energy balance both now and in the distant past.

CHAPTER 5

EQUATIONS OF STATE AND PHASE CHEMISTRY OF UO_2 AND THO_2 AT HIGH PRESSURE AND TEMPERATURE CONDITIONS

This chapter is based on: Chidester, B.A., Pardo, O.S., Fischer, R.A., Thompson, E.C., Heinz, D.L., Prescher, C., Prakapenka, V.B., and Campbell, A.J. (submitted) High-pressure phase behavior and equations of state of ThO_2 polymorphs. *American Mineralogist.* and Chidester, B.A., Fischer, R.A., Thompson, E.C., Heinz, D.L., Prescher, C., Prakapenka, V.B., and Campbell, A.J. (in prep) High-pressure, high-temperature phase behavior and equations of state of UO_2.

5.1 Introduction

Actinides, specifically U and Th, are important in the Earth as long-lived radioactive heat-producing elements. Assuming the refractory lithophile element budget of the bulk silicate Earth is chondritic in composition, these elements alone produce up to 36% of the total heat fluxed out of the planet's surface, but their distribution and role within the dynamics of the deepest part of Earth's mantle is unknown (McDonough and Sun, 1995). These elements are also highly refractory and nominally incompatible in major mantle minerals, which makes them excellent tracers for chemical reservoirs in the deep Earth as well as within other planetary bodies (e.g Arevalo et al. (2009); Fonseca et al. (2014)). Additionally, U and Th and their oxides are increasingly important as energy sources for our growing population and

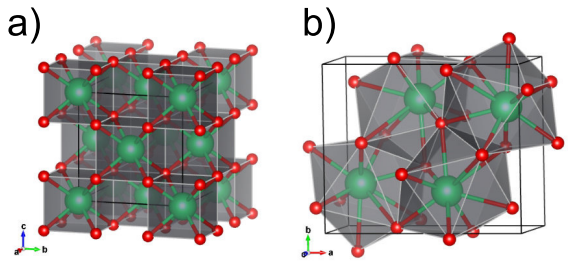

Figure 5.1: a) The fluorite crystal structure. b) The cotunnite-type crystal structure. Green spheres represent the Th^{4+} cations, red spheres represent the O^{2-} anions.

they are used in thermally resistant ceramics (Cuney, 2013). However, stable materials are needed to contain the resulting waste from this industrial usage. Minerals that are stable at extreme conditions can point to analogous materials at ambient conditions. Thus, exploring the mineralogy of actinide-bearing minerals at the extreme conditions is universally important.

End-member ThO_2 (thorianite) takes the cubic fluorite-type (CaF_2, $Fm3m$) structure at ambient conditions (Fig. 5.1a). In nature, this material forms a solid solution with end-member UO_2 (uraninite), which is also in the fluorite structure. Room temperature X-ray diffraction (XRD) studies show that at upon compression, both ThO_2 and UO_2 undergo a reconstructive phase transition to the orthorhombic cotunnite-type structure (α-$PbCl_2$, $Pnma$) (Fig. 5.1b) (Benedict et al., 1982; Dancausse et al., 1990; Idiri et al., 2004; Olsen et al., 2004), resulting in an increase in coordination of the cation from 8 to 9. At room temperature, this phase transition is kinetically inhibited, with the high-pressure phase first appearing between 30-40 GPa for both ThO_2 and UO_2 and coexisting with the metastable low-pressure phase until 55-57 GPa (ThO_2) or >69 GPa (UO_2). Because of this sluggishness, the precise position of the equilibrium phase boundary is not well constrained.

The thermoelastic parameters (e.g. bulk modulus, K, and thermal expansion, α) of these materials are necessary for modeling their thermodynamic behavior at extreme conditions of pressure and temperature, such as within the deep Earth or in a nuclear reactor. Recent measurements (XRD, ultrasonic) and calculations of the ambient-pressure isothermal bulk modulus (K_0) of pure thorianite at 300 K are consistent around 185-198 GPa with a pressure derivative ($dK/dP = K_0'$, where relevant) of ∼5 (Macedo et al., 1964; Idiri et al., 2004; Olsen et al., 2004; Kanchana et al., 2006; Shein et al., 2007; Boettger, 2009; Wang et al., 2010; Boudjemline et al., 2011; Li et al., 2014). Earlier XRD studies resulted in much higher values of K_0 and K_0' - 262 GPa and 6.7, respectively (Dancausse et al., 1990), while an inelastic X-ray scattering experiment and a different series of calculations predicted K_0 values around 220 GPa (Clausen et al., 1987; Li et al., 2002; Olsen et al., 2004; Kanchana et al., 2006;

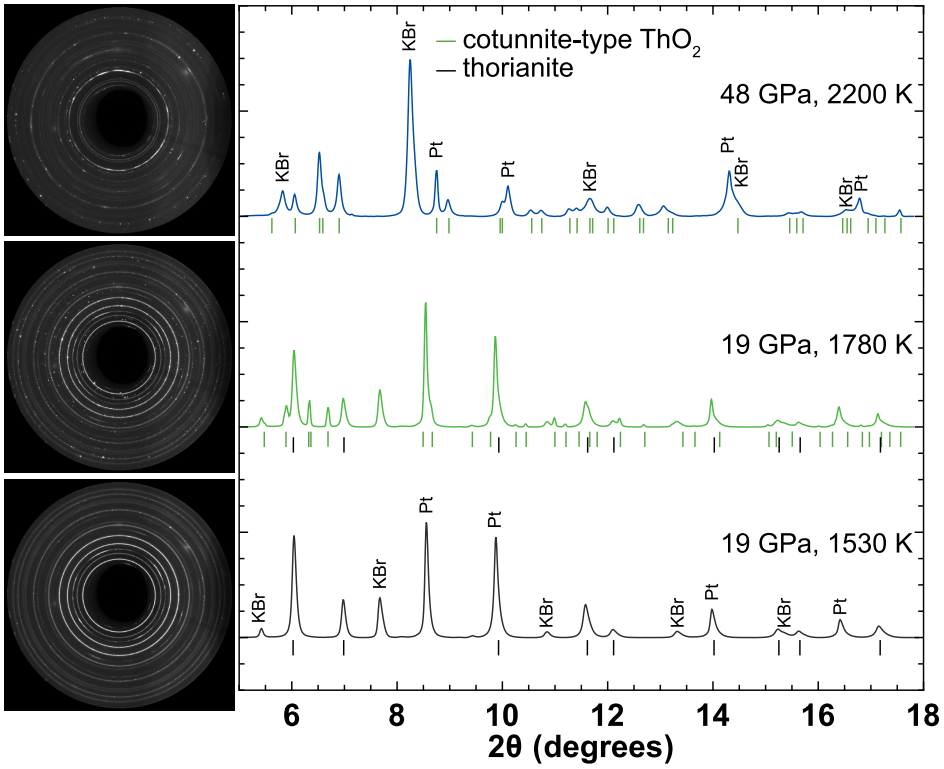

Figure 5.2: Raw diffraction images and integrated diffraction patterns for three *in situ* XRD measurements of sample B25.

Sevik and Çaln, 2009). The two experimental XRD studies of uraninite resulted in K_0 values of 192 and 207 GPa, with K_0' values of 9 and 4.5, respectively (Benedict et al., 1982; Idiri et al., 2004). Calculations of the bulk modulus of this material are consistent with experiments, ranging from 177-222 GPa, although in general the pressure derivatives are lower (Perry et al., 2017; Wang et al., 2013; Li et al., 2002; Geng et al., 2007). These results are summarized in Tables 5.1 and 5.4 along with calculated values for the high-pressure phases. To date, no experimental studies have reported on the behavior of these materials at simultaneous high pressures and high temperatures or on the equations of state of the high-pressure cotunnite-type phases. In this study, we conducted *in situ* XRD measurements of ThO_2 to 60 GPa and 2500 K and UO_2 to 95 GPa and 2600 K to more precisely define the phase boundary and to measure the thermal equation of state parameters for both the low- and high-pressure phases of these materials.

5.2 Results: Phase diagram of ThO_2

The measured lattice parameters and pressure-volume-temperature (P-V-T) data points from the *in situ* XRD experiments are listed in Tables S5.1 (thorianite) and S5.2 (cotunnite-type ThO_2) of the Supplemental Material. Ambient pressure XRD measurement of the ThO_2 starting material indicated that it was in the fluorite-type structure (Fig. 5.1a) and had a lattice parameter of a = 5.5958 ± 0.0005 Å (V_0 = 26.379 ± 0.007 cm^3/mole), which is in line with literature values for end-member thorianite (Table 5.1). Synchrotron XRD measurements at high pressure and room temperature demonstrate that thorianite exists in this fluorite-type structure until ~34 GPa, at which point new peaks appear between the (111) and (200) fluorite peaks, revealing the presence of the cotunnite-type phase (Fig. 5.1b). Figure 5.2 shows high-temperature examples of raw diffraction images and their corresponding integrated spectra (intensity vs. 2θ) for this phase transition, as well as a higher P-T pattern containing only the cotunnite-type phase.

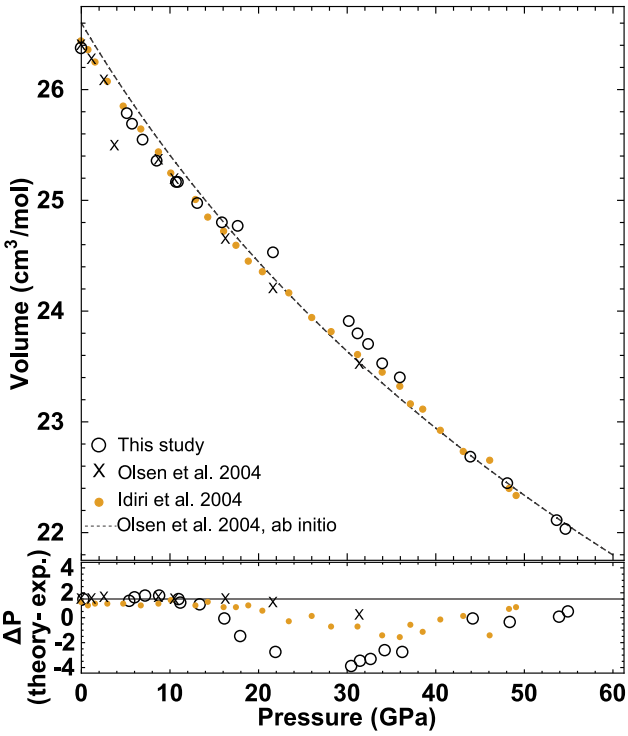

Figure 5.3: Room temperature P-V data for thorianite from this study and the available literature. The ab initio curve from Olsen et al. (2004) was developed using the General Gradient Approximation. The difference between the pressures predicted from calculations and the measured pressure is shown in the bottom panel. The solid line corresponds to the difference in ambient pressure volumes (predicted-measured). A discontinuity is apparent in the data beginning around 15 GPa.

The fluorite–cotunnite phase transition requires a crystallographic reconstruction, so it is characterized by a large degree of kinetic inhibition. As with previous XRD measurements at room temperature, the fluorite-type phase of ThO_2 was present up to the highest pressures

Table 5.1: Measured and calculated equation of state parameters for ThO_2.

Thorianite					
V_0 (cm^3/mole)	K_0 (GPa)	K_0'	αK_T (GPa/K)	Ref.	Method
26.379(7)	204(2)	**4**	0.0035(3)	This Study	LH-DAC
26.44	198(2)	4.6(3)		Idiri et al. (2004)	RT-DAC
26.37	262(4)	6.7(5)		Dancausse et al. (1990)	RT-DAC
26.39	195(2)	5.4(2)		Olsen et al. (2004)	RT-DAC
25.36	225	4.2		Olsen et al. (2004)	FP-LMTO-LDA
26.60	198	4.2		Olsen et al. (2004)	FP-LMTO-GGA
26.68	189	4.1		Perry et al. (2017)	GGA-PAW
26.8	191	4.5		Wang et al. (2010)	GGA-PAW
26.33	187.6	4.19		Li et al. (2014)	GGA-PBE
26.77	184.5	4.49		Boettger (2009)	GGA-LCGTO-FF
25.32	225	4.4		Kanchana et al. (2006)	FP-LMTO-LDA
26.58	198	4.5		Kanchana et al. (2006)	FP-LMTO-GGA
26.16	198	4.91		Boudjemline et al. (2011)	GGA
25.53	290			Kelly and Brooks (1987)	LMTO-ASA
26.76	192.8			Shein et al. (2007)	FLAPW
26.44	216			Sevik and Çaln (2009)	LDA+U
	175			Harding et al. (1994)	Dirac-Fock approx.
	221			Li et al. (2002)	FP-LMTO-GGA
	223			Clausen et al. (1987)	INS
	193(2)			Macedo et al. (1964)	Ultrasound
Cotunnite-type ThO_2					
24.75(6)	190(3)	**4**	0.0037(4)	This Study	LH-DAC
25.07	177	4.2		Perry et al. (2017)	GGA-PAW
25.1	148	7.8		Wang et al. (2010)	GGA-PAW
24.1	202.1	4.22		Li et al. (2014)	GGA-PBE
24.7	206.8	4.94		Boettger (2009)	GGA-LCGTO-FF
24.55	163.2	6.19		Boudjemline et al. (2011)	GGA

Bold values were held fixed in the fitting procedure. LH = laser-heated; RT = room temperature; FP = full potential; PAW = projector-augmented wave method; PBE = Perdew-Burke-Ernzerhof functional; LCGTO-FF = linear combinations of Gaussian type orbitals-fitting function; LMTO = linear muffin-tin orbital method; LDA = local density approximation; GGA = general gradient approximation; ASA = atomic-sphere approximation; INS = inelastic neutron scattering. This table was adapted from Olsen et al. (2004).

achieved at room temperature in this study, ∼54 GPa (Dancausse et al., 1990; Idiri et al., 2004; Olsen et al., 2004). This kinetic barrier was also observed in other room temperature compression studies using different techniques. With Raman spectroscopy, Jayaraman et al. (1988) observed the initiation of the phase transition between 30 and 37 GPa, but did not reach high enough pressures to observe the disappearance of the fluorite-type phase. The slight differences in the observed transition pressure range in these studies are likely due to the use of different pressure-transmitting media. Less hydrostatic conditions, such as were used in previous studies, promote higher strain, and therefore result in more abrupt phase transitions than more hydrostatic conditions in the experiments described here.

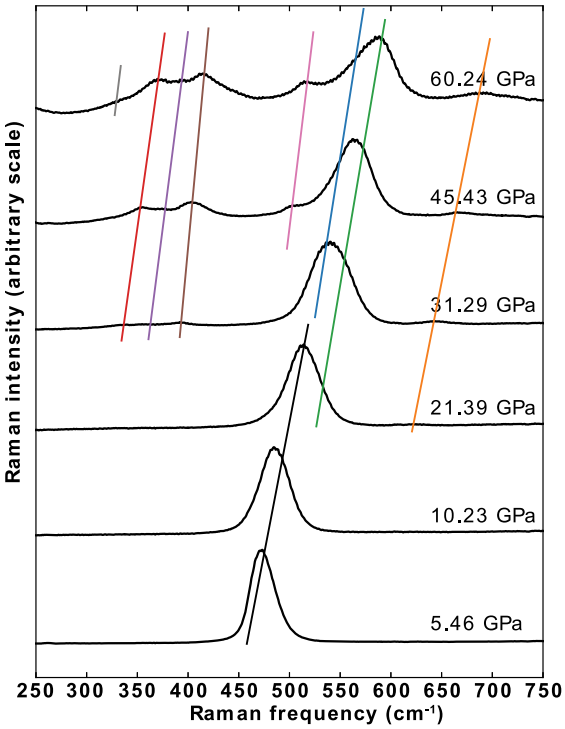

Figure 5.4: Raman spectra of ThO_2 collected at room temperature on increasing pressure. Lines are meant to indicate how peaks were tracked as a function of pressure. Colors are coordinated with absorption frequencies in Fig. 5.5

When plotting the room temperature volume vs. pressure XRD data from this study along with the room temperature data readily available in the literature, as in Fig. 5.3, a discontinuity in compression behavior is observed around 15-20 GPa. Although the crystal structure remains in the fluorite-type phase, the volume is greater at these pressures than expected by normal compressibility. We interpret this abrupt lowering of the density under pressure as anion sub-lattice disorder, as was described for the fluorite–cotunnite-type phase transition in CaF_2 (Boulfelfel et al., 2006). In this model, the anions are subject to local disordering, described by the authors as "melting". This effectively increases the volume, which allows the cations to rearrange. Thus, this property is likely a hallmark of the onset of the fluorite–cotunnite phase transition. Our data show this discontinuity much more intensely than the literature

data, which again is likely due to the difference in hydrostatic environments.

To further investigate this phase transition process, we performed Raman spectroscopy at room temperature under non-hydrostatic conditions. As described in the Chapter 2.3, measurements were made both on increasing and decreasing pressure. Examples of the compression spectra are shown in Fig. 5.4. Under these conditions at ~5 GPa, thorianite exhibits a single Raman absorption mode at ~474 cm^{-1}. This peak broadens and shifts to higher wavelengths with increasing pressure throughout the compression measurements. At ~22 GPa, new peaks appear at 540 and 622 cm^{-1}. Above 32 GPa, a triplet of absorption modes become apparent at low wavenumbers, 330-390 cm^{-1}, and a single peak becomes resolvable at 495 cm^{-1}. The pressure dependence of these absorption frequencies is shown in Fig. 5.5. We interpret the additional peaks appearing in the 20-30 GPa range as signaling the rearrangement of the anion sublattice, whereas the peaks appearing at 32 GPa are the final stages of the phase transition. There is a regular linear slope for the vibrational modes as a function of pressure above 37 GPa, thus the full crystallographic reconstruction of the cubic fluorite-type structure to the orthorhombic cotunnite-type structure appears to be complete for both the anions and cations between 32 and 37 GPa, which is consistent with the XRD data. Given the change in slope, none of the high-pressure modes appear to be directly related to the low-pressure phase. One final peak at ~330 cm^{-1} is resolved above 50 GPa

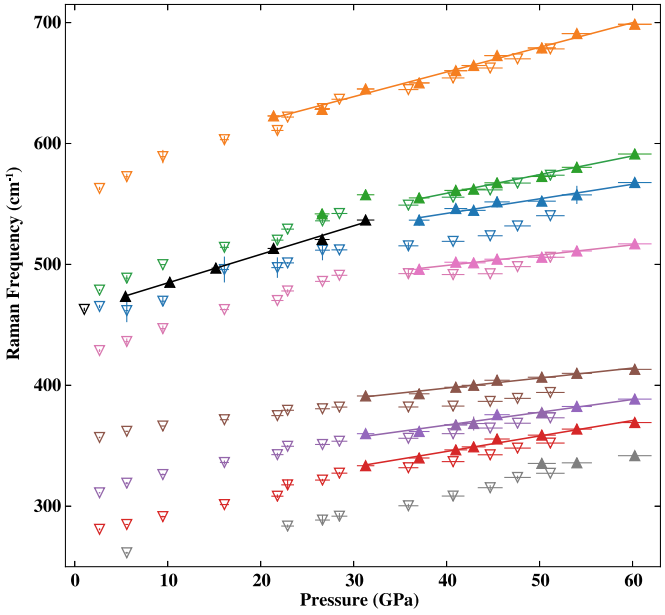

Figure 5.5: Raman vibrational frequencies as a function of pressure. Thorianite exhibits a single vibrational mode (black triangles), whereas 8 separate peaks were identified for the cotunnite-type phase. Upward triangles were measured on increasing pressure, downward triangles are decreasing pressure. Pressure dependencies were fit to linear trends, which are shown in their corresponding color.

(Figs. 5.4 and 5.5). Upon decompression, the cotunnite-type absorption peaks remain until ∼2 GPa while continually decreasing in Raman frequency. At 1 GPa, there is only a single peak remaining, suggesting that it has fully reverted back to the fluorite-type structure.

At high temperatures, the thorianite–cotunnite-type phase transition also occurs. At ∼17 GPa, the transition was observed on increasing temperature between 1534 ± 114 K and 1583 ± 119 K. Again, there is some sluggishness to this transition, even at high temperatures. The high-pressure phase was not observed at all in the pressure step at 18-19 GPa, which suggests that in this case heating was faster than the phase transition was allowed to proceed. Additionally, from 20-30 GPa at high temperatures both phases are observed, where only one of them (likely the cotunnite-type phase) can be thermodynamically stable. Above 30 GPa at high temperatures, only the cotunnite-type phase is observed up to the highest pressures reached in this study, 62 GPa. This information was compiled as our preferred P-T phase diagram for this material in Fig. 5.6. Based on our observations, the phase boundary is likely very close to vertical or slightly negative around 20-30 GPa in P-T space.

5.3 Results: Equations of state of ThO_2 polymorphs

Given the range of P-V-T data obtained for the polymorphs of ThO_2 in this study, we were able to extract equation of state parameters for each phase. We fit both sets of data to the Mie-Grüneisen type equation of state (Eq. 5.1), where the reference pressure (300 K) equation took the Birch-Murnaghan form (Eq. 5.2).

$$P = P_{300K} + P_{thermal} \tag{5.1}$$

$$P_{300K} = 3K_0 f(1+2f)^{\frac{5}{2}}(1+\frac{3}{2}f(K_0' - 4)) \tag{5.2}$$

Here, f is the finite Eularian strain, $\frac{1}{2}((\frac{V}{V_0})^{\frac{-2}{3}} - 1)$, V is the measured volume of the material at pressure, P, V_0 is the ambient pressure volume, K_0 is the ambient pressure isothermal

bulk modulus, and K_0' is its pressure derivative. For the thorianite equation of state, we only used the room temperature data prior to the volume discontinuity, that is, below ~15 GPa. For the cotunnite-type phase, there were no room temperature patterns of high enough quality that lattice parameters could be extracted. Thus, no room temperature data were used in the fits for the high-pressure phase. Because of the limited room temperature data, we chose to define the thermal pressure as in equation 5.3.

$$P_{thermal} = \alpha K_T (T - 300) \tag{5.3}$$

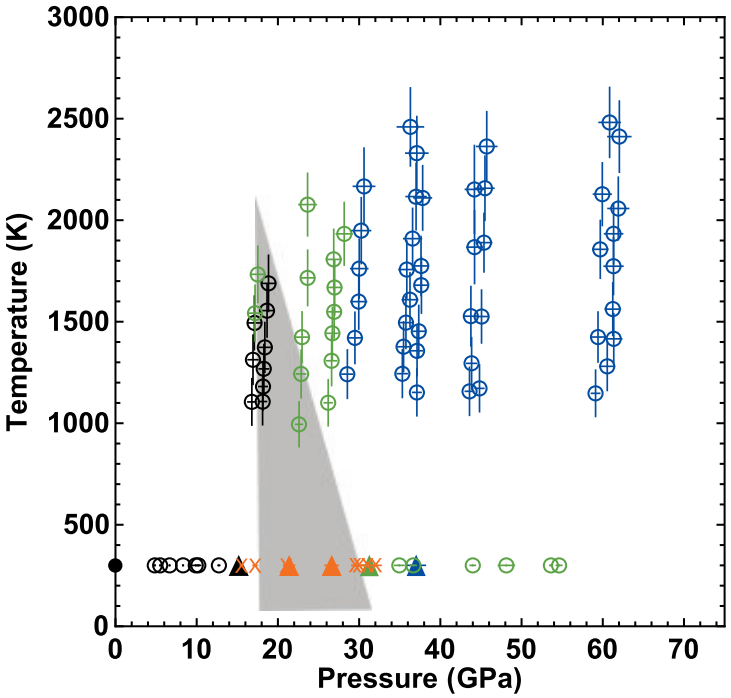

Figure 5.6: Phase diagram for ThO_2. Circles indicate *in situ* XRD measurements. Black: thorianite; green: mixed phase; blue: cotunnite-type ThO_2. Orange X's: low density thorianite determined from Fig. 5.3 (indicates anion sublattice disorder). Triangles indicate relevant Raman measurements. Black: last spectrum with only thorianite; orange: some new vibrational modes observed; green: all high-P modes are present; blue: phase transformation appears complete. The grey shaded region indicates our preferred phase boundary. See text for discussion.

In this case, the coefficient on temperature is a constant. α is thermal expansion and K_T is the bulk modulus at temperature, T. The equation of state parameters for each phase are given in Table 5.1, along with the available literature values. For thorianite, V_0 was measured prior to the compression experiments to be 26.379(7) cm^3/mole, so it was fixed in the fitting routine. Additionally, K_0' was fixed to a value of 4 to allow for more precise determination of the thermal term. Our choice of 4 for K_0' is slightly lower than has previously been measured (~5), so our bulk modulus is slightly higher than other recent XRD studies (~195-198) at 204 GPa (Idiri et al., 2004; Olsen et al., 2004).

We feel that although previous studies infer a higher value for K_0', those studies included data beyond the onset of anion sub-lattice rearrangement, which would result in a pressure derivative that is artificially high, justifying our choice of 4 for this value. The thermal pressure coefficient for thorianite was determined to be 0.0035(3) GPa/K.

The properties of the high-pressure cotunnite-type phase of ThO_2 are very similar to those of the low-pressure phase. Holding K_0' at a value of 4, the bulk modulus for this phase was determined to be 190(3) GPa. This is slightly more compressible, but very similar to the value for thorianite. Additionally, the thermal pressure coefficient was found to be 0.0037(4) GPa/K, suggesting that the high-pressure phase reacts very similarly to pressure and temperature as the low-pressure phase. The fitted zero-pressure volume for the cotunnite-type phase is 24.75(6) cm^3/mole, which is 6.2% more dense than thorianite at ambient conditions. This is virtually the same volume contrast that was observed at 35 GPa, by Idiri et al. (2004). The compiled P-V-T data from this study are plotted in Fig. 5.7 along with calculated isotherms for comparison. The values for the individual lattice parameters of the cotunnite-type phase are given in the top panel of Fig. 5.8. Each one decreases with pressure, as expected, but the a-axis appears to be compressing at a faster rate than either

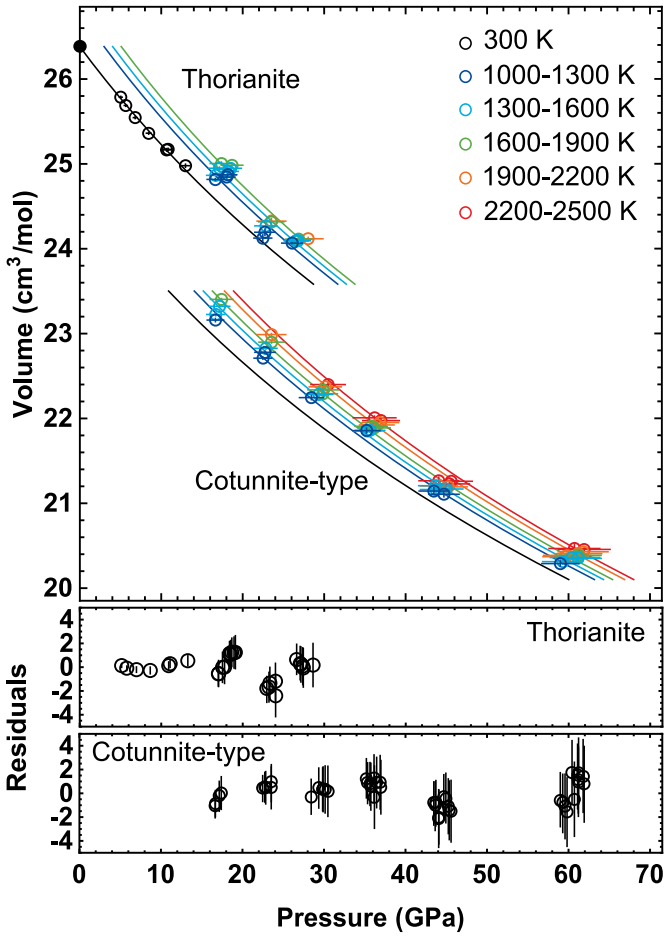

Figure 5.7: Measured P-V-T data for thorianite and cotunnite-type ThO_2. Curves are isotherms calculated using the equation of state parameters from Table 5.1. Isotherms are color-coded by temperature. Residuals to the fits are provided in the bottom panels.

b or c, while the short b-axis changes very little. This relationship is best demonstrated in the lattice parameter ratios as a function of pressure in the lower panels of Fig. 5.8.

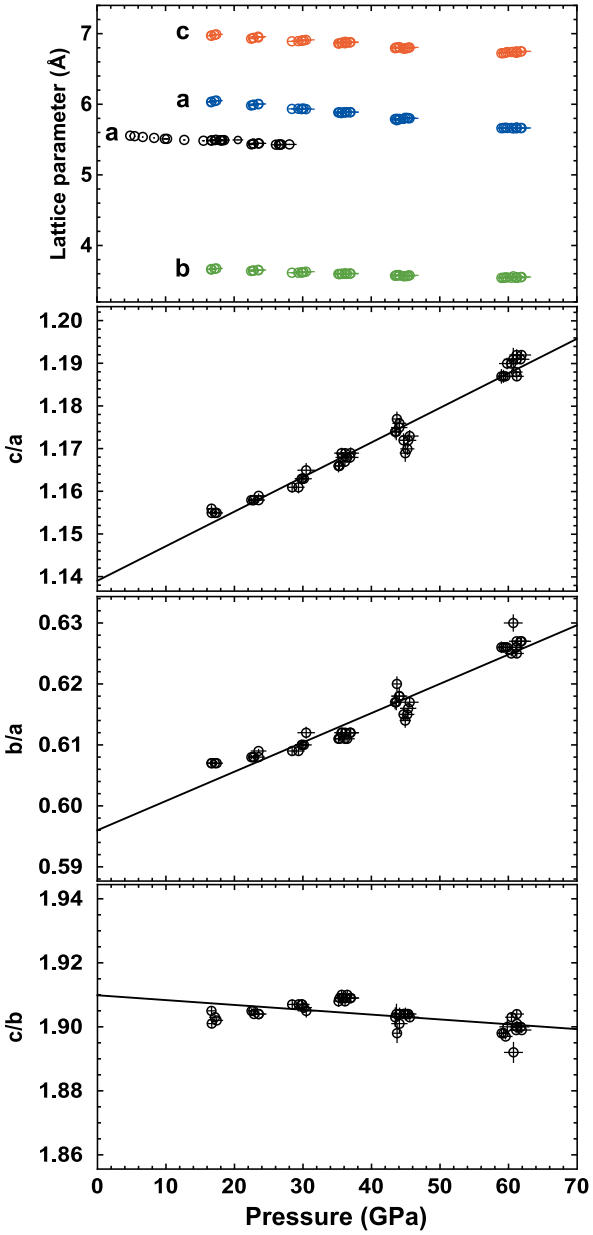

Figure 5.8: Individual lattice parameters and their ratios for cotunnite-type ThO_2. Black lines are linear fits to the data.

In general, the ratios of the lattice parameters change linearly with pressure, with only small dependences on temperature. This would occur if the coordination polyhedra within the cotunnite-type structure are continuously distorting with pressure, and suggests that upon increasing compression the material will undergo another structural phase transition. Some likely options for this higher pressure phase are common post-cotunnite structures, such as the hexagonal Ni_2In structure ($P6_3/mmc$) or orthorhombic distortions thereof (Song et al., 2012). For convenience, the ratios have been fitted to a linear dependence of pressure. The slopes and hypothetical zero-pressure values from these fits are given in Table 5.2.

5.4 Results: Phase diagram of UO_2

The measured lattice parameters and pressure-volume-temperature (P-V-T) data points from the *in situ* XRD experiments on UO_2 are listed in Tables S5.3 (uraninite), S5.4 (tetragonal UO_2), and S5.5 (cotunnite-type UO_2) of the Supplemental Material. Ambient pressure

measurement of our UO_2 sample material confirmed that it was in the fluorite-type structure (Fig. 5.1a) with an initial lattice parameter of $a = 5.46240 \pm 0.00004$ Å ($V_0 = 24.538 \pm 0.001$). This is similar to literature values (Table 5.4) and confirms that the stoichiometry of our starting material is very close to $UO_{2.00}$ (Benedict et al., 1982; Idiri et al., 2004; Leinders et al., 2015). The high-pressure, room-temperature experiments in this study did not reach high enough pressure to observe the onset of the transition to the cotunnite-type phase (Fig. 5.1b), which has been previously observed above 29 GPa. However, uraninite did exhibit abnormal compressional behavior above ∼10 GPa and up to 20 GPa, as was observed for thorianite. As in that case, it is possible that this phenomenon marks the beginning of the fluorite-type to cotunnite-type phase transition. A discontinuity in compression behavior of this type has also been observed in uraninite in the literature (Idiri et al., 2004).

Examples of the high-pressure, high-temperature XRD patterns are plotted in Fig. 5.9 and our preferred phase diagram for this material is presented in Fig. 5.10. As with ThO_2, UO_2 exhibits a large amount of kinetic inhibition across the phase transitions, and several phases were often observed at a single P-T point as is demonstrated in Fig. 5.9. The uraninite–cotunnite-type phase transition was observed around 27 GPa at high temperatures (Fig. 5.10). Fig. 5.9a shows an example of the presence of cotunnite-type UO_2 around 23 GPa, although based on relative peak intensities and their temperature dependence, uraninite was determined to be the stable phase at this condition. Uraninite coexisted with the cotunnite-type phase at high temperatures up to ∼40 GPa. Above 35 GPa upon initiation of laser heating, a new phase of UO_2 was detected (Fig. 5.9c). This phase was indexed to a tetragonal crystal structure, likely in the $I4/mmm$ space group, although we cannot rule out several lower-symmetry space groups based on systematic absences alone. Examples of calculated and measured d-

Table 5.2: Linear fits to the lattice parameter ratios as a function of pressure for cotunnite-type ThO_2.

Ratio	**Slope (GPa^{-1})**	**Zero-pressure value**
c/a	0.00081(2)	1.1391(9)
b/a	0.00048(2)	0.5962(8)
c/b	-0.00015(3)	1.910(1)

Table 5.3: Measured and calculated d-spacings of the tetragonal phase in the $I4/mmm$ at 35 GPa and 1200 K.

hkl	d calc. (Å)	d obs. (Å)	δ (obs-calc)
101	3.00846	3.00898	0.00052
110	2.69416	2.69436	0.00020
002	2.45139	2.45039	-0.0010
200	1.90506	1.90528	0.00022
112	1.81316	1.81305	-0.00011
211	1.60950	1.60957	0.00007
202	1.50342	1.50366	0.00024
220	1.34708	1.34712	0.00004

spacings of this new phase in the $I4/mmm$ are given in Table 5.3 for comparison. This phase was often observed to coexist with the cotunnite-type structure at low temperatures (Fig. 5.9c,d), although it was clear based on relative peak intensities as a function of temperature that the tetragonal phase was the thermodynamically stable lower-temperature phase. On increasing temperatures, the tetragonal phase disappeared and the cotunnite-type structure was found to be the stable high-temperature phase at least up to 63 GPa (Fig. 5.9b). The temperature at which this phase transition was occurred increased with pressure, suggesting a positive Clapeyron slope for this phase boundary.

The tetragonal phase has been observed at high temperatures previously, although it was not recognized as such. Greaux et al. (2008) made similar measurements of natural uraninite at high pressures. They chose to thermally anneal their samples at 2000 K prior to each room temperature XRD measurement to ensure high-quality diffraction data. Using this technique, they observed a high-pressure phase that could not be matched to the cotunnite-type structure as was expected. They indexed this phase to an orthorhombic *Pbca* structure. Careful examination of their reported XRD patterns confirms that this phase is equivalent to the phase we observe, although we were able to index this phase to a higher symmetry structure. As this phase has not been observed before at room temperature, it is likely that it requires some heating to overcome the sluggish kinetics to transform from the cotunnite-type structure, which is indeed what Greaux et al. (2008) did by thermally annealing their samples. Furthermore, the natural sample used by Greaux et al. (2008) contained some large cation impurities, such as Pb, which may have stabilized the structure and allowed it to be quenched to room temperature for their measurements.

Table 5.4: Measured and calculated equation of state parameters for UO_2.

Uraninite					
V_0 (cm^3/mole)	K_0 (GPa)	K_0'	αK_T (GPa/K)	Ref.	Method
24.538(1)	175(7)	4.8(5)	0.0044(2)	This Study	LH-DAC
24.66	192(20)	9(4)		Benedict et al. (1982)	RT-DAC
24.68	207(2)	4.5(4)		Idiri et al. (2004)	RT-DAC
25.16(1)	166(7)	4		Greaux et al. (2008)††	RT-DAC
25.18	176.878	3.65021		Perry et al. (2017)	GGA-PAW
24.36	222.4	3.2		Wang et al. (2013)	GGA-LDA+U
	222.7	3.5		Li et al. (2002)	FP-LMTO-GGA
24.29	208.32			Geng et al. (2007)	LSDA+U
Tetragonal UO_2					
23.9(2)	220(20)	**4**	0.0043(7)	This Study	LH-DAC
24.33(7)	225(8)	**4**		Greaux et al. (2008)†	RT-DAC
Cotunnite-type UO_2					
23.02(6)	187(4)	**4**	0.0052(3)	This Study	LH-DAC
23.82	151.381	4.778		Perry et al. (2017)	GGA-PAW
22.81	192.5			Geng et al. (2007)	LSDA + U

Bold values were held fixed in the fitting procedure. ††Values were reported for the low P-T phase in the pyrite-type structure. †Values in this study were reported for a *Pbca* structure, which we believe to be the tetragonal phase (see text). LH = laser-heated; RT = room temperature; FP = full potential; PAW = projector-augmented wave method; LMTO = linear muffin-tin orbital method; L(S)DA = local density approximation; GGA = general gradient approximation.

Along with this new phase, they also observed one to two low-intensity peaks which they could not index. We believe these peaks belong to the cotunnite-type phase, again supporting the slow kinetics of this phase transition even at high temperature. It is worth noting that Greaux et al. (2008) indexed their lower pressure phase to the pyrite type (or modified fluorite) structure (space group $Pa\bar{3}$) rather than the fluorite structure. This may be a consequence of various impurities of the sample or strain resulting from quenching after the thermal annealing process. We did not see any evidence of the pyrite-type structure in our study.

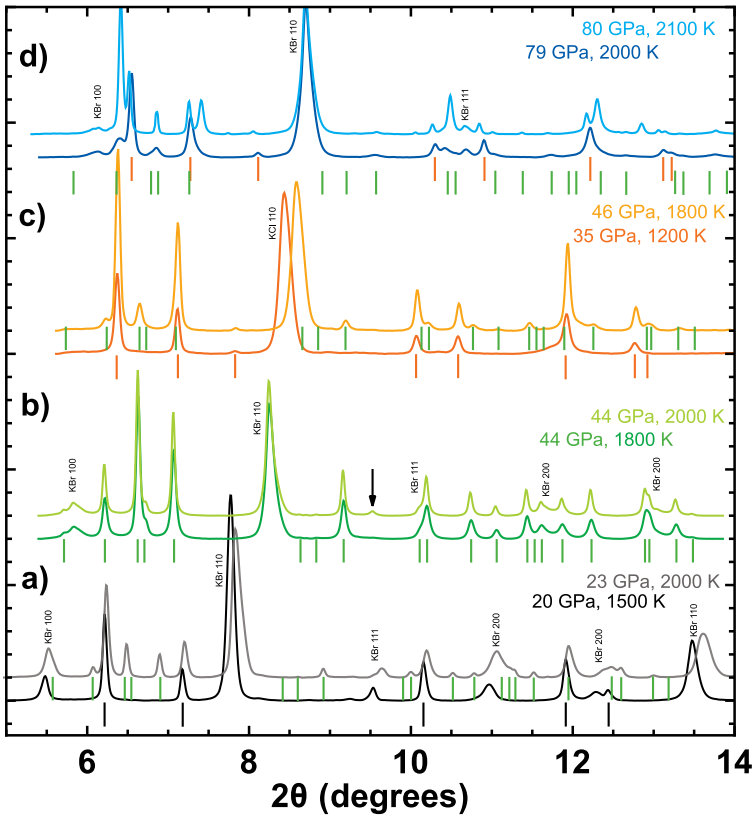

Figure 5.9: Integrated diffraction patterns for *in situ* XRD measurements of sample UO_2 demonstrating all possible combinations of phases. Hash marks indicate: black - uraninite, green - cotunnite-type UO_2, orange - tetragonal UO_2. The P-T conditions of each measurement is noted.

At temperatures above the tetragonal–cotunnite-type phase transition, an additional peak was observed at slightly higher angle (2θ) than the cotunnite (211) peak (noted in Fig. 5.9b by a black arrow). While this peak could not be assigned to the cotunnite-type structure, it was possible to index this peak along with all of the cotunnite-type peaks to a monoclinic structure. However, the volume of this theoretical structure is ~6 % lower than the cotunnite structure at the same conditions, which is too large a difference for this to be a monoclinic distortion of the cotunnite-type structure. The peak grew and changed as a function of temperature, so it may represent a chemical reaction or disproportionation of a small fraction of the sample material at high temperatures.

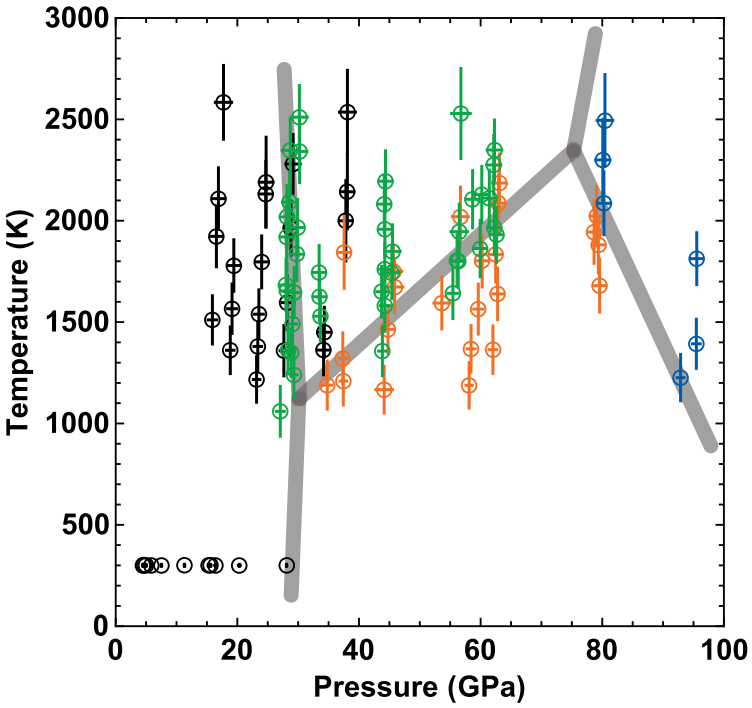

Figure 5.10: Our preferred phase diagram for UO_2. Data point colors indicate the stable phase at each P-T point: black - uraninite, green - cotunnite-type UO_2, orange - tetragonal UO_2, blue - new phase or decomposition of UO_2 (see text). The grey bars indicate approximate phase boundaries.

At 79 GPa, the tetragonal phase is stable (coexisting with the metastable cotunnite-type phase) up to 2000 K, at which point the sample undergoes a striking change (Fig. 5.9d). The raw diffraction images become spotty, suggesting a sudden recrystallization of the sample, and several new diffraction spots emerge. This may be another phase transition or possibly a decomposition of UO_2 into two separate phases. None of the peaks present can be matched to any known phase of U metal at that condition, so if there are two phases, they are likely both oxides. The sample failed to absorb the laser as well after this change occurred, suggesting different optical properties for the new material. A phase transition of this material has been predicted at around these pressures (Perry et al., 2017), and further work at these very high P-T conditions is required to fully understand this process. At 95 GPa and high temperatures, only the unknown phases are present, implying a negative Clapeyron slope for this transition/decomposition process.

5.5 Results: Equations of state of UO_2 polymorphs

Similar to ThO_2 above, the high P-T data of UO_2 were fit to thermal equations of state defined in Eqs. 5.1, 5.2, and 5.3, taking the thermal coefficient, αK_T, as a constant. The fitted coefficients for uraninite, tetragonal UO_2, and cotunnite-type UO_2 are given in

Table 5.4 along with previous experimental and calculated values from the literature. As with ThO_2, we chose not to fit the room temperature measurements of uraninite that did not exhibit normal compression (i.e. above ~10 GPa). The isothermal bulk modulus, K_0, for uraninite was fit to 175(7) GPa, with a pressure derivative (K_0') of 4.8(5). These values are very similar to those reported by Greaux et al. (2008) for the low P-T phase in the modified fluorite, or pyrite-type, structure. Since they used a natural sample with impurities and indexed it to a different structure, we would expect their V_0 to be slightly different than ours, but the compressibility should be quite similar, which is indeed what we see. Benedict et al. (1982) found K_0 and K_0' values of 192(20) GPa and 9(4), respectively, which are the same as our values within error. That study was completed nearly 35 years ago, so the quality of the data are likely much lower. Idiri et al. (2004) found values of 207(2) GPa and 4.5(4), respectively, but as mentioned above, their data show a distinct discontinuity as a function of pressure which they ignored when fitting their equation of state. One recent calculation finds a very

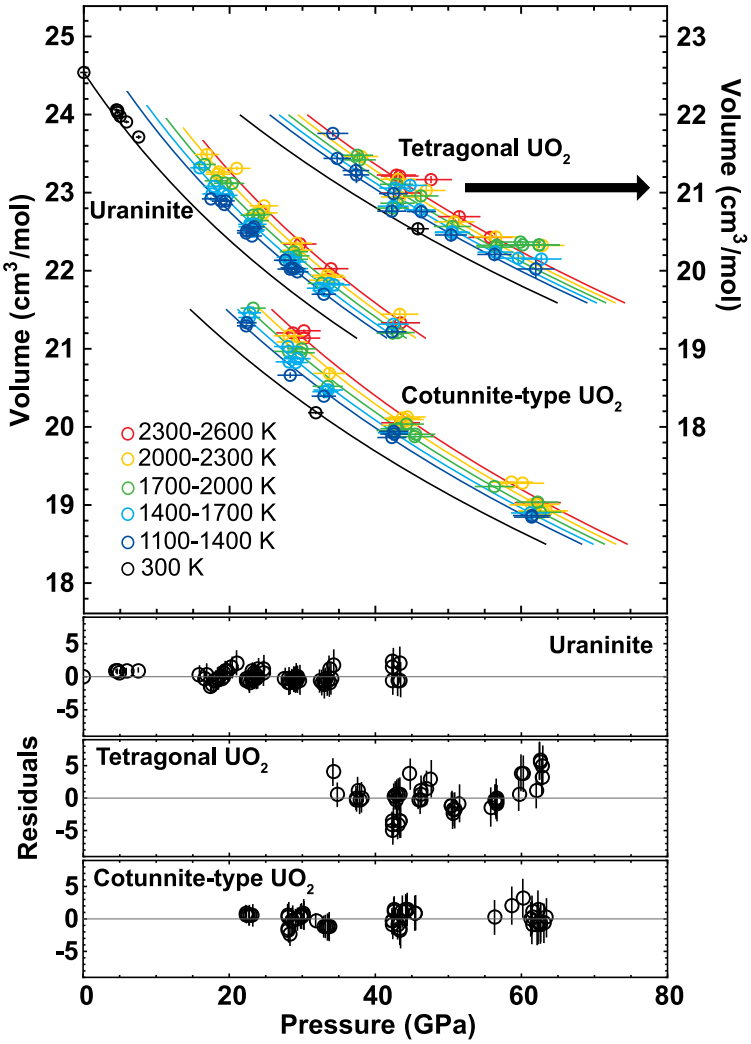

Figure 5.11: Measured P-V-T data for uraninite, tetragonal UO_2 and cotunnite-type UO_2. Curves are isotherms calculated using the equation of state parameters from Table 5.4. Isotherms are color-coded by temperature. Tetragonal volumes correspond to the axis on the right due to significant overlap with the other phases. Residuals to the fits are provided in the bottom panels.

similar value to ours (177 GPa, Perry et al. (2017)), but in general all of the calculated pressure derivatives are low (i.e. < 4) (Wang et al., 2013; Li et al., 2002; Geng et al., 2007). As such, other calculated bulk moduli are higher than our measured value ($\sim$ 220 GPa). We also provide a thermal pressure coefficient, αK_T, for this phase of 0.0044(2) GPa/K. Unfortunately, there are no literature data for us to compare our value with. The success of our thermal equation of state are shown in Fig. 5.11, where measured P-V-T data are plotted with calculated isotherms for each phase in this study.

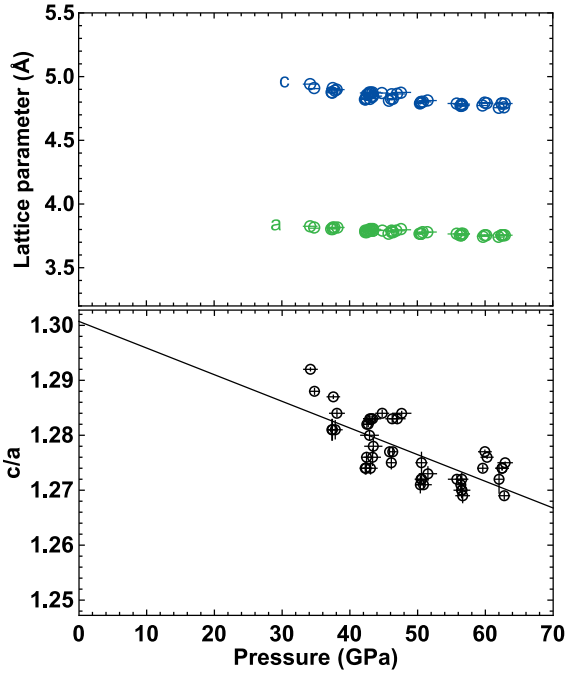

Figure 5.12: Measured lattice parameters **(Top)** and c/a ratio **(Bottom)** for tetragonal UO_2 as a function of pressure. The black curve was fit to the data. The result of that fit is in Table 5.5.

The equation of state parameters for the tetragonal phase of UO_2 are also given in Table 5.4. There is much more scatter in the equation of state fit for this phase than for the other polyphorphs of UO_2, which is a result of the relatively narrow range of P-T space in which this phase is stable. The fitted V_0 and K_0 values are 23.9(2) cm^3/mole and 220(20) GPa, respectively. K_0' was held fixed at a value of 4 for this calculation. The thermal parameter, αK_T, for this phase was 0.0043(7) GPa/K. Our data are consistent with this phase as the high-pressure, low-temperature phase above $\sim$35 GPa. When extrapolating to zero pressure, this phase is only about 3% less dense than uraninite. For this reason, the compression data for this phase had to be offset from the rest of the P-V-T data in Fig. 5.11 to be distinguishable from the other phases. With a significantly higher bulk modulus, this phase is stiffer than either of the other observed phases (Fig. 5.11), but the thermal behavior is very similar. We are only able to compare our equation of state with that of Greaux et al. (2008), as it is the only study to observe this phase. As with the lower-

pressure phase, we would expect the fitted zero-pressure volumes to be slightly different between the two studies owing to differences in composition and the space group assigned to the structure ($I4/mmm$ vs. $Pbca$). However, given that it is likely the same phase, we would expect to see similar compressibilities. This is indeed true, as the previous study measured a K_0 value of 225(8) GPa while holding K_0' fixed at 4. The lattice parameters and c/a ratio for this phase are plotted in Fig. 5.12 as a function of pressure. From this figure, we see that the c-axis is slightly more compressible than the a-axis, but overall the tetragonal structure is relatively stiff. The c/a ratio was fitted to a line to find the linear dependence on pressure and the theoretical zero-pressure value. Those results can be found in Table 5.5.

Finally, equation of state parameters were calculated for the cotunnite-type phase of UO_2. For this phase, we found a zero-pressure volume and bulk modulus of 23.02(6) cm^3/mole and 187(4) GPa, respectively, holding K_0' fixed at 4. The thermal pressure parameter was found to be 0.0052(3) GPa/K. These values are more similar to uraninite than the tetragonal phase of this material. No experimental high P-T equation of state parameters exist for this material, but our results are comparable to calculations. Geng et al. (2007) predicted a V_0 of 22.81 cm^3/mole and a K_0 or 192.5 GPa, while Perry et al. (2017) calculated a V_0 of 23.82 cm^3/mole and K_0 of 151.4 GPa. As with the cotunnite-type phase of ThO_2, the lattice parameters of this phase change anisotropically as a function of pressure (Fig. 5.13). Interestingly, while the predicted zero-pressure values for the ratios of the cotunnite-type phase in both ThO_2 and UO_2 are similar, they appear to be changing at different rates. This is particularly true for the c/b ratio, which depends negatively on pressure for ThO_2,

Table 5.5: Linear fits to the lattice parameter ratios as a funciton of pressure for the tetragonal and cotunnite-type polymorphs of UO_2.

Tetragonal UO_2		
Ratio	**Slope (GPa^{-1})**	**Zero-pressure value**
c/a	-0.00049(7)	1.301(3)
Cotunnite-type UO_2		
c/a	0.00074(2)	1.1465(7)
b/a	0.00029(1)	0.5978(4)
c/b	0.00033(2)	1.917(1)

but positively on pressure in UO_2. As with ThO_2, the anisotropic change in lattice parameters as a function of pressure here suggests the instability of this phase at high pressures, which is further supported by a phase transition or decomposition at around 80 GPa at high temperatures.

5.6 Conclusions

This chapter describes the investigation of the high-pressure, high-temperature phase diagrams of the actinide oxides ThO_2 and UO_2. We find that ThO_2 exists in the fluorite-type structure (thorianite) up to ∼20 GPa, at which point it begins the transformation process to the cotunnite-type structure. This phase transition occurs stepwise, by which the anion sublattice deforms first, locally decreasing the density of the material and allowing the cations to relocate. As such, it is very sluggish at room temperature. The low-pressure phase was observed to metastably coexist with the high-pressure phase at room temperature to the highest pressures reached in this study, 60 GPa. This transition is also kinetically inhibited at high temperatures, where the low- and high-pressure phases coexisted between 19-30 GPa. With this study, we were able to approximate the phase boundary as nearly veritcal around 20 GPa. The high P-T phase diagram of UO_2 is more complicated than the Th counterpart. UO_2 also exists in the fluorite-type structure (uraninite) to ∼30 GPa, although it is metastably present in the XRD measurements to nearly 40 GPa at high temperatures. At higher pressures and lower temperatures, a new phase has been identified. This phase has been indexed to a previously unreported tetragonal crystal structure, likely the $I4/mmm$ space group. Our data are consistent with the tetragonal phase as the stable low-temperature phase of UO_2 above 35 GPa. At higher temperatures, the tetragonal phase transforms to the cotunnite-type phase. This phase boundary appears to have a positive Clapeyron slope as a function of pressure. At even higher temperatures, a new peak is observed in the cotunnite-type XRD pattern, which cannot be assigned to the cotunnite-type phase and likely does not represent a monoclinic distortion of this phase.

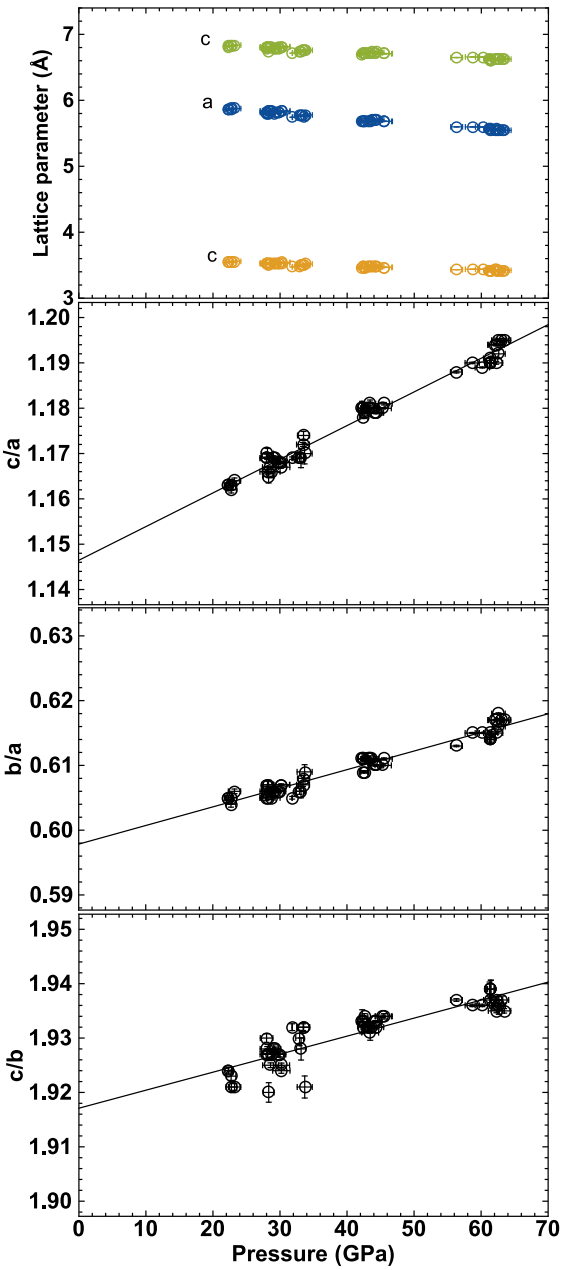

Figure 5.13: Measured lattice parameters and their ratios for cotunnite-type UO_2 as a function of pressure. The black curves were fit to the data. The results of those fits are in Table 5.5.

This peak is observed in several different samples across a wide range of P-T conditions, so it is likely linked to some kind of chemical reaction or disproportionation of the sample material at very high temperatures. The two highest pressure measurements in this study, at 79 and 95 GPa, revealed yet another transition. This modification resulted in a distinct change in the quality of the diffraction images, as well as a change in the laser-absorption properties of the material. It is either a transition to a new phase of UO_2 or a decomposition into two separate phases. None of the diffraction peaks can be indexed to any known phases of U metal, so if it is two distinct phases, they are likely both oxides.

In the crust and upper mantle, U and Th are primarily hosted in accessory phases, such as zircon ($ZrSiO_4$) (Blundy and Wood, 2003b). Our results on ThO_2 and UO_2 suggest that these elements can exist in accessory phases in the uppermost region of the lower mantle as well. ThO_2 and UO_2 likely exist as a solid solution in the cotunnite-type structure with other similar minerals such as ZrO_2 up to ~60 GPa, but it is plausible that a different mineral would host these elements at higher P-T conditions. One likely mineral host for these elements in the deepest mantle is Ca-Si-perovskite ($CaSiO_3$), which is a major phase in the lower mantle and has been shown to accomodate large cations at least

up to 25 GPa (Corgne, 2002; Corgne et al., 2003, 2005). This is also consistent with the general trend of increasing coordination number as a function of pressure; the actinide site is 8-fold coordinated in the fluorite-type structure, 9-fold coordinated in the cotunnite-type structure, and would be 12-fold coordinated in the Ca-site of the perovskite structure.

We were also able to extract thermal equation of state parameters for all identified phases of ThO_2 and UO_2. The data were fit to Mie-Grüneisen type equations of state with a Birch-Murnaghan reference curve and a constant thermal pressure parameter, αK_T. With a fixed volume for ambient pressure thorianite (V_0 = 26.379(7) cm^3/mole), we find K_0 = 204(2) GPa, holding the pressure derivative, K_0' equal to 4. The thermal parameter for this material is 0.0035(3) GPa/K. These parameters are very similar to the most recent XRD measurements of this material, as well as to the high-pressure cotunnite-type phase. The measured parameters for cotunnite-type ThO_2 are: V_0 = 24.75(6) cm^3/mole, K_0 = 190(3) (K_0' = 4), and αK_T = 0.0037(4). The similarity of the equations of state for the two phases suggests that although they have a ∼6% difference in density, they behave similarly under extreme pressure and temperature conditions. There are no other measurements of the equation of state parameters of cotunnite-type ThO_2 to date, but the measured values here are comparable to those from calculations.

The equation of state parameters for the polymorphs of UO_2 are similar to those for ThO_2. Uraninite has a measured zero-pressure volume V_0 of 24.538(1) cm^3/mole, which is slightly more dense than thorianite at the same condition. The bulk modulus for this phase is 175(7) GPa with a K_0' of 4.8(5) and αK_T of 0.0044(2). Cotunnite-type UO_2 behaves similarly, with K_0 = 187(4) (K_0' = 4) and αK_T = 0.0052(3). The zero-pressure volume for this phase is 6% more dense than uraninite, at V_0 = 23.02 cm^3/mole. In contrast, the tetragonal phase of UO_2 behaves differently than the other two polymorphs. The zero-pressure volume of this phase is intermediate at 23.9 cm^3/mole, while the bulk modulus is significantly higher at 220(20) GPa (holding K_0' fixed at 4). This makes tetragonal UO_2 much stiffer than the other two polymorphs. The thermal pressure parameter for this phase

is $\alpha K_T = 0.0043(7)$. It is important to note that tetragonal UO_2 exists under a relatively narrow range of conditions, and may not be present at all in the Earth except in cool regions of the uppermost lower mantle, such as in the very center of a subducted slab.

CHAPTER 6

CONCLUSIONS AND OUTLOOK

The research described in this dissertation utilizes both traditional high-pressure mineral physics techniques and newly developed extreme petrology techniques to understand the process of planetary differentiation and how that process resulted in the observable Earth. My research is driven by the following questions: 1) How do the long-lived radioactive elements U, Th, and K contribute to the energy budget of Earth's core, both as a component of the core and as a heat source on the core-mantle boundary? 2) Do radioactive elements, and other large cations, exist in distinct reservoirs within the mantle? 3) How do chemical reservoirs form within the deep Earth and how do they manifest as surface geochemistry? The answers to these interconnected questions have broad implications for how we interpret geochemical signals and our understanding of planetary formation.

To begin, in Chapter 3, I detailed metal–silicate partitioning experiments conducted in the laser-heated diamond anvil cell to better understand the chemical behavior of U, Th, and K under core formation conditions. Decay of these elements produces as much as 45% of the Earth's current heat budget, and this heat production was five times higher early in geologic time. However, it is unclear how this heat source has contributed to the dynamic evolution of Earth's core and mantle throughout the planet's history. For example, given their chemical behavior at the surface, it seems unlikely that radioactive elements should exist within the core in significant amounts. However, it is hard to explain the presence of the geomagnetic field early in Earth's history without a heat source such as radioactive decay. The experiments described in Chapter 3 are the first of their kind for U, Th, and K at the high pressures and temperatures relevant for core formation (up to 88 GPa and 5400 K). Using cutting-edge nanofabrication techniques, I recovered and chemically analyzed the samples. I used the resulting analyses to develop a thermodynamic parameterization of partitioning behavior of these elements with respect to the core formation pressure, temperature and chemical conditions. A principal result of this work is that U becomes significantly more

likely to partition into core material at very high temperatures and S contents of the metal, while SiO_2 content of the silicate melt (a rough proxy to parameterize melt composition) negatively affects partitioning of this element. Our data suggests that U is reduced to the 2+ valence state in high-pressure silicate melts, a state which has not been observed outside of organometallic synthesis. On the other hand, K and Th do not show significant partitioning into Fe-rich metal even at high pressures and temperatures. The core content of these two elements is negligible in terms of heat production at all conditions of core formation. Finally, experiments at these conditions show that even highly abundant lithophile elements, such as Mg, can partition into the core. In the future, this type of experiment will be used to better constrain mineral–mineral and mineral–melt interactions at the extreme pressure and temperature conditions of the lowermost mantle to understand whether distinct chemical reservoirs can exist at these conditions, how those reservoirs are stabilized, and how they are contributing to the geochemistry observed on the planet's surface. Additionally, metal–silicate partitioning within isotopic systems, such as lead, would address the first terrestrial Pb-isotope paradox, wherein samples from Earth's surface plot on the radiogenic end of the ^{207}Pb-^{206}Pb diagram rather than on the meteorite isochron as expected. The core could serve as a reservoir of lead in the deep Earth, explaining this phenomenon. Investigation of both the U-Pb system and the W-Hf system could plausibly affect the calculated ages of the Earth and core.

In Chapter 4, I used the parameterization of the behavior of radioactive elements in metal–silicate interactions within a 1-dimensional numerical model of the core's energy and entropy budget to quantify the effect radioactive decay would have on core properties, including the core-mantle boundary temperature through time and the inner core age. The maximum concentration of radioactive elements in the core would lower the inferred initial core-mantle boundary temperature by a few hundred degrees and extend the age of the inner core by 45 million years, not enough to preclude widespread mantle melting for most of Earth's history. Interestingly, widespread melting in the lower mantle would likely

result in concentrating these radioactive elements near the core-mantle boundary due to their incompatibility in mantle minerals. This radioactive heat source would actually decrease the heat flow out of the core. Interactions between this highly radiogenic silicate melt and liquid metal at the core-mantle boundary would also promote additional partitioning of these elements into the core if diffusion across the CMB is sufficiently efficient, such that a possible consequence of not having a significant radiogenic heat source in the core is an increased metal–silicate partitioning of these elements after the core has formed. Metal–silicate partitioning experiments at extreme conditions have also demonstrated the ability of very abundant lithophile elements such as Mg to partition into the core. These abundant elements, while not contributing directly to the energy budget, could produce an gravitational potential energy source if they precipitate out of the metal phase as oxides and silicates while the core is cooling. Our parameterization of Mg partitioning suggests that this element could not have partitioned to a great enough extent that it would saturate within the metal phase. However, our models did not include a period of very high temperatures, such as after a giant impact, which would likely result in much more Mg in the core. In the future, it would be useful for simulations to explore core formation under a wider range of conditions. These simulations must also be coupled to the energy budget of the mantle in the future, as they depend entirely on heat being extracted from the core and into the mantle.

In the lower mantle, radioactive elements could be hosted in accessory minerals such as oxides as they are on the surface. Chapter 5 details the first *in situ* high-pressure, high-temperature investigation of the phase behavior of the actinide oxides, UO_2 and ThO_2. I find that, as at room temperature, ThO_2 exists in the fluorite-type structure up to moderate pressures and temperatures, at which point it transforms to the orthorhombic contunnite-type phase. The phase transition process proceeds stepwise, with a period of anion sub-lattice rearrangement followed by cation rearrangement. This transition is very sluggish and takes place over a range of $\sim$20 GPa at room temperature and 10 GPa at high temperatures. The

high-pressure polymorph of ThO_2 is stable up to the highest pressures and temperatures achieved in this study, 60 GPa and 2600 K. The phase behavior of UO_2 is more complicated. It, too, exists in the fluorite-type structure to moderate P-T conditions. However, at higher pressures, the stable phase is a previously unidentified tetragonal structure. This new structure transforms to the cotunnite-type phase at higher temperatures. At the highest pressures reached in this study, UO_2 undergoes another transition or a disproportionation into two separate phases. The results of this study suggest that UO_2 and ThO_2 may exist in a solid solution in the cotunnite-type structure with similar materials such as ZrO_2 in the upper part of the lower mantle, but that they are accommodated in a different mineral at deeper conditions. This study also allowed us to extract thermoelastic parameters for each of these phases, which are necessary when modeling the behavior of these materials at extreme conditions, such as in the deep Earth or in certain industrial settings, such as in a nuclear reactor. In the future, this work could be extended to other more complicated actinide-bearing minerals, such as coffinite ($USiO_4$) and thorite ($ThSiO_4$), and more major minerals within the lower mantle, such as Ca-Si-perovskite ($CaSiO_3$), which has been shown to accommodate cations such as the actinides.

APPENDIX A

A HIGH *P-T* EQUATION OF STATE OF B2 KCL FOR USE AS AN *IN SITU* PRESSURE STANDARD IN THE DIAMOND ANVIL CELL

This chapter is based on: Chidester, B.A., Thompson, E.C., Fischer, R.A., Heinz, D.L., Prakapenka, V.B., and Campbell, A.J. (in prep) An experimental thermal equation of state of B2 KCl.

A.1 Introduction

Alkali halides are simple ionic solids that have been studied under a wide variety of conditions, making them useful benchmark materials to compare between dynamic and static compressional environments. Additionally, their crystallographic simplicity and relatively high compressibilities ($K_0 = \sim$10-30 GPa) make them useful as pressure transmitting media and potentially sensitive pressure markers in high-pressure X-ray diffraction (XRD) experiments (Decker et al., 1972). Furthermore, they are chemically inert and are transparent to near-infrared light, which facilitates their use in high-temperature experiments, such as laser heating in a diamond anvil cell (LH-DAC). Potassium chloride (KCl) has a higher melting point at high pressures than NaCl or LiF (Boehler et al., 1997), but is less electronically dense than KBr or CsI, making it optimal among alkali halides as a pressure medium, pressure standard and thermal insulator for this type of high pressure-temperature (P-T) XRD experiment.

The room temperature phase behavior and equations of state of KCl have been investigated up to 165 GPa (Vaidya et al., 1971; Yagi, 1978; Campbell and Heinz, 1991; Dewaele et al., 2012). Early studies of KCl in the diamond anvil cell at room temperature were conducted without the benefit of a (quasi)-hydrostatic pressure medium (Vaidya et al., 1971; Yagi, 1978; Campbell and Heinz, 1991), and the only high-temperature study of this material

was limited to 8 GPa and 873 K (Walker et al., 2002). More recently, Dewaele et al. (2012) have extended the room temperature data to 165 GPa under hydrostatic conditions using He as the pressure medium and ruby as the pressure standard. Similar to other alkali halides, KCl exhibits the NaCl (B1, $Fm3m$) crystal structure at ambient conditions, and transforms to the CsCl (B2, $Pm3m$) structure around 2.6 GPa at room temperature (Dewaele et al., 2012). No other solid phase transitions of this material have been observed up to 165 GPa at room temperature, nor is one expected at high temperatures in this pressure range.

As high P-T experiments in the laser-heated diamond anvil cell routinely push conditions to pressures above 100 GPa and temperatures of several thousand K, a high-temperature, high-pressure equation of state of KCl is necessary to use this material as a pressure standard for this type of experiment. In addition to high-pressure, room-temperature experiments, Dewaele et al. (2012) performed molecular dynamics simulations to generate a constant thermal pressure coefficient, $\alpha K_T = 0.00224$ GPa/K. This value is similar to the thermal pressure coefficient experimentally measured between room temperature and 873 K by Walker et al. (2002), 0.00275 GPa/K, while both of these coefficients are slightly lower than the constant $\alpha K_T = 0.0036$ GPa/K that can be calculated assuming a constant $C_V = 3$nR from the Grüneisen parameter, $\gamma = 2.30$, derived from acoustic wave velocity measurements (Campbell and Heinz, 1994). A more accurate equation of state requires experimental data to be obtained over a greater range of simultaneous high-temperature, high-pressure conditions. This study combines new high P-V-T synchrotron XRD data for KCl up to 167 GPa and 2400 K with previous high-pressure, room-temperature data from Dewaele et al. (2012) toward the aim of making KCl a useful and reliable pressure standard for future high-pressure experiments.

A.2 Methods

KCl (reagent grade) and Pt (99.9+%, 325 mesh) were purchased from Alfa Aesar. To remove adsorbed moisture, the KCl was baked at ∼100 °C prior to sample preparation. Generally,

LH-DAC samples consist of a thin foil of opaque sample material encased between layers of a soft, transparent material that acts as both the thermal insulator and as the quasi-hydrostatic pressure medium for the experiment. It is possible to use the pressure medium/thermal insulator as an internal pressure calibrant as well (see Campbell et al. (2009), for example). Thus, the samples in this study were configured to produce an equation of state of KCl specifically for use as a pressure standard in this type of sample geometry. Here, platinum (Pt) metal was used as the pressure calibrant and laser absorbing foil. Pt foils of $\sim$5 μm thick were secured between two layers of dried KCl of $\sim$10-20 μm thick. Samples were loaded into diamond anvil cells using Re as the gasket material and diamond culets of 300, 150 or 100 μm in diameter. The entire cell assembly was then dried at 100 °C for $\geq$30 minutes to ensure total removal of moisture immediately prior to closing and pressurizing the cell. Pressure-volume-temperature (P-V-T) data were collected by compressing to a target pressure and collecting powder X-ray diffraction (XRD) patterns at increasing (and/or decreasing) temperatures during laser heating.

Synchrotron angle dispersive X-ray diffraction (Fig. A.1) was conducted at beamlines 13-ID-D (GSE-CARS) and 16-ID-B (HP-CAT) of the Advanced Photon Source, Argonne National Laboratory. Laser-heating experiments at beamline 13-ID-D were done with monochromatic incident radiation ($\lambda = 0.3344$ or 0.2952 Å) measuring 2.2 by 4 μm (Prakapenka et al., 2008). Laser-heating experiments at beamline 16-ID-B were done with monochromatic incident radiation ($\lambda = 0.4066$ Å) measuring 6 by 7.5 μm (Meng et al., 2006). Sample to detector distances and tilt were calibrated using LaB_6 or CeO_2, respectively. In both cases, the laser was co-aligned with the incident X-rays using the X-ray induced fluorescence of KCl. Laser-heating of the samples was done from both sides, adjusting upstream and downstream laser powers to balance temperatures. The highest pressure measurements (sample B86) were conducted using "burst" mode, where the lasers were enabled at the desired laser power only during XRD collection. This allowed the DAC to stay cool enough that the laser-to-X-ray alignment was maintained throughout the entire heating cycle. Surface temperatures were

determined spectroradiometrically using the greybody approximation (Prakapenka et al., 2008; Meng et al., 2006), which were then corrected by -6% for an axial temperature gradient through the thickness of the metal to determine the average temperature of the Pt foil (Campbell et al., 2007). The average KCl temperature was taken as the temperature at the midpoint between the surface of the sample and the surface of the diamond anvils; thus, the estimated average temperature of the KCl pressure medium is $T_{KCl} = (3T_{surface} + 295)/4 \pm (T_{surface} - 295)/4$. While this results in a large uncertainty on the KCl temperature, it is reasonable for alkali halides because their compressibility far outweighs their thermal expansion (Campbell et al., 2009).

Powder X-ray diffraction patterns were collected on a CCD and integrated azimuthally to intensity vs. 2θ plots (e.g. Fig. 1) using Dioptas (Prescher and Prakapenka, 2015). Reflection positions were fit to determine lattice parameters as a function of pressure and temperature using PeakFit (Systat Software). A minimum of two reflections was used to determine the lattice parameters of KCl. As was observed in Dewaele et al. (2012), the KCl (200) reflection yielded systematically higher lattice parameters than all other lines, so it was not accounted for in the volume calculation. Pressure in these experiments was measured using the high P-T equation of state of Pt (Dorogokupets and Oganov, 2007).

A.3 Thermal Equation of State

The thermal equation of state (EOS) of B2-KCl was determined at high pressures and temperatures for use as a pressure standard in high P-T X-ray diffraction (XRD) experiments in the diamond anvil cell. The measured pressure-volume-temperature (P-V-T) data from four experiments are listed in Table SA.1 (Supplemental Materials). Fig. A.1 shows a sample diffraction pattern from this study at 31.6 GPa and 1194 K. As expected, the powder diffraction patterns became more "spotty," as opposed to uniformly defined rings, as temperatures increased. This is due to recrystallization and growth at high temperature and was more apparent in Pt than in KCl. By contrast, the KCl peaks tended to be broad because the

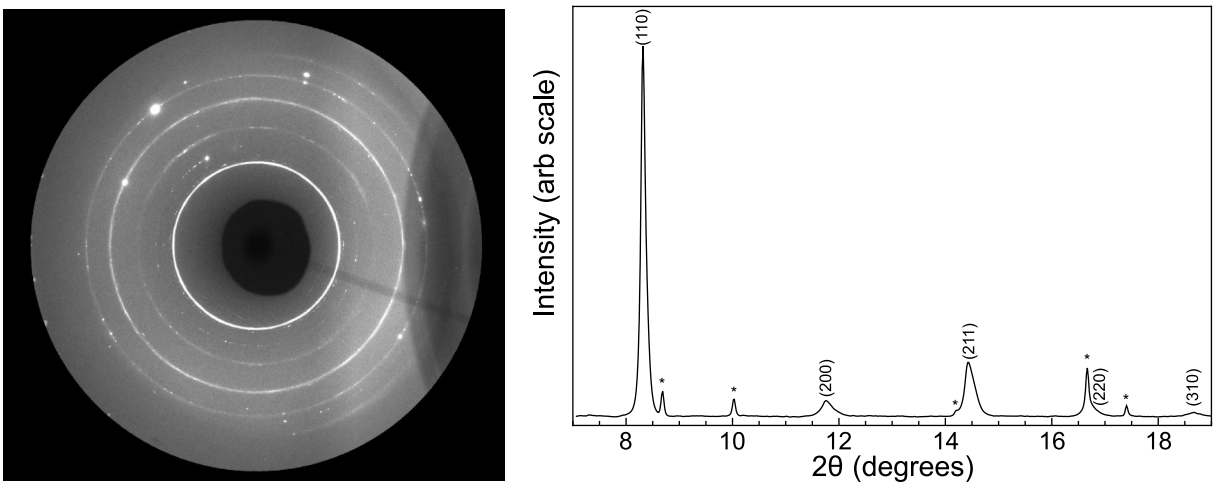

Figure A.1: Left: A typical XRD pattern from this study. Right: The integration of intensity vs. 2θ (degrees) of the pattern on the left. The asterisks indicate reflections from the Pt pressure standard, while the KCl reflections are noted with their respective Miller indices (hkl). This pattern was collected at 31.6 GPa and 1194 K (Pt temperature).

X-rays are sampling KCl at a range of temperatures between the Pt surface and the diamond culet. When possible, data were measured primarily on cooling to minimize lattice strain within the KCl. All experiments in this study were conducted above 15 GPa to stabilize and protect the diamonds during laser heating. This is well above the B1-to-B2 phase transition in KCl, reported at ∼2.6 GPa (Dewaele et al., 2012). No other phase transitions were observed up to 167 GPa and 2400 K in this study. Sample B2 was measured at both sector 13-ID-D and sector 16-ID-B. There was no distinguishable difference between these data.

We fit the high temperature data of B2 KCl, along with the room temperature data reported by Dewaele et al. (2012), to a Mie-Grüneisen-Debye (M-G-D) thermal equation of state, defined as:

$$P = P_{300} + P_{thermal}, \tag{A.1}$$

where the room temperature data are described by:

$$P_{300,BM} = 3K_0 f(1+2f)^{\frac{5}{2}}(1+\frac{3}{2}(K_0'-4)f). \tag{A.2}$$

Here, $P_{300,BM}$ is the Birch-Murnaghan (Birch, 1978) isothermal equation of state at 300 K,

f is the Eulerian strain ($\frac{1}{2}((\frac{V}{V_0})^{\frac{-2}{3}} - 1)$), V_0 is the inferred zero-pressure volume, K_0 and K_0' are the isothermal zero-pressure bulk modulus and its pressure derivative.

Interestingly, while Dewaele et al. (2012) chose the Rydberg-Vinet (R-V) functional form for their isothermal equation of state, we found that a Birch-Murnaghan (B-M) EOS better describes their room temperature data, particularly at low pressures near the B1-B2 transition. With the R-V fit, the lower pressure, room temperature residuals exhibit a monotonic trend with pressure, which the authors attributed to the B1-B2 phase transition affecting the bulk modulus of the B2 phase. This led them to fit only their lowest pressure data (2-6 GPa) to determine V_0. We find that when we fit the data to the B-M EOS, the residuals do not show such a trend with pressure and a reasonable, albeit slightly higher, V_0 can be inferred by fitting all of the data simultaneously. The resulting parameters for the calculated equations of state are given in Table A.1, along with the thermal EOS parameters available in the literature. In terms of the room temperature B-M EOS, our fit agrees well with the literature data. The inferred zero pressure volume, V_0, is 32.0(3) cm^3/mole, which is the same as reported by both Campbell and Heinz (1991) and Walker et al. (2002), within error. The bulk modulus, $K_0 = 24(1)$ GPa is very similar to that reported by Walker et al. (2002), but lower than the 28.7 GPa reported by Campbell and Heinz (1991). This discrepancy is likely due to the fact that those authors chose to fix the pressure derivative of the bulk modulus, K_0', to 4. The larger pressure range sampled by this study allowed us to more precisely fit this parameter to 4.56(5). There is a trade off between the V_0 and K_0' with K_0, which is especially pronounced when comparing B-M and R-V-type fits. Higher initial volumes promote higher compressibility and a high change in compressibility with pressure. The room temperature equation of state fitting is demonstrated in Fig. A.2, along with the data from Dewaele et al. (2012) for reference.

The thermal contribution to pressure, $P_{thermal}$, is described by:

$$P_{thermal} = \frac{\gamma}{V} \times (E_{harmonic,T} - E_{harmonic,300K}), \tag{A.3}$$

Table A.1: Fitted equation of state parameters for KCl.

V_0 **(cm^3/mole)**	K_0 **(GPa)**	K_0'	γ_0	q	**Reference (type of fit)**
32.0(3)	24(1)	4.56(5)	2.9(4)	1.0(1)	This study
34.3(5)	13(1)	6.2(1)	3.4(4)	1.0(1)	This study (R-V reference EOS)
32.8	17.2	5.89	1.47	**1**	Dewaele et al. (2012) (R-V)
32.25	23.7	4.4	1.78	textbf1	Dewaele et al. (2012) (B-M)
31.83	28.7	4*	2.3	**1**	Campbell and Heinz (1991, 1994) (B-M, acoustic)

Bold values were held constant during fitting. The γ_0 from Dewaele et al. (2012) and Walker et al. (2002) were calculated from the provided αK_T by assuming $\frac{V}{C_V}$ was constant. Values in parentheses are errors on the last digit.

and

$$E_{harmonic} = 9nRT(\frac{T}{\theta_D})^3 \int_0^{\theta_D/T} \frac{x^3}{e^x - 1}\, dx. \tag{A.4}$$

$\gamma = \gamma_0(\frac{V}{V_0})^q$ is the Grüneisen parameter, q is a constant, V is the volume in cubic centimeters per mole, $E_{harmonic}$ is the harmonic contribution to thermal pressure at temperature (T), n is the number of atoms per mole KCl (2), R is the ideal gas constant, and θ_D is the ambient pressure Debye temperature, 235 K (Campbell and Heinz, 1994).

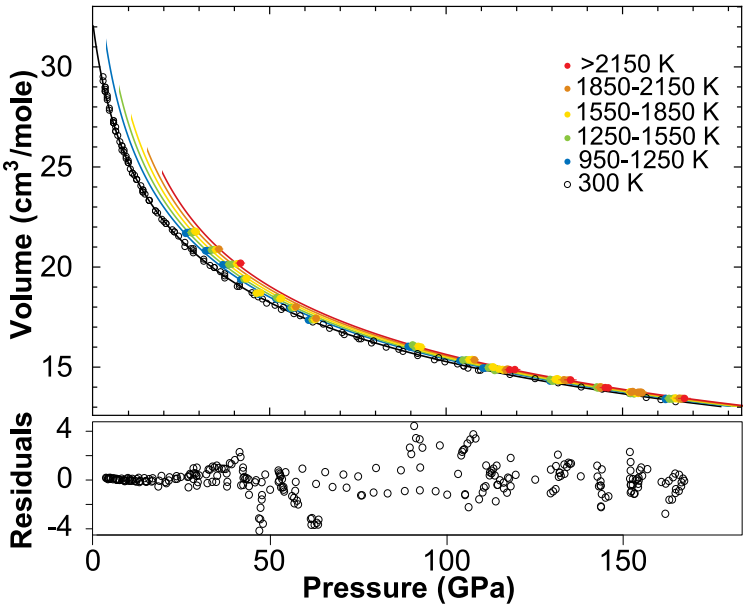

Figure A.2: **Top:** High P-T KCl data. Open black circles are room temperature data from Dewaele et al. (2012). High temperature data are color-coded by median temperature. Solid curves are isotherms calculated from the B-M equation of state parameters in Table A.1. **Bottom:** Residuals to the fit of all the data.

Instead of fitting a constant thermal pressure term (αK_T), we chose to fit our data to the full Debye energy as in Eq. A.4. The thermal parameters, γ_0 and q, that describe our data are 2.9(4) and 1.0(1), respectively. The high-temperature data are also presented in Fig. A.2. They are color coded by median temperature and plotted along with their corresponding isotherms. The root-mean-square misfit to the data over the whole pressure and tempera-

ture range is 1.6 GPa. The region of largest error falls between 40 and 100 GPa, as shown in the residuals plot in Fig. A.2. In this pressure range, the two largest XRD peaks in the high-temperature data, the (110) of KCl and the (111) of Pt, cross in 2θ space. We attribute the misfit to the high-temperature data in this range to variations in calculated volume as a result of slight overlaps of these two peaks.

Our fitted q value of 1.0(1) is typical and means that the Grüneisen parameter is linear with volume. The fitted value of γ_0 is higher than expected based on both previous static experiments and the available shock-wave data (van Thiel, 1977). By assuming q is 1 and C_V is equal to the Debye limit, $3nR$, the value of γ_0 can be solved for based on the published parameters of Dewaele et al. (2012) and Walker et al. (2002) to be 1.47 and 1.78, respectively, using the relationship $\frac{\gamma}{V}=\frac{\gamma_0}{V_0}=\frac{\alpha K_T}{C_V}$. The discrepancy of about a factor of two between the value measured here and that of Dewaele et al. (2012) can be attributed to the difference between calculations and high temperature experiments. Additionally, the data in Walker et al. (2002) were only measured up to 8 GPa and <1000 K. One would not expect these parameters to be easily extrapolated over a wide P-T range. The γ_0 value measured acoustically by Campbell and Heinz (1994) is closer to our value, at 2.3, but this study was also limited in pressure and temperature. Figure A.3 shows the comparison between the thermal equations of state reported in the literature and our fit up to 170 GPa. The R-V fit from this study gener-

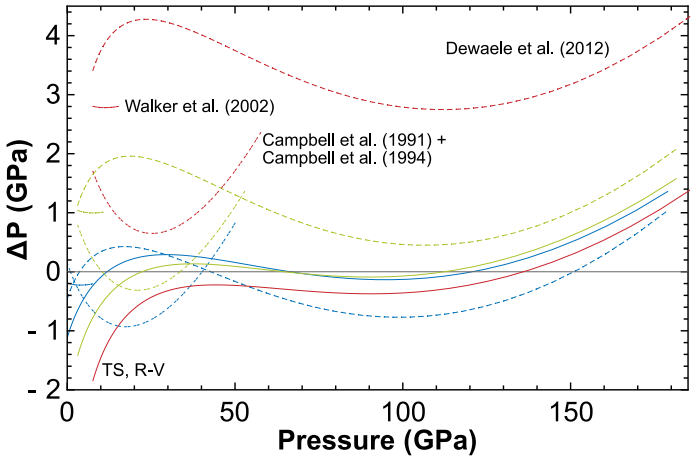

Figure A.3: Difference in calculated equations of state (P-$P_{BM,300}$(This study)) as a function of pressure. Blue curves are calculated at 300 K, green at 1000 K and red at 2000 K. Different studies are represented by different dash formatting and are noted on the plot. Curves are plotted over the range of pressure measured in each study, respectively.

ally matches our B-M EOS to +/- 1 GPa, but overestimates the pressure slightly at low pressures and high temperatures. All of the thermal EOSs available in the literature do a reasonable job reproducing our data at room temperature, but underestimate the pressure at high temperatures by as much as 4 GPa.

Figure A.4 shows the 300 K isotherm resulting from this study, along with the principal adiabat and the principal shock Hugoniot calculated using our thermal equation of state and equation A.5.

$$P_H = \frac{\frac{V}{\gamma}P_S + \int_{V_0}^{V} P_S dV - \Delta E_{\rm tr}}{\frac{V}{\gamma} - \frac{V_{00}-V}{2}}(5) \tag{A.5}$$

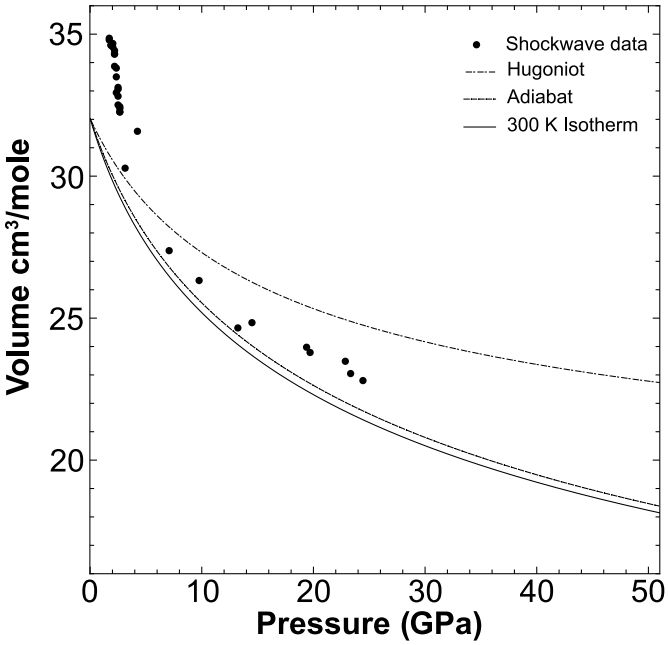

Figure A.4: The 300 K isotherm, principal isentrope and Hugoniot curves for KCl calculated from the high temperature EOS. The measured shockwave data are shown for comparison. The B2 data end at ∼25 GPa, at which point the material melts.

P_H is the Hugoniot compression curve, P_S is the principal adiabatic compression curve, $\Delta E_{\rm tr}$ is the change in energy due to the B1-B2 phase transition (31.4 J/mole) (Campbell and Heinz, 1994), and V_{00} is the ambient pressure volume of the B1 phase (37.55 J/mole) (Dewaele et al., 2012). The available shockwave data from van Thiel (1977) are also included in Fig. A.5. It is clear that our predicted Hugoniot overestimates the pressure when compared with the data. This is due to the high Grüneisen parameter in our equation of state. When fitting the shockwave data, we find that they are better described by a γ_0 of 1.6-1.7, depending on the reference equation of state used. These values are more in line with those in Dewaele et al. (2012) and Walker et al. (2002). However, Campbell and Heinz (1994) reported a similar discrepancy to the one observed here

between the γ_0 measured statically and the one extracted from the shockwave data. While the root cause of this discrepancy is unclear, possible causes may be differences in sample configuration or contamination of any of the samples by water.

A.4 Conclusions

We have measured high P-T synchrotron X-ray diffraction on KCl in the laser-heated diamond anvil cell. These data, combined with the room temperature data from Dewaele et al. (2012), were used to determine the Mie-Grüneisen-Debye equation of state for KCl. The 300 K Birch-Murnaghan equation of state parameters measured here are very similar to those reported in the literature. There is a marked tradeoff between the inferred V_0 term and the compressibility, which is exceptionally noticeable when comparing between Birch-Murnaghan and Rydberg-Vinet type fits. The thermal parameters, γ_0 and q, for KCl were found to be 2.9(4) and 1.0(1), respectively. This γ_0 value is higher than expected based on the calculations from Dewaele et al. (2012) and the available shockwave data from van Thiel (1977), but is consistent with that measured acoustically by Campbell and Heinz (1994). The measurements here extend the available data to super-megabar pressures and several thousand degrees kelvin. This greatly expanded dataset has made a more robust high P-T equation of state possible, which will allow KCl to be used as an *in situ* pressure standard for high pressure-temperature XRD experiments in the laser-heated diamond anvil cell.

APPENDIX B

SYNCHROTRON XANES MEASUREMENTS OF CATION OXIDATION STATES IN SILICATE MELTS FROM LASER-HEATED DIAMOND ANVIL CELL EXPERIMENTS

Portions of this chapter are included in: Shofner G.A., Campbell A.J., Chidester B.A., Danielson L.R., Lanzirotti A., Rahman Z., and Righter K. (In Prep) Metal–silicate partitioning of tungsten from 10 to 50 GPa: Implications for core formation.

B.1 Introduction

In Chapter 3, the dependence of metal–silicate partitioning of trace elements on various thermodynamic variables, including pressure, temperature, oxygen fugacity (fO_2), chemical composition is discussed. As a reminder, the exchange of trace elements with Fe, as occurs in metal–silicate interactions, is most easily described by a reaction of the form:

$$MO_{n/2} + \frac{n}{2}Fe \rightarrow \frac{n}{2}FeO + M, \tag{B.1}$$

where the cation of interest, M, is reduced to a metal by exchanging O with Fe. In this reaction, n is the oxidation state of the cation M. The resulting exchange coefficient for this reaction, K_D^M is defined as

$$K_D^M = \frac{\frac{X_M}{X_{MO_{n/2}}}}{(\frac{X_{Fe}}{X_{FeO}})^{n/2}} = \frac{D_M}{(D_{Fe})^{n/2}}. \tag{B.2}$$

Typically in high-pressure metal–silicate experiments, the value of n is either assumed a priori based on known behavior at ambient conditions, or else is inferred from the data. That is, if all of the data in a metal–silicate partitioning study are collected under a relatively narrow range of P-T-X conditions, plotting the partition coefficient D_M against fO_2 (which in

our case is related to D_{Fe} by Eq. 3.1), the slope of the data should be equal to $-\frac{n}{4}$, thus allowing the oxidation state of the cation in the silicate melt to be inferred. However, if experiments are done over a wide range of conditions, the scatter in the data related to dependences on variables other than fO_2 make inferring the oxidation state of the cation much more challenging. For example, in Chapter 3 the oxidation state of U has been inferred as 2+, rather than 4+ which was observed in lower pressure experiments and expected based on surface chemistry of this element. It is unclear whether this is the true state of U in silicate melts at high P-T conditions, or whether this inferred value is a result of co-varying parameters in our fit.

Fortunately, there is a method by which the oxidation state of various cations can be measured directly. This method, known as X-ray Absorption Near Edge Spectroscopy (XANES), relies on the absorption of X-rays by the core electrons of the element of interest. The premise of this method is that a core electron is forced out of its shell to a higher energy level when a beam of X-rays focused on the sample sweeps across the binding energy of that electron. There is a standard value for the absorption edge energy for every element in its zero-valence state. When an element is oxidized by removing a valence electron, the relative force on the core electrons from the nucleus increases. In other words, the binding energy of a core electron is increased due to oxidation of an element, effectively shifting the absorption edge to higher energies. The X-ray absorption edge for an element often varies linearly in energy with the oxidation state, a phenomenon known as Kunzl's law (Kunzl, 1932). With proper standardization for the cation in different oxidation states, the unknown oxidation state of that cation within the silicate glass of a metal–silicate partitioning sample should be measurable.

In addition to oxidation state, XANES provides other useful information. When the core electron falls back to its orginal shell it emits X-rays of characteristic energy. This X-ray emission allows the sample to be imaged and the distribution of various elements to be mapped across the sample. By standardizing peak intensity as a function of concentra-

tion, as is done with the more common technique of UV-Vis absorption spectroscopy, X-ray emission can also be used to quantify the concentrations of elements within the sample. Another useful property of XANES spectra is that they often exhibit structure near the absorption edge which can be informative of the environment that the cation is in, including nearest-neighbor distance and bonding environment. In this study, we used synchrotron-based XANES to measure the oxidation states of W and U in silicate melts of recovered metal–silicate partitioning samples from the laser-heated diamond anvil cells. A synchrotron source was necessary for these measurements, as a very intense and tightly focused X-ray beam was necessary to measure the very tiny samples in this study (∼20x20x1 μm).

B.2 XANES methods

Micro X-ray absorption near edge structure (μXANES) spectra on samples G34, G36, and B56 were collected at beamline 13-ID-E (GSE-CARS) of the Advanced Photon Source, Argonne National Laboratory. A monochromatic X-ray beam from a Si(111) double crystal monochromator was focused on the sample by a set of 240 mm long highly polished mirrors in a Kirkpatrick-Baez (KB) geometry. Grazing incidence focusing was done using Rh stripes for the best focus at the highest intensity. The incident X-ray beam measured 1 μm x 2 μm. Sample fluorescence intensities were normalized to the incident X-ray beam (I_0) measured in a helium-cooled ion chamber upstream of the KB mirror optics. To differentiate between the metal and silicate portions of the sample, X-ray fluorescence (XRF) maps were taken of each sample. Fluorescence intensity measurements were made using a four-element silicon-drift-diode detector array (Vortex-ME4, Hitachi High-Technologies Science America, Inc.) with pulse-processing provided by an Xspress 3 digital X-ray processor system (Quantum Detectors). μXANES measurements for both W and U were then taken in fluorescence mode at several points within the silicate melt by scanning over the L_{III}-absorption edge (10,207 eV for W, 17,166 eV). For example, the W measurements consisted of sweeps over 10,107-10,192 eV in 5 eV steps, 10,192-10,217 eV in 0.2 eV steps and 10,217-10,450 eV with variable

energy steps between 0.2-3.0 eV. The measurement pre-edge, edge, and post-edge ranges for U were similar. The fluorescence mode spectra were corrected for detector dead time and normalized to a pre-edge value of 0 and a post edge value of 1 prior to analysis. Because of the low W and U concentrations in these samples, several absorption edge spectra were taken at each point, and these spectra were then merged to improve the signal-to-noise of the data.

The W reference standard foils (W metal, $W^{4+}O_2$ and $W^{6+}O_3$) were measured in transmission mode. Due to safety regulations, no standard materials for the U measurements were available on sight at the beamline. Instead, standard spectra from several previous measurements for a range of U-bearing materials with oxidation states of 4+ and 6+ were graciously provided by the beamline scientist, Dr. Anthony Lanzirotti. No spectra for metallic U were available, so determination of U^{2+} had to be in relation to the oxidation state vs. energy curve from the 4+ and 6+ data. Analysis of the μXANES data (samples and standards), including spectrum merging and normalization, was completed using the Athena software from the Horae software package (Ravel and Newville, 2005). The absorption edge energy (E_0) for each standard and sample was defined as the center of the first significant peak in the first derivative spectrum.

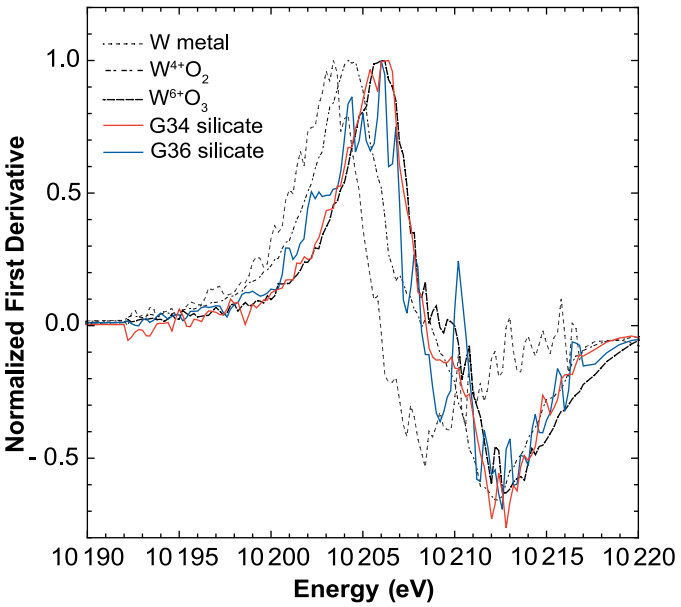

Figure B.1: The first derivative of the normalized W-μXANES curve at the W-L_{III} absorption edge. After differentiation, the curves were renormalized to the maximum value of each curve for ease of visualization. Curves are given for each of the standards (W metal, $W^{4+}O_2$ and $W^{6+}O_3$) and for the silicate glasses in G34 and G36. G34 has W in the 6+ oxidation state. G36 could contain W as either 6+ or as a mixture of 4+ and 6+ cations.

B.3 Results: Oxidation state of W

XANES measurements on W were measured as a complement to the PhD thesis on the metal–silicate partitioning of W by Dr. Gregory Shofner. Fig. B.1 shows the first derivatives of the standard curves, along with those for the silicate melts in samples G34 and G36. The absorption edge energies for the W, $W^{4+}O_2$ and $W^{6+}O_3$ standards were 10203.4 eV, 10204.4 eV and 10206.0 eV, respectively. The first derivative curve for sample G34 matches the standard curve for W^{6+}, indicating that the tungsten in the silicate glass in this sample is primarily 6+. The first derivative curve for G36 is noisier and broader than that for G34, but is indicative of a more oxidized silicate as well. It is likely that this sample contained some W^{4+} along with W^{6+}. This matches well with the oxidation state of W inferred by fitting the data as a function of fO_2, which found an intermediate value of ∼5+. These results were used to inform metal–silicate exchange between W and Fe in models of core formation similar to those described in Chapter 3.3.1 for U.

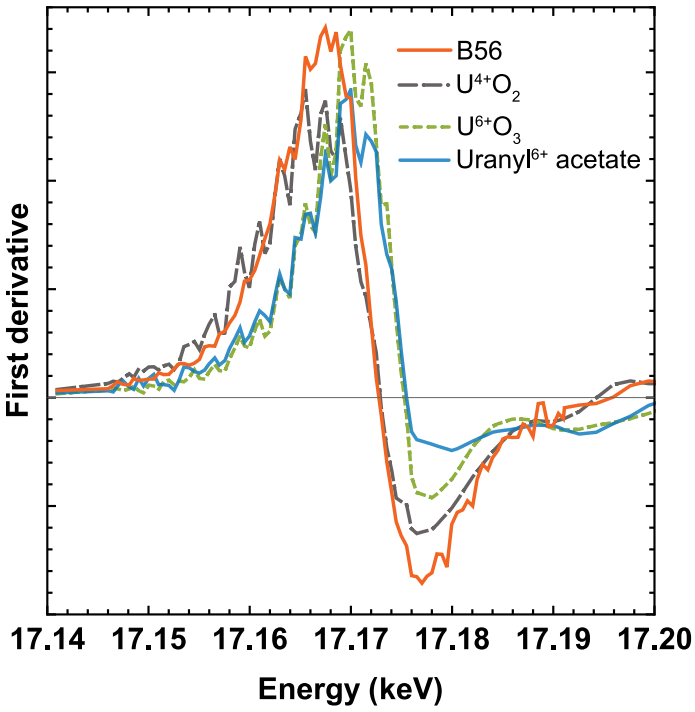

Figure B.2: The first derivative of the normalized U-μXANES curve at the U-L_{III} absorption edge. Curves are given for each of the standards ($U^{4+}O_2$, $U^{6+}O_3$ and uranyl acetate (6+)) and for the silicate glass in B56. U in B56 appears to be in the 4+ oxidation state

B.4 Results: Oxidation state of U

As mentioned above, standards were not available for U at the time of data collection, so spectra from previous measurements were provided by the beamline scientist, Dr. Anthony Lanzirotti. The standards used in these measurements are UO_2 (4+ oxidation

state), UO_3 (6+ oxidation state), and uranyl acetate. The uranyl cation is equivalent to $UO_2{}^{2+}$, meaning the U is in the 6+ oxidation state. Even though the synchrotron allowed for measurements as small as 1x2 μm, only one U-bearing sample had good enough spatial resolution to make XANES measurements, B56, recovered from 41 GPa and 4000 K. Chemical information on this sample can be found in Chapter 3. Figure B.2 compares the XANES spectrum from the silicate glass in B56 compared with the available standard spectra. From this figure, it appears that U was in the 4+ oxidation state in the silicate melt of this sample. However, when we inferred the oxidation state of U at these conditions from thermodynamic parameterization, we determined it to be 2+. There are several possible reasons for this discrepancy. It is possible that the measurement is correct and the metal–silicate partitioning of U has some dependence that we are not capturing with our fit. It is also possible that U does exist in the 2+ state in the silicate liquid, but that upon quenching the sample to ambient conditions it oxidizes to 4+ since electron transfer occurs more rapidly than our samples cool. Another possible explanation is that U exists in 2+ in the silicate melt, but that they were oxidized during illumination with the X-ray beam at the synchrotron. This possibility is supported by the fact that chemical measurements of the sample in the SEM after synchrotron measurements showed the metal phases within samples to be much more oxidized than they had been prior to the measurements. Thus, we have deemed our U-XANES measurements inconclusive.

APPENDIX C

A NUMERICAL MODEL OF THE ENERGY AND ENTROPY BUDGET OF EARTH'S CORE

This code is written in the syntax of Mathematica 10.2.0.0.

$G = 6.67408 * 10\text{^} - 11; m\text{^}3/\text{kgs}\text{^}2;$

$\rho\text{cen} = 12500; \text{kg}/m\text{^}3;$

$\rho 0 = 7900; \text{kg}/m\text{^}3;$

$\text{K0} = 500 * 10\text{^}9; \text{Pa};$

$\text{Pc} = 139; \text{GPa};$

$\text{rc} = 3480; \text{km};$

$\text{Cp} = 840; J/\text{kgK};$

$\alpha = 1.25 * 10\text{^} - 5; /K;$

$\text{Tm0} = 2677; K;$

$\text{Tm1} = 2.98 * 10\text{^} - 3; \text{GPa}\text{^} - 1;$

$\text{Tm2} = 8.4 * 10\text{^} - 7; \text{GPa}\text{^} - 2;$

$\text{Lh} = 750; \text{kJ}/K;$

$\Delta\rho\text{c} = 560; \text{kg}/m\text{^}3;$

$\text{Mc} = 1.92667 * 10\text{^}24; \text{kg};$

$\text{kc} = 130; W/\text{mK};$

$\text{Dk} = 5900; \text{km};$

$\text{lambda8} = \text{Log[2]}/(1.41 * 10\text{^}17); s\text{^} - 1;$

$\text{Wperkg8} = 9.46 * 10\text{^} - 5; W/\text{kg238U};$

$\text{lambda5} = \text{Log[2]}/(2.22 * 10\text{^}16); s\text{^} - 1;$

$\text{Wperkg5} = 5.69 * 10\text{^} - 4; W/\text{kg235U};$

$\text{lambdaK} = \text{Log[2]}/(3.946 * 10\text{^}16); s\text{^} - 1;$

WperkgK40 = 2.92 * 10^ − 5; W/kgK40;

lambdaTh = Log[2]/(4.4156 * 10^17); s^ − 1;

WperTh = 26.4 * 10^ − 6;

L = Sqrt[3 * K0 * (Log[ρcen/ρ0] + 1)/(2 * π * G * ρcen * ρ0)]/10^3; km;

De = Sqrt[3 * Cp/(2 * π * α * ρcen * G)]/1000; km;

Csq = 3 * L^2/16 − (1 − ((3 * rc^2)/(10 * L^2))) * (rc^2/2); km^2;

Fsqr = 1/(1/L^2 − 1/De^2); km^2;

A = Sqrt[1/(1/L^2 + 1/De^2)]; km;

Is = 4 * π * ρcen * (−A^2 * rc * Exp[−rc^2/A^2]/2 + A^3 * Sqrt[π] * Erf[rc/A]/4) * 10^9; kg;

B[r_]:=((3 * r^2)/10 − L^2/5) * Exp[−r^2/L^2]; km^2;

P[r_]:=Pc + (4 * π * G * ρcen^2 * 1000^2/3) * (B[rc] − B[r])/10^9; GPa;

Tm[r_]:=Tm0 * (1 + Tm1 * P[r] + Tm2 * P[r]^2); K;

ψ[r_]:=(2 * π * G * ρcen * r^2 * (1 − ((3 * r^2)/(10 * L^2)))/3) −

(2 * π * G * ρcen * rc^2 * (1 − ((3 * rc^2)/(10 * L^2)))/3); km^2/s^2;

Ta[r_, j_]:=Tcen[[j]] * Exp[−r^2/De^2]; K;

gr[r_]:=4 * π/3 * G * ρcen * (1 − ((3 * r^2)/(5 * L^2))); s^ − 2;

ρ[r_]:=ρcen * Exp[−r^2/L^2]; kg/m^3;

dt = −3.154 * 10^13; s/Myr;

Tcen = ConstantArray[5727, 4500]; K;

Tc = ConstantArray[4180, 4500]; K;

Qs = ConstantArray[$-1.851 * 10^{\wedge}15, 4500$]; TWs/$K$;

dTmdP[r_]:=Tm0 $*$ (Tm1 $+ 2 *$ Tm2 $* P[r]$); K/GPa;

dTadP[r_, j_]:=($-2 * r *$ Tcen[[j]]/De$^{\wedge}$2) $*$ Exp[$-r^{\wedge}2$/De$^{\wedge}$2]/($-\rho[r] *$ gr$[r] * r/10^{\wedge}3$); K/GPa;

dridt = ConstantArray[$-9.991, 4500$]; km/K;

Ql = ConstantArray[$-1.7033 * 10^{\wedge}15, 4500$]; TWs/$K$;

Moc = ConstantArray[$1.83318 * 10^{\wedge}24, 4500$]; kg;

int = ConstantArray[$-1.361 * 10^{\wedge}25, 4500$]; kgkm$^{\wedge}2/s^{\wedge}2$;

Qg = ConstantArray[$-1.015 * 10^{\wedge}15, 4500$]; TWs/$K$;

U8 = ConstantArray[$5.47 * 10^{\wedge} - 9, 4500$];

U5 = ConstantArray[$0.042 * 10^{\wedge} - 9, 4500$];

K40 = ConstantArray[$0.0001097 * 10^{\wedge} - 6, 4500$];

Th = ConstantArray[$7.4 * 10^{\wedge} - 9, 4500$];

h = ConstantArray[$7.4 * 10^{\wedge} - 25, 4500$];

Qr = ConstantArray[$1.42, 4500$];

It = ConstantArray[$4.05 * 10^{\wedge}20, 4500$];

Er = ConstantArray[$7.33, 4500$];

Qk = ConstantArray[$14.97, 4500$]; TW;

Ek = $((16 * \pi *$ kc $* 10^{\wedge}3 *$ rc$^{\wedge}5)/(5 *$ De$^{\wedge}4)) * (1 + (2/7) * (1/((\text{Dk}^{\wedge}2/\text{rc}^{\wedge}2) - 1)))/(10^{\wedge}6)$;

MW/K;

Es = ConstantArray[$-5.571 * 10^{\wedge}16, 4500$]; MWs/$K^{\wedge}2$;

El = ConstantArray[$-9.834 * 10^{\wedge}16, 4500$]; MWs/$K^{\wedge}2$;

Eg = ConstantArray[$-2.428 * 10\hat{}17, 4500$]; MWs/$K\hat{}2$;

Ephi = ConstantArray[$1046, 4500$]; MW/K;

Qcmb = ConstantArray[$18.2, 4500$]; TW;

dT = ConstantArray[$0.124, 4500$]; K;
ri = ConstantArray[$1220, 4500$]; km;
time = ConstantArray[$0, 4500$]; s;

For[$i = 1, i < 4500, i{+}{+}$;

Qs[[i]] = $-$(Cp/Tc[[$i - 1$]]) $*$ Tcen[[$i - 1$]] $*$ Is/$10\hat{}12$;
Es[[i]] = (Cp/Tc[[$i - 1$]]) $*$ (Mc $-$ (Is $*$ Tcen[[$i - 1$]])/Tc[[$i - 1$]])/$10\hat{}6$;

dridt[[i]] = If[ri[[$i - 1$]] $\leq 0, 0$,
(-1/(dTmdP[ri[[$i - 1$]]] $-$ dTadP[ri[[$i - 1$]], $i - 1$])) $*$
(Ta[ri[[$i - 1$]], $i - 1$]/(ρ[ri[[$i - 1$]]] $*$ gr[ri[[$i - 1$]]] $*$ ri[[$i - 1$]] $*$ 1000)) $*$
(1/Tc[[$i - 1$]]) $*$ $10\hat{}6$];

Ql[[i]] = $4 * \pi *$ ri[[$i - 1$]]$\hat{}2 *$ Lh $* \rho$[ri[[$i - 1$]]] $*$ dridt[[$i - 1$]];
El[[i]] =
(Ql[[$i - 1$]] $*$ (Ta[ri[[$i - 1$]], $i - 1$] $-$ Tc[[$i - 1$]])/(Ta[ri[[$i - 1$]], $i - 1$] $*$ Tc[[$i - 1$]])) $*$
$10\hat{}6$;

Moc[[i]] = $4 * \pi * \rho$cen $* 10\hat{}9 * (-L\hat{}2 *$ rc $*$ Exp[$-$rc$\hat{}2/L\hat{}2$]$/2 + L\hat{}3 *$ Sqrt[π] $*$ Erf[rc/L]$/4) -$
$4 * \pi * \rho$cen $* 10\hat{}9 *$

$(-L\text{^}2 * \text{ri}[[i-1]] * \text{Exp}[-\text{ri}[[i-1]]\text{^}2/L\text{^}2]/2 + L\text{^}3 * \text{Sqrt}[\pi] * \text{Erf}[\text{ri}[[i-1]]/L]/4);$

$\text{int}[[i]] = 8 * \pi\text{^}2 * \rho\text{cen}\text{^}2 * G * 10\text{^}9/3 *$

$(((3 * \text{rc}\text{^}5/20 - L\text{^}2 * (\text{rc}\text{^}3)/8 - L\text{^}2 * \text{Csq} * \text{rc}) * \text{Exp}[-\text{rc}\text{^}2/L\text{^}2] +$

$\text{Csq} * L\text{^}3 * \text{Sqrt}[\pi] * \text{Erf}[\text{rc}/L]/2) -$

$((3 * \text{ri}[[i-1]]\text{^}5/20 - L\text{^}2 * \text{ri}[[i-1]]\text{^}3/8 - L\text{^}2 * \text{Csq} * \text{ri}[[i-1]]) *$

$\text{Exp}[-\text{ri}[[i-1]]\text{^}2/L\text{^}2] + \text{Csq} * L\text{^}3 * \text{Sqrt}[\pi] * \text{Erf}[\text{ri}[[i-1]]/L]/2));$

$\text{Qg}[[i]] = (\text{int}[[i-1]] - \text{Moc}[[i-1]] * \psi[\text{ri}[[i-1]]]) * \Delta\rho\text{c} * 10\text{^}9 * 4 * \pi * \text{ri}[[i-1]]\text{^}2 *$

$\text{dridt}[[i-1]]/(\text{Moc}[[i-1]] * 10\text{^}6);$

$\text{Eg}[[i]] = \text{Qg}[[i-1]] * 10\text{^}6/\text{Tc}[[i-1]];$

$\text{Qk}[[i]] = (8 * \pi * \text{rc}\text{^}3 * \text{kc} * 10\text{^}3 * \text{Tc}[[i-1]])/\text{De}\text{^}2/10\text{^}12;$

$\text{U8}[[i]] = \text{U8}[[i-1]]/\text{Exp}[\text{lambda8} * \text{dt}];$

$\text{U5}[[i]] = \text{U5}[[i-1]]/\text{Exp}[\text{lambda5} * \text{dt}];$

$\text{K40}[[i]] = \text{K40}[[i-1]]/\text{Exp}[\text{lambdaK} * \text{dt}];$

$\text{Th}[[i]] = \text{Th}[[i-1]]/\text{Exp}[\text{lambdaTh} * \text{dt}];$

$h[[i]] = \text{U8}[[i-1]] * \text{Wperkg8}/10\text{^}12 + \text{U5}[[i-1]] * \text{Wperkg5}/10\text{^}12 +$

$\text{K40}[[i-1]] * \text{WperkgK40}/10\text{^}12 + \text{Th}[[i-1]] * \text{WperTh}/10\text{^}12;$

$\text{Qr}[[i]] = h[[i-1]] * \text{Mc};$

$\text{It}[[i]] = ((4 * \pi * \rho\text{cen} * 10\text{^}9 * \text{rc}\text{^}3)/(3 * \text{Tcen}[[i-1]])) * (1 - (3/5) * (\text{rc}\text{^}2/\text{Fsqr}));$

$\text{Er}[[i]] = (\text{Mc}/\text{Tc}[[i-1]] - \text{It}[[i-1]]) * h[[i-1]];$

$\text{If}[\text{ri}[[i-1]] > 0,$

$\text{Ephi}[[i]] =$

$((\text{Es}[[i-1]] + \text{El}[[i-1]] + \text{Eg}[[i-1]])/(\text{Qs}[[i-1]] + \text{Ql}[[i-1]] + \text{Qg}[[i-1]])) *$

$(\text{Qcmb}[[i-1]] -$

```
Qr[[i - 1]] *
(1 - ((Qs[[i - 1]] + Ql[[i - 1]] + Qg[[i - 1]])/(Es[[i - 1]] + El[[i - 1]] + Eg[[i - 1]])) *
(Er[[i - 1]]/Qr[[i - 1]]))) - Ek, Ephi[[i]] = 100];

If[ri[[i - 1]] ≤ 0,
Qcmb[[i]] = Qr[[i]]/(1 + 2.5 * (L^2/rc^2)) + Qk[[i]] * (1 + (Ephi[[i]]/Ek)),
Qcmb[[i]] = 18.2];

dT[[i]] = ((Qcmb[[i - 1]] - Qr[[i - 1]])/(Qs[[i - 1]] + Ql[[i - 1]] + Qg[[i - 1]])) * dt;

Tc[[i]] = Tc[[i - 1]] + dT[[i - 1]];
Tcen[[i]] = Tc[[i]]/Exp[-rc^2/De^2];
ri[[i]] = ri[[i - 1]] + dridt[[i - 1]] * dT[[i - 1]];
If[ri[[i]] ≤ 0, ri[[i]] = 0];
time[[i]] = time[[i - 1]] + dt; ];
```

APPENDIX D

LIST OF SUPPLEMENTARY MATERIAL

S5.1 Measured lattice parameters and P-V-T data for thorianite

S5.2 Measured lattice parameters and P-V-T data for cotunnite-type ThO_2

S5.3 Measured lattice parameters and P-V-T data for uraninite

S5.4 Measured lattice parameters and P-V-T data for tetragonal UO_2

S5.5 Measured lattice parameters and P-V-T data for cotunnite-type UO_2

SA.1 Measured P-V-T data for KCl

REFERENCES

Akahama, Y. and Kawamura, H. (2007). Diamond anvil Raman gauge in multimegabar pressure range. *High Pressure Research*, 27(4):473–482.

Alfe, D., Gillan, M., and Price, G. (2003). Thermodynamics from first principles: temperature and composition of the Earth's core. *Mineralogical Magazine*, 67(1):113–123.

Alfe, D., Gillan, M. J., and Price, G. D. (2002). Ab-initio chemical potentials of solid and liquid solutions and the chemistry of the Earth's core. *The Journal of Chemical Physics*, 116(16):7127.

Alfè, D., Price, G. D., and Gillan, M. J. (2002). Iron under Earth's core conditions: Liquid-state thermodynamics and high-pressure melting curve from ab initio calculations. *Physical Review B*, 65(16):165118.

Allègre, C. J. (1968). Comportement des systemes U-Th-Pb dans le manteau superieur et modele d'evolution de ce dernier au cours des temps geologiques. *Earth and Planetary Science Letters*, 5:261–269.

Amit, H. and Olson, P. (2015). Lower mantle superplume growth excites geomagnetic reversals. *Earth and Planetary Science Letters*, 414:68–76.

Andrault, D., Bolfan-Casanova, N., Nigro, G. L., Bouhifd, M. A., Garbarino, G., and Mezouar, M. (2011). Solidus and liquidus profiles of chondritic mantle: Implication for melting of the Earth across its history. *Earth and Planetary Science Letters*, 304(1-2):251–259.

Arevalo, R., McDonough, W. F., and Luong, M. (2009). The K/U ratio of the silicate Earth: Insights into mantle composition, structure and thermal evolution. *Earth and Planetary Science Letters*, 278:361–369.

Badro, J., Siebert, J., and Nimmo, F. (2016). An early geodynamo driven by exsolution of mantle components from Earth's core. *Nature*, 536:326–328.

Benedict, U., Andreeti, G. D., Fournier, J. M., and Waintal, A. (1982). X-ray powder diffraction study of the high pressure behavior of uranium dioxide. *Journal de Physique*, 43:L–171 – L–177.

Biggin, A. J., de Wit, M. J., Langereis, C. G., Zegers, T. E., Voûte, S., Dekkers, M. J., and Drost, K. (2011). Palaeomagnetism of Archaean rocks of the Onverwacht Group, Barberton Greenstone Belt (southern Africa): Evidence for a stable and potentially reversing geomagnetic field at ca. 3.5Ga. *Earth and Planetary Science Letters*, 302(3-4):314–328.

Birch, F. (1978). Finite strain isotherm and velocities for single-crystal and polycrystalline NaCl at high pressures and 300. *J. Geophys. Res.*, 83(7):1257–1268.

Blundy, J. and Wood, B. (2003a). Partitioning of trace elements between crystals and melts. *Earth and Planetary Science Letters*, 210(3-4):383–397.

Blundy, J. D. and Wood, B. J. (2003b). Mineral-melt partitioning of uranium, thorium, and their daughters. *Reviews in Mineralogy and Geochemistry*, 52:59–123.

Boehler, R., Ross, M., and Boercker, D. B. (1997). Melting of LiF and NaCl to 1 Mbar: Systematics of ionic solids at extreme conditions. *Physical Review Letters*, 78(24):4589–4592.

Boettger, J. C. (2009). Theoretical Zero-Temperature Isotherm and Structural Phase Stability of Thorium Dioxide. *International Journal of Quantum Chemistry*, 109:3564–3569.

Boudjemline, A., Louail, L., Islam, M. M., and Diawara, B. (2011). Dependence of pressure on elastic, electronic and optical properties of CeO2 and ThO2: A first principles study. *Computational Materials Science*, 50(7):2280–2286.

Bouhifd, M. A., Andrault, D., Bolfan-Casanova, N., Hammouda, T., and Devidal, J. L. (2013). Metal-silicate partitioning of Pb and U: Effects of metal composition and oxygen fugacity. *Geochimica et Cosmochimica Acta*, 114:13–28.

Bouhifd, M. A., Gautron, L., Bolfan-Casanova, N., Malavergne, V., Hammouda, T., Andrault, D., and Jephcoat, A. P. (2007). Potassium partitioning into molten iron alloys at high-pressure: Implications for Earth's core. *Physics of the Earth and Planetary Interiors*, 160(1):22–33.

Bouhifd, M. A. and Jephcoat, A. P. (2011). Convergence of Ni and Co metal-silicate partition coefficients in the deep magma-ocean and coupled silicon-oxygen solubility in iron melts at high pressures. *Earth and Planetary Science Letters*, 307:341–348.

Boujibar, A., Andrault, D., Bouhifd, M. A., Bolfan-Casanova, N., Devidal, J. L., and Trcera, N. (2014). Metal-silicate partitioning of sulphur, new experimental and thermodynamic constraints on planetary accretion. *Earth and Planetary Science Letters*, 391:42–54.

Boulfelfel, S. E., Zahn, D., Hochrein, O., Grin, Y., and Leoni, S. (2006). Low-dimensional sublattice melting by pressure: Superionic conduction in the phase interfaces of the fluorite-to-contunite transition of CaF2. *Physical Review B - Condensed Matter and Materials Physics*, 74(9):094106.

Boultif, A. and Louër, D. (2004). Powder pattern indexing with the dichotomy method. *Journal of Applied Crystallography*, 37(5):724–731.

Boyet, M. and Carlson, R. W. (2005). 142Nd evidence for early (>4.53 Ga) global differentiation of the silicate Earth. *Science*, 309:576–581.

Boyet, M. and Carlson, R. W. (2006). A new geochemical model for the Earth's mantle inferred from 146Sm-142Nd systematics. *Earth and Planetary Science Letters*, 250(1-2):254–268.

Boyet, M. and Carlson, R. W. (2007). A highly depleted moon or a non-magma ocean origin for the lunar crust? *Earth and Planetary Science Letters*, 262(3-4):505–516.

Buffett, B. A. (2002). Estimates of heat flow in the deep mantle based on the power requirements for the geodynamo. *Geophysical Research Letters*, 29(12):1566.

Buffett, B. A. and Christensen, U. R. (2007). Magnetic and viscous coupling at the core-mantle boundary: Inferences from observations of the Earth's nutations. *Geophysical Journal International*, 171(1):145–152.

Buffett, B. A., Huppert, H. E., Lister, J. R., and Woods, A. W. (1996). On the thermal evolution of Earth's core. *Journal of Geophysical Research*, 101(B4):7989–8006.

Bukowinski, M. S. T. (1976). The Effect of Pressure on the Physics and Chemistry of Potassium. *Geophysical Research Letters*, 3(8):491–494.

Burke, K. and Torsvik, T. H. (2004). Derivation of Large Igneous Provinces of the past 200 million years from long-term heterogeneities in the deep mantle. *Earth and Planetary Science Letters*, 227(3-4):531–538.

Campbell, A. J. (2008). Measurement of temperature distributions across laser heated samples by multispectral imaging radiometry. *Review of Scientific Instruments*, 79:015108.

Campbell, A. J., Danielson, L., Righter, K., Seagle, C. T., Wang, Y., and Prakapenka, V. B. (2009). High pressure effects on the iron-iron oxide and nickel-nickel oxide oxygen fugacity buffers. *Earth and Planetary Science Letters*, 286(3-4):556–564.

Campbell, A. J. and Heinz, D. L. (1991). Compression of KCl in the B2 structure to 56 GPa. *Journal of Physics and Chemistry of Solids*, 52(3):495–499.

Campbell, A. J. and Heinz, D. L. (1994). High-pressure acoustic wave velocites and equations of state of the alkali chlorides. *Journal of Geophysical Research*, 99(B6):11,765–11,774.

Campbell, A. J., Seagle, C. T., Heinz, D. L., Shen, G., and Prakapenka, V. B. (2007). Partial melting in the iron-sulfur system at high pressure: A synchrotron X-ray diffraction study. *Physics of the Earth and Planetary Interiors*, 162(1-2):119–128.

Canup, R. M., Visscher, C., Salmon, J., and Fegley Jr, B. (2015). Lunar Volatile Depletion Due To Incomplete Accretion Within An Impact-Generated Disk. *Nature Geoscience*, 8(December):918–921.

Cartier, C., Hammouda, T., Boyet, M., and Bouhifd, M. A. (2014). Redox control of the fractionation of niobium and tantalum during planetary accretion and core formation. *Nature Geoscience*, 7(8):573–576.

Cartier, C., Hammouda, T., Boyet, M., Mathon, O., Testemale, D., and Moine, B. N. (2015). Evidence for Nb 2+ and Ta 3+ in silicate melts under highly reducing conditions: A XANES study. *American Mineralogist*, 100:2152–2158.

Christensen, U. R. (2010). Dynamo scaling laws and applications to the planets. *Space Science Reviews*, 152(1-4):565–590.

Christensen, U. R. and Tilgner, A. (2004). Power requirement of the geodynamo from ohmic losses in numerical and laboratory dynamos. *Nature*, 429(6988):169–171.

Clausen, K., Hayes, W., Macdonald, J. E., Osborn, R., Schnabel, P. G., Hutchings, M. T., and Magerl, A. (1987). Inelastic neutron scattering investigation of the lattice dynamics of ThO2 and CeO2. *Journal of the Chemical Society, Faraday Transactions 2*, 83(7):1109–1112.

Connelly, J. N. and Bizzarro, M. (2016). Lead isotope evidence for a young formation age of the EarthMoon system. *Earth and Planetary Science Letters*, 452:36–43.

Corgne, A. (2002). CaSiO3 and CaTiO3 perovskite-melt partitioning of trace elements: Implications for gross mantle differentiation. *Geophysical Research Letters*, 29(19):3–6.

Corgne, A., Allan, N. L., and Wood, B. J. (2003). Atomistic simulations of trace element incorporation into the large site of MgSiO3 and CaSiO3 perovskites. *Physics of the Earth and Planetary Interiors*, 139(1-2):113–127.

Corgne, A., Keshav, S., Fei, Y., and McDonough, W. F. (2007). How much potassium is in the Earth's core? New insights from partitioning experiments. *Earth and Planetary Science Letters*, 256(3-4):567–576.

Corgne, A., Liebske, C., Wood, B. J., Rubie, D. C., and Frost, D. J. (2005). Silicate perovskite-melt partitioning of trace elements and geochemical signature of a deep perovskitic reservoir. *Geochimica et Cosmochimica Acta*, 69(2):485–496.

Cuney, M. (2013). Uranium and thorium resources and the sustainability of nuclear energy. In Burns, P. C. and Sigmon, G. E., editors, *Uranium: Cradle to Grave, Mineralogical Association of Canada Short Course Series Volume 43*, chapter 15, pages 417–437. Mineralogical Association of Canada.

Dancausse, J.-P., Gering, E., Heathman, S., and Benedict, U. (1990). Pressure-induced phase transition in ThO2 and PuO2. *High Pressure Research*, 2(5-6):381–389.

de Koker, N., Steinle-Neumann, G., and Vlcek, V. (2012). Electrical resistivity and thermal conductivity of liquid Fe alloys at high P and T, and heat flux in Earth's core. *Proceedings of the National Academy of Sciences of the United States of America*, 109(11):4070–4073.

Decker, D. L., Bassett, W. A., Merrill, L., Hall, H. T., and Barnett, J. D. (1972). High Pressure Calibration: A Critical Review. *Journal of Physical and Chemical Reference Data*, 1(3):773–836.

Dewaele, A., Belonoshko, A. B., Garbarino, G., Occelli, F., Bouvier, P., Hanfland, M., and Mezouar, M. (2012). High-pressure-high-temperature equation of state of KCl and KBr. *Physical Review B - Condensed Matter and Materials Physics*, 85(21):214105.

Dorogokupets, P. I. and Oganov, A. R. (2007). Ruby, metals, and MgO as alternative pressure scales: A semiempirical description of shock-wave, ultrasonic, x-ray, and thermochemical data at high temperatures and pressures. *Physical Review B - Condensed Matter and Materials Physics*, 75(2):1–16.

Filiberto, J., Treiman, A. H., and Le, L. (2008). Crystallization experiments on a Gusev Adirondack basalt composition. *Meteoritics & Planetary Science*, 43(7):1137–1146.

Fiquet, G., Auzende, a. L., Siebert, J., Corgne, A., Bureau, H., Ozawa, H., and Garbarino, G. (2010). Melting of Peridotite to 140 Gigapascals. *Science*, 329(5998):1516–1518.

Fischer, R. A., Nakajima, Y., Campbell, A. J., Frost, D. J., Harries, D., Langenhorst, F., Miyajima, N., Pollok, K., and Rubie, D. C. (2015). High pressure metalsilicate partitioning of Ni, Co, V, Cr, Si, and O. *Geochimica et Cosmochimica Acta*, 167:177–194.

Fonseca, R. O. C., Mallmann, G., Sprung, P., Sommer, J. E., Heuser, A., Speelmanns, I. M., and Blanchard, H. (2014). Redox controls on tungsten and uranium crystal/silicate melt partitioning and implications for the U/W and Th/W ratio of the lunar mantle. *Earth and Planetary Science Letters*, 404:1–13.

Frost, D. J., Asahara, Y., Rubie, D. C., Miyajima, N., Dubrovinsky, L. S., Holzapfel, C., Ohtani, E., Miyahara, M., and Sakai, T. (2010). Partitioning of oxygen between the Earth's mantle and core. *Journal of Geophysical Research: Solid Earth*, 115:B02202.

Ganguly, J. (2009). *Thermodynamics in Earth and Planetary Sciences*. Springer.

Garnero, E., Lay, T., and McNamara, A. (2007). Implications of lower-mantle structural heterogeneity for the existence and nature of whole-mantle plumes. In Fouler, G. and Jurdy, D., editors, *Plates, Plumes, and Planetary Processes*, pages 79–101. Geological Society of America Special Paper 430.

Geng, H. Y., Chen, Y., Kaneta, Y., and Kinoshita, M. (2007). Structural behavior of uranium dioxide under pressure by LSDA+U calculations. *Physical Review B - Condensed Matter and Materials Physics*, 75(5):1–8.

Gessmann, C. K. and Wood, B. J. (2002). Potassium in the Earth's core? *Earth and Planetary Science Letters*, 200:63–78.

Gomi, H. and Hirose, K. (2015). Electrical resistivity and thermal conductivity of hcp FeNi alloys under high pressure: Implications for thermal convection in the Earth's core. *Physics of the Earth and Planetary Interiors*, 247:2–10.

Gomi, H., Hirose, K., Akai, H., and Fei, Y. (2016). Electrical resistivity of substitutionally disordered hcp FeSi and FeNi alloys: Chemically-induced resistivity saturation in the Earth's core. *Earth and Planetary Science Letters*, 451:51–61.

Gomi, H., Ohta, K., Hirose, K., Labrosse, S., Caracas, R., Verstraete, M. J., and Hernlund, J. W. (2013). The high conductivity of iron and thermal evolution of the Earth's core. *Physics of the Earth and Planetary Interiors*, 224:88–103.

Greaux, S., Gautron, L., Andrault, D., Bolfan-Casanova, N., Guignot, N., and Bouhifd, M. A. (2009). Experimental high pressure and high temperature study of the incorporation of uranium in Al-rich CaSiO3 perovskite. *Physics of the Earth and Planetary Interiors*, 174(1-4):254–263.

Greaux, S., Gautron, L., Andrault, D., Bolfan-Casanova, N., Guignot, N., and Haines, J. (2008). Structural characterization of natural UO2 at pressures up to 82 GPa and temperatures up to 2200 K. *American Mineralogist*, 93(7):1090–1098.

Grove, T. L. and Parman, S. W. (2004). Thermal evolution of the Earth as recorded by komatiites. *Earth and Planetary Science Letters*, 219(3-4):173–187.

Gubbins, D., Alfe, D., Masters, G., Price, G. D., and Gillan, M. J. (2003). Can the Earth's dynamo run on heat alone? *Geophysical Journal International*, 155(2):609–622.

Harding, J. H., Lindan, P. J. D., and Pyper, N. C. (1994). The cohesion of thorium dioxide. *Journal of Physics: Condensed matter*, 6:6485–6496.

Helffrich, G. and Kaneshima, S. (2010). Outer-core compositional stratification from observed core wave speed profiles. *Nature*, 468:807–810.

Hirao, N., Ohtani, E., Kondo, T., Endo, N., Kuba, T., Suzuki, T., and Kikegawa, T. (2006). Partitioning of potassium between iron and silicate at the core-mantle boundary. *Geophysical Research Letters*, 33(8):33–36.

Hirose, K., Labrosse, S., and Hernlund, J. (2013). Composition and State of the Core. *Annual Review of Earth and Planetary Sciences*, 41(1):657–691.

Hirose, K., Morard, G., Sinmyo, R., Umemoto, K., Hernlund, J., Helffrich, G., and Labrosse, S. (2017). Crystallization of silicon dioxide and compositional evolution of the Earth's core. *Nature*, 543(7643):99–102.

Idiri, M., Le Bihan, T., Heathman, S., and Rebizant, J. (2004). Behavior of actinide dioxides under pressure: UO2 and ThO2. *Physical Review B - Condensed Matter and Materials Physics*, 70(1):014113.

Jackson, M. G. and Jellinek, a. M. (2013). Major and trace element composition of the high 3He/ 4He mantle: Implications for the composition of a nonchonditic Earth. *Geochemistry, Geophysics, Geosystems*, 14(00):2954–2976.

Japan Society for the Advancement of Science and the 19th Committee on Steelmaking (1988). *Steelmaking Data Sourcebook*. Gordon and Breach Science Publishers, New York, rev. ed. edition.

Jaupart, C., Labrosse, S., and Mareschal, J. C. (2007). Temperatures, Heat and Energy in the Mantle of the Earth. *Treatise on Geophysics*, 7:253–303.

Javoy, M., Kaminski, E., Guyot, F., Andrault, D., Sanloup, C., Moreira, M., Labrosse, S., Jambon, A., Agrinier, P., Davaille, A., and Jaupart, C. (2010). The chemical composition of the Earth: Enstatite chondrite models. *Earth and Planetary Science Letters*, 293(3-4):259–268.

Jayaraman, A., Kourouklis, G. A., and van Uitert, L. G. (1988). A high pressure raman study of ThO2 to 40 GPa and pressure-induced phase transition from fluorite structure. *Pramana - Journal of Physics*, 30(3):225–231.

Kanchana, V., Vaitheeswaran, G., Svane, A., and Delin, A. (2006). First-principles study of elastic properties of CeO2 , ThO2 and PoO2. *Journal of Physics: Condensed Matter*, 18(42):9615–9624.

Kawanishi, S., Yoshikawa, T., and Tanaka, T. (2009). Equilibrium Phase Relationship between SiC and a Liquid Phase in the Fe-Si-C System at 15231723 K. *Materials Transactions*, 50(4):806–813.

Kelly, P. J. and Brooks, M. S. S. (1987). Electronic-Structure And Ground-State Properties Of The Actinide Dioxides. *J. Chem. Soc., Faraday Trans. 2*, 83(7):1189–1203.

Konôpková, Z., McWilliams, R. S., Gómez-Pérez, N., and Goncharov, A. F. (2016). Direct measurement of thermal conductivity in solid iron at planetary core conditions. *Nature*, 534:99–101.

Kuang, W. and Bloxham, J. (1997). An Earth-like numerical dynamo model. *Nature*, 389(6649):371–374.

Kunzl, V. (1932). A linear dependence of energy levels on the valency of elements. *Collection des Travaux de Chimie de Tchecoslovaquie*, 4:213–224.

Labrosse, S. (2003). Thermal and magnetic evolution of the Earth's core. *Physics of the Earth and Planetary Interiors*, 140(1-3):127–143.

Labrosse, S., Poirier, J. P., and Le Mouël, J. L. (2001). The age of the inner core. *Earth and Planetary Science Letters*, 190:111–123.

Lay, T., Hernlund, J., and Buffett, B. A. (2008). Coremantle boundary heat flow. *Nature Geoscience*, 1:25–32.

Lee, K. K. M. and Jeanloz, R. (2003). High-pressure alloying of potassium and iron: Radioactivity in the Earth's core? *Geophysical Research Letters*, 30(23):3–6.

Lee, K. K. M., Steinle-Neumann, G., and Jeanloz, R. (2004). Ab-initio high-pressure alloying of iron and potassium: Implications for the Earth's core. *Geophysical Research Letters*, 31(11):1–4.

Leinders, G., Cardinaels, T., Binnemans, K., and Verwerft, M. (2015). Accurate lattice parameter measurements of stoichiometric uranium dioxide. *Journal of Nuclear Materials*, 459:135–142.

Li, J. and Agee, C. B. (2001). The effect of pressure, temperature, oxygen fugacity and composition on partitioning of nickel and cobalt between liquid Fe-Ni-S alloy and liquid silicate: Implications for the Earth's core formation. *Geochimica et Cosmochimica Acta*, 65:1821–1832.

Li, Q., Yang, J.-s., Huang, D.-h., Cao, Q.-l., and Wang, F.-h. (2014). Phase transition and thermodynamic properties of ThO2: Quasi-harmonic approximation calculations and anharmonic effects. *Chinese Physics B*, 23(1):017101.

Li, S., Ahuja, R., and Johansson, B. (2002). High pressure theoretical studies of actinide dioxides. *High Pressure Research*, 22:471–474.

Li, Y., Dasgupta, R., and Tsuno, K. (2015). The effects of sulfur, silicon, water, and oxygen fugacity on carbon solubility and partitioning in Fe-rich alloy and silicate melt systems at 3 GPa and 1600 C: Implications for core-mantle differentiation and degassing of magma oceans and reduced plane. *Earth and Planetary Science Letters*, 415:54–66.

Lock, S. J. and Stewart, S. T. (2017). The structure of terrestrial bodies: Impact heating, corotation limits, and synestias. *Journal of Geophysical Research: Planets*, pages 950–982.

Lord, O. T., Wood, I. G., Dobson, D. P., Vocadlo, L., Wang, W., Thomson, A. R., Wann, E. T. H., Morard, G., Mezouar, M., and Walter, M. J. (2014). The melting curve of Ni to 1 Mbar. *Earth and Planetary Science Letters*, 408:226–236.

MacDonald, M. R., Fieser, M. E., Bates, J. E., Ziller, J. W., Furche, F., and Evans, W. J. (2013). Identification of the +2 Oxidation State for Uranium in a Crystalline Molecular Complex, [K(2.2.2-Cryptand)][(C5H4SiMe3)3U]. *Journal of the American Chemical Society*, 135(36):13310–13313.

Macedo, P. M., Capps, W., and Wachtman Jr., J. B. (1964). Elastic constants of single crystal ThO2 at 25C. *Journal of the American Ceramic Society*, 47(12):651.

Malavergne, V., Tarrida, M., Combes, R., Bureau, H., Jones, J., and Schwandt, C. (2007). New high-pressure and high-temperature metal/silicate partitioning of U and Pb: Implications for the cores of the Earth and Mars. *Geochimica et Cosmochimica Acta*, 71:2637–2655.

McDonough, W. F. (2013). Compositional Model for the Earth's Core. In *Treatise on Geochemistry: Second Edition*, volume 3, pages 559–577. Elsevier Ltd., 3 edition.

McDonough, W. F. and Sun, S. s. (1995). The composition of the Earth. *Chemical Geology*, 120(3-4):223–253.

Meng, Y., Shen, G., and Mao, H. K. (2006). Double-sided laser heating system at HPCAT for in situ x-ray diffraction at high pressures and high temperatures. *Journal of physics. Condensed matter : an Institute of Physics journal*, 18(25):S1097.

Miettinen, J. (1998). Reassessed thermodynamic solution phase data for ternary Fe-Si-C system. *Calphad*, 22(2):231–256.

Murthy, V. R., van Westrenen, W., and Fei, Y. (2003). Experimental evidence that potassium is a substantial radioactive heat source in planetary cores. *Nature*, 423(6936):163–165.

Mysen, B. O. (1991). Relations between structure, redox equilibria of iron, and properties of magmatic liquids. In Perchuk, L. L. and Kushiro, I., editors, *Physical Chemistry of Magmas*, pages 41–98. Springer-Verlag New York.

Nimmo, F. (2015). Energetics of the Core. In *Treatise on Geophysics*, volume 8, pages 31–65. Elsevier B.V., 2 edition.

Ohta, K., Kuwayama, Y., Hirose, K., Shimizu, K., and Ohishi, Y. (2016). Experimental determination of the electrical resistivity of iron at Earth's core conditions. *Nature*, 534:95–98.

Olsen, J. S., Gerward, L., Kanchana, V., and Vaitheeswaran, G. (2004). The bulk modulus of ThO2an experimental and theoretical study. *Journal of Alloys and Compounds*, 381(1-2):37–40.

O'Neill, H. S. C. and Eggins, S. M. (2002). The effect of melt composition on trace element partitioning: An experimental investigation of the activity coefficients of FeO, NiO, CoO, MoO2 and MoO3 in silicate melts. *Chemical Geology*, 186(1-2):151–181.

O'Rourke, J. G., Korenaga, J., and Stevenson, D. J. (2017). Thermal evolution of Earth with magnesium precipitation in the core. *Earth and Planetary Science Letters*, 458:263–272.

O'Rourke, J. G. and Stevenson, D. J. (2016). Powering Earth's dynamo with magnesium precipitation from the core. *Nature*, 529:387–389.

Palme, H. and O'Neill, H. (2013). Cosmochemical Estimates of Mantle Composition. *Treatise on Geochemistry: Second Edition*, 3:1–39.

Pearce, N. J. G., Perkins, W. T., Westgate, J. A., Gorton, M. P., Jackson, S. E., Neal, C. R., and Chenery, S. P. (1997). A Compilation of New and Published Major and Trace Element Data for NIST SRM 610 and NIST SRM 612 Glass Reference Materials. *Geostandards and Geoanalytical Research*, 21(1):115–144.

Perry, S. N., Pigott, J. S., and Panero, W. R. (2017). Ab initio calculations of uranium and thorium storage in CaSiO 3 -perovskite in the Earth's lower mantle. *American Mineralogist*, 102:321–326.

Pozzo, M., Davies, C., Gubbins, D., and Alfè, D. (2012). Thermal and electrical conductivity of iron at Earth's core conditions. *Nature*, 485:355–358.

Pozzo, M., Davies, C., Gubbins, D., and Alfè, D. (2014). Thermal and electrical conductivity of solid iron and ironsilicon mixtures at Earth's core conditions. *Earth and Planetary Science Letters*, 393:159–164.

Prakapenka, V. B., Kubo, a., Kuznetsov, a., Laskin, a., Shkurikhin, O., Dera, P., Rivers, M. L., and Sutton, S. R. (2008). Advanced flat top laser heating system for high pressure research at GSECARS: application to the melting behavior of germanium. *High Pressure Research*, 28(3):225–235.

Prescher, C. and Prakapenka, V. B. (2015). DIOPTAS : a program for reduction of two-dimensional X-ray diffraction data and data exploration. *High Pressure Research*, 35(3):223–230.

Ravel, B. and Newville, M. (2005). ATHENA, ARTEMIS, HEPHAESTUS: Data analysis for X-ray absorption spectroscopy using IFEFFIT. *Journal of Synchrotron Radiation*, 12(4):537–541.

Righter, K. (2003). Metalsilicate partitioning of siderophile elements and core formation in the early Earth. *Annual Review of Earth and Planetary Science*, 31(1):135–174.

Righter, K., Danielson, L., Pando, K., Shofner, G., Sutton, S., Newville, M., and Lee, C.-T. (2016). Valence and metal/silicate partitioning of Mo: Implications for conditions of Earth accretion and core formation. *Earth and Planetary Science Letters*, 437:89–100.

Righter, K., Sutton, S. R., Newville, M., Le, L., Schwandt, C. S., Uchida, H., Lavina, B., and Downs, R. T. (2006). An experimental study of the oxidation state of vanadium in spinel and basaltic melt with implications for the origin of planetary basalt. *American Mineralogist*, 91:1643–1656.

Ringwood, A. E. (1966). Chemical evolution of the terrestrial planets. *Geochimica et Cosmochimica Acta*, 30(1):41–104.

Ringwood, A. E. and Hibberson, W. (1990). The System F e - FeO Revisited. *Physics and Chemistry of Minerals*, 17:313–319.

Roberts, P., Jones, C., and Calderwood, A. (2003). Energy fluxes and ohmic dissippation in the Earth's core. In Jones, C., Soward, A., and Zhang, K., editors, *Earth's core and lower mantle*, pages 123–157. Taylor & Francis, London.

Rodriguez-Carvajal, J. (1993). Recent advances in magnetic structure determination by neutron powder diffraction + FULLProf. *Physica B: Condensed Matter*, 192:55–56.

Ross, M., Mao, H. K., Bell, P. M., and Xu, J. A. (1986). The equation of state of dense argon: A comparison of shock and static studies. *Journal of Chemical Physics*, 85(2):1028–1033.

Rubie, D. C., Jacobson, S. A., Morbidelli, A., O'Brien, D. P., Young, E. D., de Vries, J., Nimmo, F., Palme, H., and Frost, D. J. (2015). Accretion and differentiation of the terrestrial planets with implications for the compositions of early-formed Solar System bodies and accretion of water. *Icarus*, 248:89–108.

Sanloup, C. and Fei, Y. (2004). Closure of the Fe-S-Si liquid miscibility gap at high pressure. *Physics of the Earth and Planetary Interiors*, 147(1):57–65.

Seagle, C. T., Cottrell, E., Fei, Y., Hummer, D. R., and Prakapenka, V. B. (2013). Electrical and thermal transport properties of iron and iron-silicon alloy at high pressure. *Geophysical Research Letters*, 40:1–5.

Sevik, C. and Çaln, T. (2009). Mechanical and electronic properties of CeO2, ThO2, and (Ce,Th)O2 alloys. *Physical Review B - Condensed Matter and Materials Physics*, 80(1):014108.

Shein, I. R., Shein, K. I., and Ivanovskii, A. L. (2007). Elastic and electronic properties and stability of SrThO3, SrZrO3 and ThO2 from first principles. *Journal of Nuclear Materials*, 361(1):69–77.

Shofner, G. A. (2011). *High pressure redox geochemistry of tungsten in metalsilicate systems: Implications for core formation in the Earth*. PhD thesis, University of Maryland.

Siebert, J., Badro, J., Antonangeli, D., and Ryerson, F. J. (2012). Metal-silicate partitioning of Ni and Co in a deep magma ocean. *Earth and Planetary Science Letters*, 321-322:189–197.

Song, H. X., Geng, H. Y., and Wu, Q. (2012). Pressure-induced group-subgroup phase transitions and post-cotunnite phases in actinide dioxides. *Physical Review B - Condensed Matter and Materials Physics*, 85:064110.

Stelzer, Z. and Jackson, A. (2013). Extracting scaling laws from numerical dynamo models. *Geophysical Journal International*, 193(3):1265–1276.

Tange, Y. and Takahashi, E. (2004). Stability of the high-pressure polymorph of zircon (ZrSiO4) in the deep mantle. *Physics of the Earth and Planetary Interiors*, 143-144:223–229.

Tarduno, J. A., Cottrell, R. D., Davis, W. J., Nimmo, F., and Bono, R. K. (2015). A Hadean to Paleoarchean geodynamo recorded by single zircon crystals. *Science*, 349(6247):521–524.

Tarduno, J. A., Cottrell, R. D., Watkeys, M. K., Hofmann, A., Doubrovine, P. V., Mamajek, E. E., Liu, D., Sibeck, D. G., Neukirch, L. P., and Usui, Y. (2010). Geodynamo, solar wind, and magnetopause 3.4 to 3.45 billion years ago. *Science*, 327:1238–1240.

Toby, B. H. and Von Dreele, R. B. (2013). GSAS-II: the genesis of a modern open-source all purpose crystallography software. *Journal of Applied Crystallography*, 46(2):544–549.

Torsvik, T. H., Burke, K., Steinberger, B., Webb, S. J., and Ashwal, L. D. (2010). Diamonds sampled by plumes from the core-mantle boundary. *Nature*, 466(7304):352–355.

Tsuno, K., Terasaki, H., Ohtani, E., Suzuki, A., Asahara, Y., Nishida, K., Sakamaki, T., Funakoshi, K. I., and Kikegawa, T. (2007). In situ observation and determination of liquid immiscibility in the Fe-O-S melt at 3 GPa using a synchrotron X-ray radiographic technique. *Geophysical Research Letters*, 34(17):L17303.

Turcotte, D. and Schubert, G. (2002). *Geodynamics*. Cambridge University Press, 2nd edition.

Vaidya, S. N., Kennedy, G. C., Physics, P., and Angeles, L. (1971). Compressibility of 27 halides to 45 kbar. *Journal of Physics and Chemistry of Solids*, 32:951–964.

van Achterbergh, E., Ryan, C. G., and Griffin, W. L. (1999). GLITTER: Online interactive data reduction for the laser ablation inductively coupled plasma mass spectrometry microprobe. In *Proceedings of the 9th V. M. Goldschmidt Conference*, pages 305–306. Lunar and Planetary Institue, Houston, TX.

van Thiel, M. (1977). Compendium of shock wave data. In *Rep. UCRL - 50108*. Lawrence Livermore National Laboratory, Livermore, CA.

Verhoogen, J. (1980). *Energentics of the Earth*. National Academy Press, Washington, D.C.

Wade, J. and Wood, B. (2005). Core formation and the oxidation state of the Earth. *Earth and Planetary Science Letters*, 236(1-2):78–95.

Wade, J. and Wood, B. J. (2012). Metal-silicate partitioning experiments in the diamond anvil cell: A comment on potential analytical errors. *Physics of the Earth and Planetary Interiors*, 192-193:54–58.

Walker, D., Cranswick, L. M. D., Verma, P. K., Clark, S. M., and Buhre, S. (2002). Thermal equations of state for B1 and B2 KCl. *American Mineralogist*, 87:805–812.

Wang, B.-T., Shi, H., Li, W.-D., and Zhang, P. (2010). First-principles study of ground-state properties and high pressure behavior of ThO2. *Journal of Nuclear Materials*, 399(2-3):181–188.

Wang, B. T., Zhang, P., Lizarraga, R., Di Marco, I., and Eriksson, O. (2013). Phonon spectrum, thermodynamic properties, and pressure-temperature phase diagram of uranium dioxide. *Physical Review B - Condensed Matter and Materials Physics*, 88(10):104107.

Watanabe, K., Ohtani, E., Kamada, S., Sakamaki, T., Miyahara, M., and Ito, Y. (2014). The abundance of potassium in the Earth's core. *Physics of the Earth and Planetary Interiors*, 237:65–72.

Wohlers, A. and Wood, B. J. (2015). A Mercury-like component of early Earth yields uranium in the core and high mantle 142Nd. *Nature*, 520(7547):337–340.

Yagi, T. (1978). Experimental determination of thermal expansivity of several alkali halides at high pressures. *Solid State Communications*, 25(8):vi.